ELECTRIDES AS SOLID-STATE IONIC CONDUCTORS FOR FLUORIDE-ION BATTERIES

Rebecca C. Radomsky

A dissertation submitted to the faculty at the University of North Carolina at Chapel Hill in partial fulfillment of the requirement for the degree of Doctor of Philosophy in the Department of Chemistry in the School of Arts and Sciences.

Chapel Hill
2024

Approved By:

Scott C. Warren

James F. Cahoon

Megan N. Jackson

Yosuke Kanai

Jillian L. Dempsey

© 2024
Rebecca C. Radomsky
ALL RIGHTS RESERVED

ABSTRACT

Rebecca C. Radomsky: Electrides as Solid-State Ionic Conductors for Fluoride-Ion Batteries
(Under the direction of Scott C. Warren)

Batteries are an essential aspect of creating a renewable energy landscape. The use of Li-ion batteries has become widespread in the past few decades, but the demand for rechargeable batteries for consumer goods, electric vehicles, and grid energy storage continues to rise. Alternate ion shuttle batteries, such as fluoride-ion batteries (FIBs) are particularly interesting due to large predicted capacities and the large window of electrochemical redox stability of the F^- anion. However, few materials that can reversibly intercalate F^- have been studied. Herein, we study electrides—materials with bare electrons located in distinct lattice sites—as potential FIB anodes.

First, we experimentally investigate the concept of electron-anion exchange (EAX) in which one F^- ion and one electride electron directly swap places within an electride framework. We then computationally predict and experimentally synthesize the first two-dimensional (2D) semiconducting electride Sc_2C. We then explore the Y-S phase space, and discover a family of new electrides based on the YS_x rocksalt phase. The most electron-rich of these phases, Y_6S_4, is a promising F^- ion conductor due to its 2D percolating network of electron density and large interlayer spaces. *Ab initio* molecular dynamics (AIMD) simulations predict that the activation energy for F^- diffusion through Y_6S_4 is less than 80 meV. We then sought to find a compatible FIB solid-state electrolyte (SSE) and thus performed a high-throughput search fluoride-containing materials. We selected and successfully synthesized $ZnSnF_6$ as an ideal candidate for a FIB electrolyte.

To those who strive to solve our world's environmental crisis,
that this work may contribute to our collective efforts.

ACKNOWLEDGEMENTS

To my mentors, colleagues, friends, and family: thank you for your continued support and encouragement. I could not have accomplished this without each of you.

I would first like to thank Professor Scott Warren, my advisor and mentor throughout my time at the University of North Carolina at Chapel Hill. I believe it uncommon for a graduate student to find an advisor whose mentorship style aligns so well with their own approach to learning. I will forever be grateful for our weekly meetings where I not only learned how to become a sophisticated problem solver, but also gained confidence as a scientist and academic. Each of my accomplishments over the past four years has only been possible through your continued support and guidance. Thank you.

To my fellow graduate students in the Warren lab: I am happy to call each of you a lab mate, colleague, and friend. Working with you has made me excited to come into lab every day. Karen, Connor, and Duncan: I could not have imagined a better cohort to start my Ph.D. with; Thank you for being my trusted allies and friends. I would especially like to thank those who have worked on electrides and fluoride-ion batteries with me; this dissertation surely would not be complete without your help and collaboration. To Jack: thank you for pushing me to develop an interest in computational chemistry. Many of the methods described in this thesis were only possible through your encouragement. To Lauren, my mentor, close colleague, and friend: you not only taught me about electrides and solid-state chemistry, but also about being a bold and successful woman in science. Thank you.

I have been lucky to find a large community of friends in North Carolina, both at UNC and throughout the research triangle. You have all made my years here some of my best.

When I look back on my time in graduate school, I am immediately reminded of lunches outside of Kenan, weekly trivia in Durham, exploring the triangle on the weekends, and golfing at Twin Lakes. Thank you to each and every person who has made these memories with me.

Finally, I would like to thank my family; I could not have accomplished this without you. Dad: thank you for sharing your love of science with me and for teaching me to always be curious about the world around me. Thank you for engaging with my science and encouraging me to broaden my horizons. Abby and Carrie: I am lucky to have built-in best friends. Thank you for all of the advice you've given me over the past 26 years about work, friendships, school, and life. And thank you for letting me annoy you throughout our entire lives. Mom: no one has believed in me as strongly and unwaveringly as you. Thank you for letting me call you daily to talk about every detail of my life. Thank you, most importantly, for always reminding me that I can do anything I set my mind to.

TABLE OF CONTENTS

LIST OF FIGURES……ix

LIST OF TABLES……xi

LIST OF ABBREVIATIONS……xii

CHAPTER 1: INTRODUCTION……1

1.1 Motivation……1

1.2 The Development of Fluoride-Ion Batteries……2

1.2.1 Ion Shuttle Batteries……2

1.2.2 History of Fluoride-Ion Batteries……4

1.2.3 Current State of Fluoride-Ion Battery Technology……6

1.2.3.1 Fluoride-Ion Battery Electrolytes……7

1.2.3.2 Fluoride-Ion Battery Electrodes……8

1.3 Electrides……9

1.3.1 Discovery of Electrides……9

1.3.2 Methods of Assessing Electride Character……10

1.3.3 Rocksalt-Derived Layered Electrides……11

1.4 Electron-Anion Exchange in Electrides……13

1.5 Overview of Research Described in this Thesis……15

1.5.1 3D MXene Synthesis via Fluorination of an Electride……15

1.5.2 Sc_2C – A 2D Semiconducting Electride……15

1.5.3 The Yttrium Sulfide Electrides……16

1.5.4 Novel Solid-State Electrolytes with an ABF_6 Structure……16

REFERENCES.....17

CHAPTER 2: METHODS.....24

2.1 Introduction.....24

2.2 Computational Methods.....24

2.2.1 Geometry Optimization and Calculations of Structure.....25

2.2.2 Electronic Structure.....27

2.2.2.1 Electron Localization Function.....27

2.2.2.2 Band Structure.....27

2.2.3 Thermodynamic Stability.....28

2.2.4 Ion Diffusion.....29

2.2.4.1 Nudged Elastic Band.....29

2.2.4.2 *Ab Initio* Molecular Dynamics.....29

2.3 Synthetic Methods.....30

2.3.1 Chemical Fluorination via XeF_2.....30

2.3.1.1 Y_2C as a Reactant.....30

2.3.1.2 XeF_2 as a Fluorinating Agent.....31

2.3.1.2.1 XeF_2 Chemical Compatibility.....32

2.3.1.3 Reactor Design.....33

2.3.1.3.1 High-Temperature SiO_2 Reactor.....33

2.3.1.3.2 Controllable Low-Temperature HDPE Reactor.....35

2.3.2 Synthesis of Yttrium Sulfide.....37

2.3.3 Synthesis of ABF_6 Compounds.....37

2.3.3.1 Aqueous Synthesis of Hydrates.....38

2.3.3.2 Mechanochemical Ball Milling.....39

2.4 Characterization Methods.....39

2.4.1 Powder X-Ray Diffraction.....40
2.4.1.1. Rietveld Refinement.....40
2.4.2 Transmission Electron Microscopy.....43
2.4.2.1 Imaging.....44
2.4.2.2 Energy Dispersive X-ray Spectroscopy.....44
2.4.2.3 Electron Diffraction.....45
2.4.3.2.1 Finding Zone Axes.....46
REFERENCES.....49
CHAPTER 3: 3D MXENE SYNTHESIS VIA FLUORINATION OF AN ELECTRIDE.....54
3.1 Introduction.....54
3.2 Full Conversion from an Electride to a 3D MXene.....56
3.3 Study of Solid-State Kinetics.....58
3.4 Room-Temperature Conversion of Y_2C to Y_2CF_2.....63
REFERENCES.....65
CHAPTER 4: SC_2C – A 2D SEMICONDUCTING ELECTRIDE.....69
4.1 Introduction.....69
4.2 Phase Diagram Exploration.....72
4.3 Structural Characterization.....73
4.4 Electronic Structure Characterization.....76
4.5 Stability in Air.....78
4.6 Conclusions.....79
REFERENCES.....81
CHAPTER 5: THE YTTRIUM SULFIDE ELECTRIDES.....85
5.1 Introduction.....85
5.2 Phase Diagram Exploration.....88

5.3 Electronic Structures……89

5.4 Structural Characterization……..91

5.5 Computational Fluorination……..98

5.6 Conclusions……..102

REFERENCES……..104

CHAPTER 6: ABF_6 MATERIALS AS FIB ELECTROLYTES……107

6.1 Introduction……..107

6.2 ABF_6 Compounds and Structures……108

6.3 Electronic Structure……109

6.4 Fluoride Diffusion……114

6.5 Solid-State Synthesis of $ZnSnF_6$……...117

6.6 Conclusions……..118

REFERENCES……..119

APPENDIX A: SUPPORTING INFORMATION FOR CHAPTER 3……121

APPENDIX B: SUPPORTING INFORMATION FOR CHAPTER 5……..122

APPENDIX C: SUPPORTING INFORMATION FOR CHAPTER 6……125

LIST OF FIGURES

Figure 1-1. Conversion and intercalation battery electrodes.....3

Figure 1-2. Theoretical energy densities of battery systems.....5

Figure 1-3. Schematic of a fluoride-ion battery.....6

Figure 1-4. Electron localization functions of Ca_2N and Y_2C.....11

Figure 1-5. Y-C binary phase diagram and examples of disordered and ordered structures...13

Figure 1-6. Electron-anion exchange.....14

Figure 2-1. Errors in lattice constant calculations.....25

Figure 2-2. Schematic of reactor for Y_2C/XeF_2 high-temperature reactions.....33

Figure 2-3. Schematic of reactor for Y_2C/XeF_2 low-temperature reactions.....35

Figure 2-4. JEMS example for finding ZA.....48

Figure 3-1. The Y_2C electride and 3D MXene Y_2CF_2.....55

Figure 3-2. XRD of Y_2C before and after exposure to XeF_2.....56

Figure 3-3. XRD of the fluorination of fresh (bottom) and oxidized (top) Y_2C.....57

Figure 3-4. Extents of Y_2C fluorinations.....60

Figure 3-5. Linearized Avrami plots at each temperature.....61

Figure 3-6. Arrhenius plot of the fluorination of Y_2C.....62

Figure 3-7. XRD pattern of Y_2CF_2 synthesized at room temperature.....63

Figure 4-1. Phase exploration of the Sc-S system.....72

Figure 4-2. X-ray diffraction patterns of experimental and calculated Sc_2C phases.....74

Figure 4-3. Filtered HRTEM images of Sc_2C particles.....75

Figure 4-4. Electron diffraction pattern of annealed Sc_2C.....76

Figure 4-5. Electronic structure of Sc_2C.....77

Figure 4-6. PXRD of Sc2C oxidation……79

Figure 5-1. Y-C and Sc-S binary phase diagrams……..87

Figure 5-2. New Y-S phases discovered by an evolutionary algorithm……..89

Figure 5-3. Electron Localization Functions of Y_6S_4, Y_6S_5, and YS……..90

Figure 5-4. Connectivity of electron density in the Y_6S_4 electride……..91

Figure 5-5. Experimental and predicted XRD patterns of the Y-S phases……..92

Figure 5-6. XRD patterns predicted by different functionals……..93

Figure 5-7. XRD studies of varying Y:S reagent stoichiometries……..94

Figure 5-8. Rietveld refinement of the ordered and disordered structures of Y_6S_4……96

Figure 5-9. Y_6S_4F structure……99

Figure 5-10. Arrhenius plot of F^- diffusion via MD……101

Figure 5-11. Predicted ground-state structure of Y_6S_4F……..102

Figure 6-1. ABF_6 structures and space groups……..108

Figure 6-2. Band gaps calculated via band structure vs. density of states……..110

Figure 6-3. Band structure (and density of states of $MgBiF_6$ calculated via HSE……111

Figure 6-4. Band gaps calculated via HSE and PBE……112

Figure 6-5. Densities of states of $MgTiF_6$, $MgMnF_6$, and $MgSnF_6$……..114

Figure 6-6. NEB pathways in ABF_6 materials……115

Figure 6-7. X-ray diffraction of $ZnSnF_6$ from mechanochemical ball-milling……117

Figure A-1. XRD of partially fluorinated Y_2C……..121

Figure B-1. Y_2SO_2 structure and XRD pattern of oxidized Y_6S_4……..122

Figure B-2. Bright-Field TEM images and EDS spectra of Y_6S_x particles……123

Figure C-1. Densities of states for Mg-containing structures……..128

LIST OF TABLES

Table 2-1. Experimental and calculated lattice parameters for rocksalt structures……26

Table 3-1. Rate constants as determined via the Avrami method……61

Table 5-1. Y_6S_4 experimental lattice parameters compared to various DFT functionals……..93

Table 5-2. Refined occupancy of each S site in Y_6S_6……..97

Table 5-3. Diffusion constants of F^- through Y_6S_4……100

Table 6-1. Structures for in-depth band structure investigation……..113

Table 6-2. Diffusion barriers and band gaps for a set of ABF6 materials……116

Table C-1. Band gaps and IDPP diffusion barriers of all ABF_6 structures……125

LIST OF ABBREVIATIONS

0D	zero-dimensional
1D	one-dimensional
2D	two-dimensional
AIMD	*ab initio* molecular dynamics
BPR	ball-to-powder ratio
CI-NEB	climbing image nudged elastic band
CVD	chemical vapor deposition
DOS	density of states
DFT	density functional theory
E_a	activation energy
EA	evolutionary algorithm
EAX	electron anion exchange
EDS	energy dispersive X-ray spectroscopy
ELF	electron localization function
FFT	fast Fourier transform
FIB	fluoride-ion battery
FWHM	full width at half maximum
GGA	generalized gradient approximation
HAADF	high-angle annular dark field
HDPE	high-density polyethylene
HF	Hartree-Fock
HRTEM	high-resolution transmission electron microscopy
K_B	Boltzmann's constant
LDPE	low-density polyethylene

LIB	lithium-ion battery
Li-S	lithium sulfur battery
MAE	mean absolute error
MSE	mean squared error
MSD	mean squared displacement
MD	molecular dynamics
NEB	nudged elastic band
OCV	open-circuit voltage
PAW	projector augmented wave
PBE	Perdew-Burke-Ernzerhof
PXRD	powder X-ray diffraction
PyMatGen	Python Package for Materials Genomics
SA	selected area aperature
SEI	solid-electrolyte interface
Simmate	Simulated Materials Ecosystem
SSE	solid-state electrolyte
S/TEM	scanning/transmission electron microscopy
TEM	transmission electron microscopy
USPEX	Universal Structure Predictor: Evolutionary Xtallography
VASP	Vienna *ab initio* Software Package
XPS	X-ray photoelectron spectroscopy
XRD	X-ray diffraction
ZA	zone axis

CHAPTER 1: INTRODUCTION

1.1 Motivation

Since the 1970s, scientists have not only studied the impacts of burning fossil fuels on the environment[1–5], but also developed methods to minimize these consequences in the future[6,7]. At the forefront of this movement is the need to overhaul and rebuild our global energy landscape. Coal- and oil-based energy production, whether for transportation, manufacturing, or electrification, is the primary contributor to the environmental crisis[1,2]. Therefore, a switch to renewable energy is of utmost importance. Government-funded research into solar and wind energy has significantly increased in the past 50 years, with both of these methods sharing a sizeable portion of the energy market since the early 2000s[8–13]. However, as these energy conversion methods have become more mainstream, the lack of suitable methods for storing that energy has become apparent[14,15].

Current solar technologies have the ability to meet global energy demands by covering only 1.2% of the Sahara Desert with solar panels (335 km^2)[16]. Why, then, does solar energy make up less than 5% of global energy production? The answer lies in our current technologies for storing and transporting this energy. One of the greatest benefits of traditional fossil fuel-based energy is the ease of transportation. Oil itself stores energy until it is ready to be used. Conversely, renewable energy relies on external storage in the form of batteries. However, technologies for energy *storage* have not advanced at the same pace as those for energy *conversion* (i.e., solar panels, wind turbines).[17,18] Thus, for renewable energy to have a global impact, more efficient batteries must be developed.

1.2 The Development of Fluoride-Ion Batteries

1.2.1 Ion Shuttle Batteries

Batteries have been used for small-scale energy storage for more than 2 centuries. Alessandro Volta developed the first working battery in 1800, which was able to supply a constant current for close to 1 hour[19,20]. However, these cells and many subsequent iterations were primary batteries, meaning that they could only be used once. Primary batteries are useful in their own right (evidenced by the continuous popularity of single-use disposable AA and AAA batteries) but are not able to meet many battery demands. For example, mobile electronics would not be practical without the ability to be frequently charged and discharged. In 1859, Gaston Planté developed the first rechargeable battery—the lead-acid battery.[21] This technology, which is still implemented in most vehicles, relies on the reversible reactions of Pb (anode) and PbO_2 (cathode) with an H_2SO_4 electrolyte.

More than a century after the invention of reversible batteries, intercalation-based electrodes were proposed and developed by M. Stanley Whittingham[22,23]. The process of intercalation consists of inserting small ions or molecules (in this case, Li^+) into crystallographic voids or interstitial sites of a host material. In this process, the host material remains relatively unchanged, with host atoms occupying the same crystallographic sites before and after intercalation. Rather than in conversion-based batteries, where the atomic and crystal structure of the host material is completely altered upon conversion (i.e., Pb to $PbSO_4$), intercalation-based electrodes allow the host material structure to remain relatively unchanged throughout the charging and discharging processes, as shown in Figure 1-1.

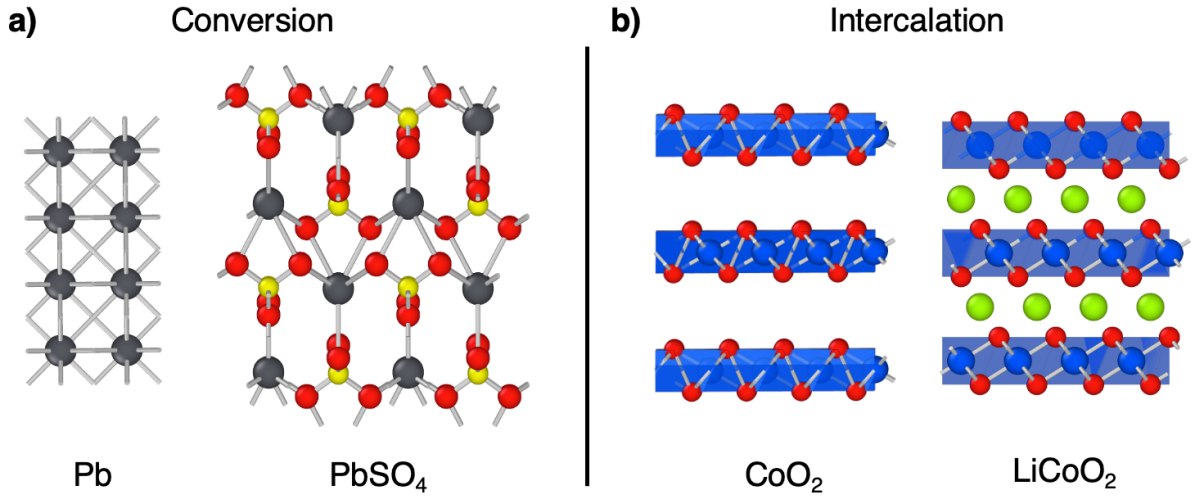


Figure 1-1. Conversion and intercalation battery electrodes. (a) As SO_4 reacts with the Pb electrode in lead-acid batteries, all the original bonds are broken, and the volume expands significantly to accommodate new species. **(b)** As Li^+ intercalates into CoO_2, the CoO_2 framework remains relatively unchanged, without breaking or reforming of bonds or significant volume expansion.

In 1980, John B. Goodenough discovered an intercalation-based (Li)CoO_2 cathode for Li-ion batteries (LIBs)[24,25]. The large capacity, low volume change upon charging/discharging, and high Li^+ ionic conductivity of CoO_2 cathodes not only enable the realization of Li-ion batteries but also have made them among the most successful cathodes to date. The first working prototype of a modern Li-ion battery was developed by Akira Yoshino in 1985[26] upon his development of a petroleum coke carbonaceous anode, which is the basis for current commercial graphite anodes. Whittingham, Goodenough, and Yoshino were awarded the Nobel Prize in Chemistry in 2019 for the development of Li-ion batteries.

Despite the commercial success of LIBs, they have not fulfilled the need to support growing renewable energy use. However, due to the increasing sales of electric vehicles, the demand for Li is starting to surpass the supply available from current mining infrastructure[27,28]. To meet the increasing demand for sustainable batteries, the market must either develop more

mining infrastructure, recycle used LIBs more efficiently, or develop alternative battery systems. Ethical and geopolitical concerns regarding the mining practices of both Li and Co have shifted much of the current research toward either recycling current batteries or developing new, Li-free technologies.

A growing sector of research is focused on alternative energy storage technologies. One of the most promising alternatives is the lithium-sulfur (Li-S) battery, which operates with a sulfur cathode and Li-metal anode[29–31]. Li-S batteries not only have increased safety compared to LIBs due to the lack of flammable electrolytes, but S is also an extremely safe, abundant, and lightweight cathodic material.[32] However, these batteries still rely on a large amount of either mined or recycled Li. Many researchers are also studying alternate ion batteries that follow the same general mechanism as LIBs. Instead of shuttling Li^+ between the anode and cathode, these batteries rely on other cationic species, with the most popular being Na^+[33,34], K^+[35,36], Mg^{2+}[37], Zn^{2+}[38,39], and Al^{3+}[40–42]. However, all of these technologies face challenges in ionic diffusion either due to increased ionic radii (Na^+, K^+) or multivalency (Mg^{2+}, Zn^{2+}, Al^{3+}) in comparison to Li^+. In addition, all ion batteries that rely on metal cations (including Li^+) face the drawback of dendritic metal growth on the anodic surface[43,44], causing the battery performance to decrease significantly with continued use. Therefore, some researchers have broadened their scope to study batteries that shuttle ions other than metal cations. In particular, fluoride-ion batteries (FIBs) have received increasing attention due to the relatively low mass and high redox stability of F^-[45–47].

1.2.2 History of Fluoride-Ion Batteries

Electrochemical cells that shuttle F^- were first proposed and realized in the 1970s[48–50]. The first experimental cells utilized a doped ß-PbF_2 electrolyte with a Pb anode and either a CuF_2 or AgF cathode[48]. However, these cells suffered from extremely poor capacities, which is thought to be due to oxidation of the Pb anode material. Research on FIBs continued

through the 1970s and early 1980s, with doped CuF_2 exhibiting much improved capacities over initial cells, and Bi/BiF_3 was also introduced as an efficient cathode material[49]. However, research into FIBs significantly decreased following this promising research, with almost no studies on fluoride-ion cells published between 1981 and 2011.

However, enthusiasm for FIBs spiked again in 2011 following Reddy and Fitchner's report[45] on the first reversible all-solid-state FIB operating at elevated temperatures of 150-200 °C. Since this "reintroduction" of FIBs, research on electrolytes and electrodes for FIBs has significantly increased in recent years. In fact, many proposed cells have higher theoretical capacities and open-circuit voltages (OCVs) than commercial LIBs and other proposed cation-shuttle systems[51].

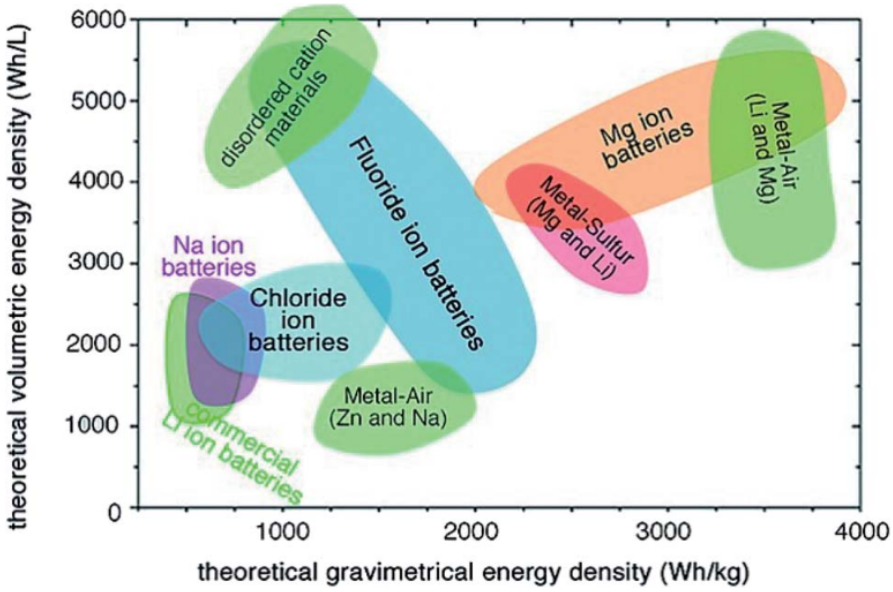


Figure 1-2. Theoretical energy densities of battery systems. The theoretical gravimetric and volumetric energy densities of multiple alternate battery systems in comparison to those of commercial LIBs. FIBs have a particularly promising theoretical volumetric energy density. Adapted from ref. 51.

Fluorine is the most electronegative element on the periodic table, and thus, F^- has an incredibly high redox stability. This allows FIBs to operate at high OCVs without destabilizing

the shuttle ion itself. The theoretical volumetric and gravimetric energy densities displayed in Figure 1-2 demonstrate the usefulness of a FIB for large-scale energy storage.

1.2.3 Current State of Fluoride-Ion Battery Technology

FIBs operate under the same principles as other cation-shuttle batteries, with the exception of the direction of ion flow as the battery is charged and discharged (due to the negative charge of F^- compared to the positive charge of Li^+). As the battery is discharged and electrons flow from the anode to the cathode through an external circuit, F^- ions must shuttle from the cathode to the anode for the system to remain charge balanced. Because F^- has the same charge as a single electron, there is a one-to-one exchange in each electrode. Figure 1-3 shows a schematic of a standard FIB.

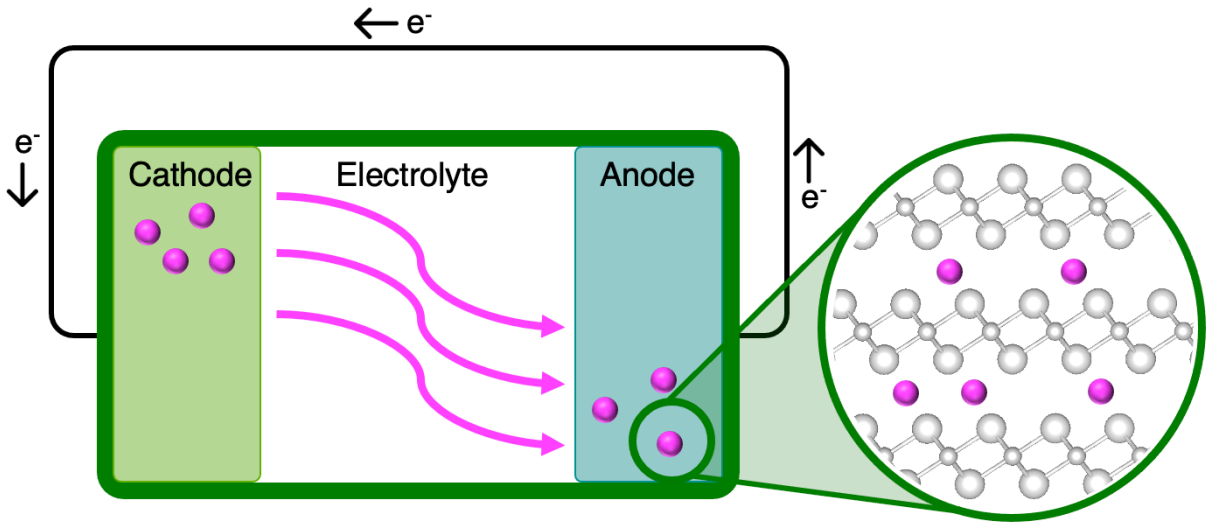


Figure 1-3. Schematic of a fluoride-ion battery. FIBs operate by shuttling F^- from the cathode to the anode through an ionically conductive electrolyte as electrons move through an external circuit from the anode to the cathode. There is a thermodynamic driving force for F^- diffusion from the cathode (higher energy) to the anode (lower energy). The identities of the best working electrodes are not yet known, but layered intercalation materials (as shown on the right) offer many advantages.

Although FIBs have impressive theoretical voltages and capacities, their realization is hindered by the lack of materials with sufficient fluoride-ion conductivities to act as electrolytes and electrodes.[52]

1.2.3.1 Fluoride-Ion Battery Electrolytes

In any ion battery, the electrolyte must have high ionic conductivity, a large window of electrochemical stability to operate at high voltages, and low electrical conductivity to prevent self-discharge. In the LIB community, the most common electrolytes are composed of a lithium salt in an organic solvent, which allows for high Li^+ conductivity via the salt, while the organic solvent acts to suppress electrical conductivity. In 2018, Davis et al. published on the first liquid electrolyte for an FIB system—a combination of tetraalkylammonium salt and fluorinated ether.[53] This electrolyte was ground-breaking for FIBs due to its high room-temperature ionic conductivity and continues to be the only electrolyte operable at room temperature.

However, much of the research in the field of FIB electrolytes is a continued search for solid-state electrolytes (SSEs)[46,54–57] due to their increased safety compared to flammable and volatile liquid electrolytes. Many solid fluoride-ion conductors that have been proposed and studied as FIB electrolytes are either tysonite-type (i.e., LaF_3) or fluorite-type (i.e., CaF_2) crystals[47]. Tysonite-type structures are often a binary fluoride with a rare earth metal, and frequently do not have sufficient ionic conductivities until they are doped with an aliovalent ion. In Reddy and Fitchner's 2011 paper[45], they introduced a Ba-doped LaF_3 electrolyte, which can exhibit F^- conductivity up to 10^{-4} S cm^{-1} as a single crystal. Although this conductivity is sufficient for a battery electrolyte, single crystals large enough for an electrochemical cell are difficult and expensive to grow. Therefore, polycrystalline SSEs are a much more feasible avenue for achieving an all-solid-state FIB. However, grain boundaries and an increased number of defects significantly decrease the ionic conductivity of polycrystalline solids compared to single crystals. To date, every solid-state FIB electrolyte requires elevated temperatures to reach the required ionic conductivity to operate in a battery.[47] Therefore, for all-solid-state FIBs to be commercially realized, electrolytes that can operate at room temperature must be discovered.

1.2.3.2 Fluoride-Ion Battery Electrodes

To date, much of the research on FIB anodes and cathodes has been based on conversion-type reactions. The vast majority of FIB research has been carried out with either a CuF_2 or PbF_2 cathode or a Mg/MgF_2 or Ca/CaF_2 anode, which all operate via conversion reactions[47,58]. However, as mentioned above, these electrodes require the continuous breaking and reforming of chemical bonds throughout the conversion process and exhibit large volume changes. In a practical electrochemical cell, a large change in the volume of the electrode material can lead to cracking and decreased contact with electrolytes and additives. Intercalation-based electrodes, which have proven to be the most efficient in LIB systems due to minimized structural changes, have therefore received increased attention from the FIB community.

Intercalation-based FIB cathodes have gained popularity, with the most promising being oxides and oxyfluorides of the Ruddlesden-Popper structure[59,60], with alternating perovskite-like layers and rocksalt layers. In the rocksalt layer, some anions are vacant, allowing for the intercalation of F^- without disturbing the remaining host material. However, these materials require relatively modest operating capacities and voltages to avoid degradation during cycling and have low gravimetric capacities due to the presence of heavy transition metals.

There has been significantly less research on intercalation-based anodes for FIBs. Studies have suggested that Ruddelsden-Popper oxyfluorides, similar to those proposed for charged (defluorinated) cathodes, could act as discharged (fluorinated) anodes[61]. However, these anodes suffer from the same drawbacks as their cathode counterparts.

The difficulty in finding high-capacity and high-voltage intercalation-based FIB electrodes stems from the fact that there are very few known materials that can reversibly intercalate fluoride ions. Sundberg et al. reported computational methods to not only test all

known fluoride-containing crystals for feasibility as FIB anodes, cathodes, and electrolytes but also to discover novel fluoride-containing materials[52]. To fully realize a room-temperature, high-capacity FIB, new materials must be discovered and introduced to the community. The majority of the research described in this dissertation is devoted to discovering and testing novel materials as FIB anodes.

1.3 Electrides

Ionic solids ordinarily consist of cations and anions arranged in a set crystallographic lattice. In inorganic electrides, a class of ionic solid, some of the anionic lattice sites are instead occupied by a bare electron, henceforth referred to as the "electride electron." The term "electride" was first used by Dye in the 1980s[62,63]; however, this was not the first observation of bare electrons and their properties.

1.3.1 Discovery of Electrides

In the early 1800s, Sir Humphry Davy noted in a laboratory notebook that "when 8 Grains of potassium were heated in ammoniacal gas—it assumed a beautiful metallic appearance & gradually became of a fine blue colour."[64] About a century later, it was noted that some metals dissolved in various solvents all produced the same characteristic blue color, which has since been attributed to the solvated electron, or a bare electron in solution surrounded by solvent molecules[65–67]. Concurrently, it was noted that when rocksalts were radiated with X-rays, they often shifted in color in a uniform, reproducible way, accompanied by a significant increase in electrical conductivity[68,69]. It was proposed, and later demonstrated, that this color was due to a vacancy defect in the crystal filled with a bare electron, which is now referred to as an F-center defect[70].

In the 1980s, Dye synthesized the first material with stoichiometric repeating sites occupied by bare electrons, $Cs^+(18\text{-crown-6})_2 \cdot e^-$[71]. In this report, he coined the term electride. In 2003, the first known thermally stable electride was synthesized by Matsuishi *et al.*[71] by

treating mayenite, $[Ca_{24}Al_{28}O_{64}]^{4+}(2O^{2-})$ with calcium metal (similar to the mechanism used to produce solvated electrons in liquids), which replaced the oxygen anions with electride electrons. Since this discovery, many other inorganic electrides with varying lattice positions and stoichiometric ratios of electride electrons have been proposed and synthesized. Many of the first electrides were zero-dimensional (0D), meaning that each electride site was insulated from each other within the host material network. However, one-dimensional (1D)[72–74] and two-dimensional (2D) electrides have since been successfully synthesized and characterized[75–78]. The interconnectedness of the electride sites in these 1D and 2D materials leads to increased electronic and ionic mobilities, opening up electrides for a variety of applications[72,79–85].

1.3.2 Methods of Assessing Electride Character

Many proposed electrides were not initially accepted as having crystallographic lattice sites filled with bare electrons. The most common alternate hypothesis is that instead of bare electrons sitting in interstitial spaces, there are hydride (H^-) ions[86]. Since H^- is exceptionally small and light and does not contain any core electrons, it is undetectable by most traditional characterization methods. However, due to the incredibly large incoherent neutron scattering cross length of hydrogen, neutron scattering has become the standard technique for ruling out the possibility of a hydride filling the crystallographic voids in a proposed electride[87,88].

However, thorough studies into the electronic structure of proposed electrides are also necessary to not only rule out hydrides but also demonstrate the presence of bare electrons in these voids. The invention and widespread use of density functional theory (DFT) has allowed for the calculation of highly detailed electronic structures. However, because electride electrons do not have a corresponding atomic nucleus, even generalized gradient approximation (GGA) functionals tend to overestimate the delocalization of electride

electrons[89,90]. Hybrid functionals that incorporate the exact exchange of the Hartree-Fock (HF) method are better at predicting the localization of electride electrons[91].

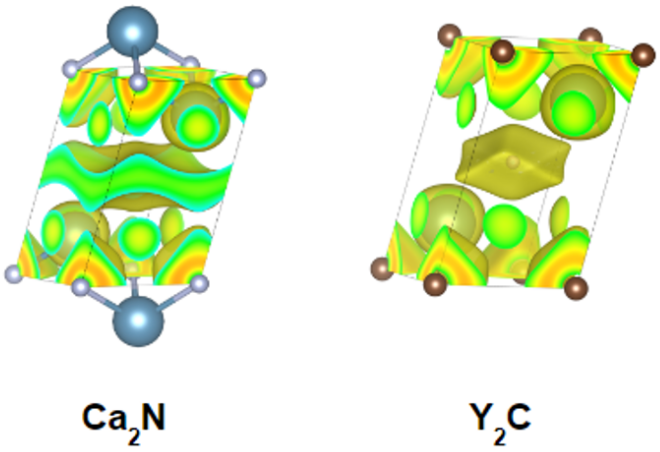


Figure 1-4. Electron Localization Functions of Ca_2N and Y_2C. The ELFs of the Ca_2N and Y_2C electrides show distinct localized electrons in lattice sites that do not contain an atom. In both structures, the electride site is centered in the unit cell.

The electride character is assessed computationally via the electron localization function (ELF), in which the likelihood of finding an electron with the same spin as a reference electron at any given point is calculated. As the electron localization increases, the ELF approaches 1. ELFs are therefore used to demonstrate that an electride has electron density localized within vacant sites in the crystal. Figure 1-4 shows the ELF for the Y_2C and Ca_2N electrides with the electride crystallographic site centered in the unit cell. Due to the nature of the surrounding host lattice, the electride sites in Ca_2N are more connected than those in Y_2C.

1.3.3 Rocksalt-Derived Layered Electrides

In the 1950s and 1960s, multiple layered nitrides, Ba_2N[92], Sr_2N[92], and Ca_2N[93], were all noted to have exceptionally large interlayer spaces, well outside the ionic radii of any of the metals surrounding the gap. Notably, the classic oxidation states of Ca (2^+) and N (3^-) did not lead to a balanced bulk material. It was proposed in 1962 that this large interlayer distance in Ca_2N is actually due to "excess electrons situated in the large gaps between layers.[94]"

However, this model was not fully accepted, and hypotheses were made that the oxidation states of the metal atoms may be +1.5 rather than +2 or that hydride ions (H^-), undetectable by most characterization techniques, may be situated in the interlayer[86]. Both of these hypotheses were disproven in the year 2000, after which these layered nitrides were accepted by the general community as electrides[88].

Since the confirmation of these nitrides as electrides, three more layered electrides have been computationally and experimentally confirmed: Gd_2C[95,96], Hf_2S[81], and Y_2C[76]. Y_2C, which was discovered as an electride by Zhang et al. in 2014[76], forms the basis for much of the research of this thesis. As the first electride discovered with a transition metal in the site directly adjacent to the electride site, Y_2C demonstrated that electride electrons can coexist next to metal atoms containing valence d-electrons. Additionally, due to the nature of each anion, Y_2C contains twice as many electride electrons per formula unit as previously reported for layered nitrides.

The structure of these layered electrides is derived from the traditional NaCl-type rocksalt structure. In the Y-C binary phase diagram, the YC_x rocksalt phase region spans from approximately 15% C to 66% C. Within this space, the overall rocksalt structure remains the same, with some partial occupancies and vacancies on either the cation or anion site. Figure 1-5 shows this Y-C phase diagram[97]. In the YC_x rocksalt phase, it has been confirmed by ELF that C vacancies are indeed filled with a bare electron, making these materials electrides[76]. Within the larger YC_x rocksalt region of the phase diagram, vacancies are typically disordered, causing either the cation or anion site to be partially occupied (other than in the case of an exact 1–1 ratio). In the case of C-deficient YC_x ($x<1$), these partially occupied C sites are also partially occupied by an electride electron. In practice, this means that sites are randomly filled with either C^{2-} or $2e^-$ according to the stoichiometry of the phase. However, in the case of the layered Y_2C electride, these sites order into specific planes such that each anion layer is either

fully occupied by C or by electride electrons. This layered structure is still a direct derivative of the traditional rocksalt structure, with only ordered vacancies, as shown in Figure 1-5.

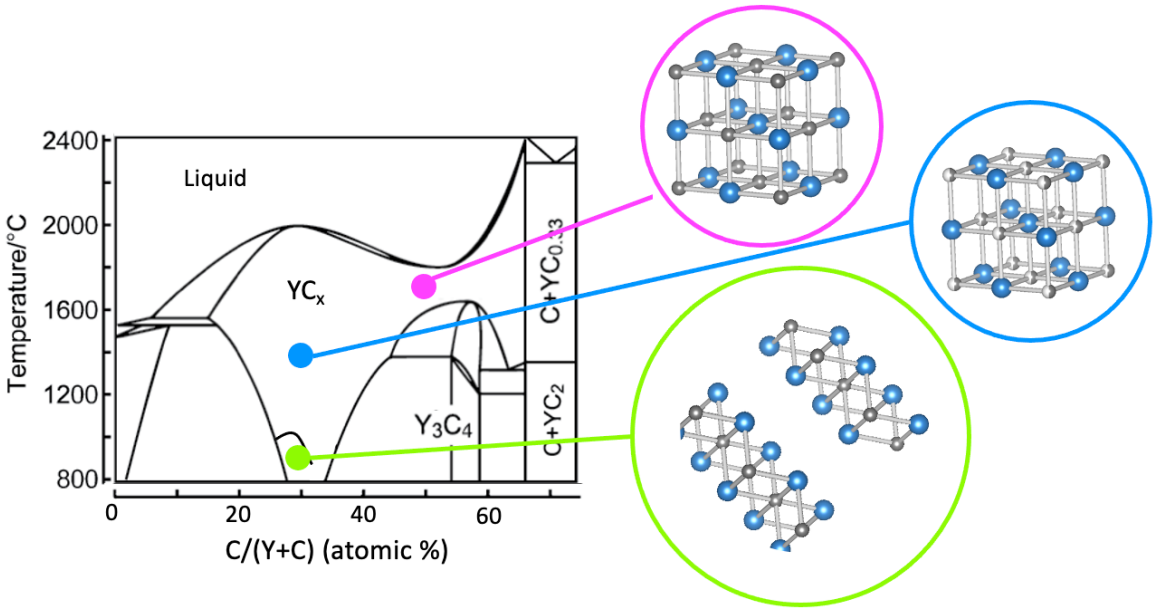


Figure 1-5. Y-C binary phase diagram and examples of disordered and ordered structures. The YC_x phase on the phase diagram represents the Y-C rocksalt phase. At an exact 1–1 stoichiometry (as shown by the pink dot), the YC structure is the same as that of NaCl. At lower anion concentrations, vacancies can either be disordered and partially occupied (blue) or ordered into specific planes (green). The structure in green is that of the Y_2C layered electride. Phase diagram adapted from ref. 97.

1.4 Electron-Anion Exchange in Electrides

Although the mechanism of cation intercalation has been studied in a variety of materials, anion intercalation has not been studied as extensively, and we have predicted that the mechanism of anion intercalation might differ from that of a traditional cation[98]. In particular, anion intercalation into materials with vacancies already filled by a bare electron–i.e. electrides—had not previously been studied, but likely differs from cation intercalation into empty vacancies. The BadELF method[99], a modification of the Bader charge analysis[100], estimates the radius of an electride electron in Y_2C to be 124 pm, very similar to the crystal

ionic radius of F^-, 119 pm. We therefore predicted that F^- ions could intercalate into the crystallographic sites occupied by electride electrons.

In 2019, Druffel et al. discovered and synthesized a fluoride analog to the electride $Y_2C(e^-)_2$, Y_2CF_2[101]. Due to the similarities in the size and charge of the F^- and e^- anions, the Y_2C electride and Y_2CF_2 are structurally similar, with F^- occupying the same layer occupied by electride electrons in Y_2C. Additionally, Y_2CF_2 has a lower energy/atom than Y_2C, which can act as a thermodynamic driving force for fluorination of a Y_2C FIB anode.

Druffel et al. computationally investigated the intercalation of F^- into Y_2C, which presented a fundamentally new mechanism of intercalation[98]. As a F^- ion intercalates into $Y_2C(e^-)_2$, it directly replaces an electride species of the same size and charge, and the host material does not undergo any reduction or oxidation. This mechanism was named "electron-anion exchange" (EAX) and is shown in Figure 1-6. EAX is the first demonstration of ion insertion without redox. We predict that the absence of redox on the nearest neighbor elements contributes to the extremely fast kinetics computationally observed during the intercalation of F^- into Y_2C. The activation energy (E_a) for F^- diffusion in Y_2C is predicted to be less than 150 meV. For comparison, the E_a for Li^+ intercalation in CoO_2 and graphite are both near 300 meV.

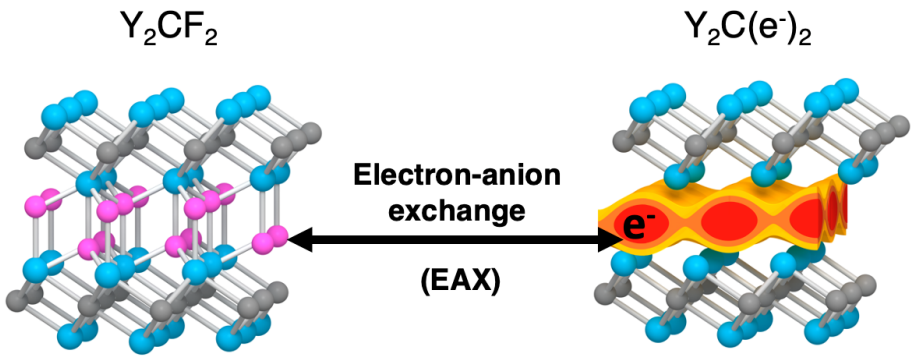


Figure 1-6. Electron-Anion Exchange. The structures of the Y_2C electride (right) and Y_2CF_2 (left) are extremely similar, allowing for the direct exchange of F^- and e^- without redox to the surrounding Y and C atoms.

However, the extreme reducing nature of electrides has made experimental realization of EAX difficult. Electrochemically, a Y_2C anode has such a high reduction potential that it will react with all known fluoride-containing electrolytes upon contact. In a practical battery, the reaction between an electrode and electrolyte contributes to decreased capacity and eventual short circuiting. Other members of the FIB community are working to develop solid-electrolyte interfaces (SEIs) to prevent this type of reaction[102]. However, until a working SEI is developed, the use of EAX cannot be fully demonstrated electrochemically.

1.5 Overview of Research Described in this Thesis

In this thesis, I will detail my efforts to further the current state of FIB research by demonstrating EAX in electrides, computationally and experimentally discovering new electrides, and developing solid-state electrolytes for FIBs that are compatible with electride anodes.

1.5.1 3D MXene Synthesis via Fluorination of an Electride

Due to the extreme reducing nature of electrides, the EAX mechanism of ion insertion into electrides has not yet been experimentally demonstrated. I have therefore developed a novel method to controllably insert F^- into Y_2C electrides at room temperature via gas-phase XeF_2. I also partially fluorinated Y_2C at various elevated temperatures and used powder X-ray diffraction (PXRD) to determine the extent of the reaction. I then use the Avrami and Arrhenius methods to calculate the experimental E_a for fluoride insertion into Y_2C for the first time. As fully fluorinated Y_2CF_2 is a 3D crystalline MXene, this method can also be generalized to the synthesis of other 3D MXenes.

1.5.2 Sc_2C – A 2D Semiconducting Electride

I have assisted with the discovery of a novel electride, Sc_2C. Because Sc is a more electronegative metal than any of those previously used in electrides, Sc_2C is the first example of a hybrid electride, where the electride sites hybridize with the d-electrons of the Sc nearest

neighbors. I performed detailed structural and morphological characterization of Sc_2C via transmission electron microscopy (TEM), high-resolution imaging and electron diffraction.

1.5.3 The Yttrium Sulfide Electrides

I have also discovered a new electride by studying the effect of substituting the C anion in Y_2C with a larger anion, S. By performing an evolutionary algorithm (EA) search on the Y-S phase diagram and applying subsequent ELFs, I have discovered a new suite of Y-S electrides with varying stoichiometries. The most anion-deficient of these, Y_6S_4, is the basis of much of this thesis. Y_6S_4 is analogous to previously known layered electrides, with the addition of S pillars in the previously vacant electride layer. I perform detailed calculations of the structure and electronic structure of Y_6S_4 and subsequently synthesize it via high-temperature solid-state synthesis. I then characterized the material via PXRD and TEM and compared it to the computationally derived structure.

In purely 2D electrides such as Y_2C, there is a shift in the stacking sequence as the electride is fluorinated. For example, Y_2C is ABC stacked, while Y_2CF_2 is AA stacked. However, we have predicted that the S pillars in Y_6S_4 act as structural supports throughout intercalation, decreasing the E_a for F^- diffusion. We performed *ab initio* molecular dynamics (AIMD) simulations on F^- within the Y_6S_4 framework and discovered an extremely low E_a for F^- diffusion.

1.5.4 Novel Solid-State Electrolytes with an ABF_6 Structure

Finding materials that are F-ion conductors is essential for fully operational FIB. Sundberg et al. previously published a study predicting the E_a for diffusion in every known F-containing crystal.[52] A specific class of materials with a stoichiometry of ABF_6 have emerged as particularly good ionic conductors. I performed detailed calculations of the electronic structure and F^- diffusion of each known ABF_6 material. After determining the best candidates for FIB anodes, I developed a synthetic method via mechanochemical ball milling.

REFERENCES

(1) Redlin, M.; Gries, T. Anthropogenic Climate Change: The Impact of the Global Carbon Budget. *Theoretical and Applied Climatology* **2021**, *146*, 713–721.

(2) Montzka, S. A.; Dlugokencky, E. J.; Butler, J. H. Non-CO2 Greenhouse Gases and Climate Change. *Nature* **2011**, *476*, 43–50.

(3) Crowley, T. J.; Berner, R. A. Paleoclimate. CO2 and Climate Change. *Science* **2001**, *292*, 870–872.

(4) Vitousek, P. M. Beyond Global Warming: Ecology and Global Change. *Ecology* **1994**, *75*, 1861–1876.

(5) Hughes, I. Biological Consequences of Global Warming: Is the Signal Already Apparent? *Trends Ecol. Evol.* **2000**, *15*, 56–61.

(6) Turner, J. A. A Realizable Renewable Energy Future. *Science* **1999**, *285*, 687–689.

(7) Dincer, I. Renewable Energy and Sustainable Development: A Crucial Review. *Renew. Sustain. Energy Rev* **2000**, *4*, 157–175.

(8) Kannan, N.; Vakeesan, D. Solar Energy for Future World: - A Review. *Renew. Sustain. Energy Rev* **2016**, *62*, 1092–1105.

(9) Mekhilef, S.; Saidur, R.; Safari, A. A Review on Solar Energy Use in Industries. *Renew. Sustain. Energy Rev* **2011**, *15*, 1777–1790.

(10) Green; M. A. Solar Cells: Operating Principles, Technology, and System Applications. *Englewood Cliffs* **1982**.

(11) Edition, E. WIND ENERGY SYSTEMS.

(12) Musgrove, P. J. Wind Energy Conversion: Recent Progress and Future Prospects. *Solar & Wind Technology* **1987**, *4*, 37–49.

(13) Joselin Herbert, G. M.; Iniyan, S.; Sreevalsan, E.; Rajapandian, S. A Review of Wind Energy Technologies. *Renew. Sustain. Energy Rev* **2007**, *11*, 1117–1145.

(14) Ould Amrouche, S.; Rekioua, D.; Rekioua, T.; Bacha, S. Overview of Energy Storage in Renewable Energy Systems. *Int. J. Hydrogen Energy* **2016**, *41*, 20914–20927.

(15) Castillo, A.; Gayme, D. F. Grid-Scale Energy Storage Applications in Renewable Energy Integration: A Survey. *Energy Conversion and Management* **2014**, *87*, 885–894.

(16) We Could Power The Entire World By Harnessing Solar Energy From 1% Of The Sahara https://www.forbes.com/sites/quora/2016/09/22/we-could-power-the-entire-world-by-harnessing-solar-energy-from-1-of-the-sahara/ (accessed Jul 5, 2024).

(17) Yoo, H. D.; Markevich, E.; Salitra, G.; Sharon, D.; Aurbach, D. On the Challenge of Developing Advanced Technologies for Electrochemical Energy Storage and Conversion. *Materials Today* **2014**, *17*, 110–121.

(18) Semadeni, M. Energy Storage as an Essential Part of Sustainable Energy Systems: A Review on Applied Energy Storage Technologies. *ETH Zurich* **2003**.

(19) Volta, A. *Historical Records Documenting the First Galvanic Battery,"The Volta Column";* 1800; pp. 45–49.

(20) Volta, A. *"Le Opere Di Alessandro Volta (Vol. II).";* 1920.

(21) Planté, M. G. New Secondary Pile of Great Power. *The London, Edinburgh, and Dublin Philosophical Magazine and Journal of Science* **1860**, *19*, 468–469.

(22) Whittingham, M. S. Electrical Energy Storage and Intercalation Chemistry. *Science* **1976**, *192*, 1126–1127.

(23) Whittingham, M. S. Chemistry of Intercalation Compounds: Metal Guests in Chalcogenide Hosts. *Progress in Solid State Chemistry* **1978**, *12*, 41–99.

(24) Mizushima, K.; Jones, P. C.; Wiseman, P. J.; Goodenough, J. B. LixCoO2 (0< X< -1): A New Cathode Material for Batteries of High Energy Density. *Mater. Res. Bull.* **1980**, *15*, 783–789.

(25) US4668595A - Secondary battery - Google Patents https://patents.google.com/patent/US4668595/en (accessed Jul 5, 2024).

(26) Yoshino, A. The Birth of the Lithium-Ion Battery. *Angew. Chem. Int. Ed* **2012**, *51*, 5798–5800.

(27) Alessia, A.; Alessandro, B.; Maria, V.-G.; Carlos, V.-A.; Francesca, B. Challenges for Sustainable Lithium Supply: A Critical Review. *J. Clean. Prod.* **2021**, *300*, 126954.

(28) Martin, G.; Rentsch, L.; Höck, M.; Bertau, M. Lithium Market Research – Global Supply, Future Demand and Price Development. *Energy Storage Materials* **2017**, *6*, 171–179.

(29) Zhang, S. S. Liquid Electrolyte Lithium/Sulfur Battery: Fundamental Chemistry, Problems, and Solutions. *J. Power Sources* **2013**, *231*, 153–162.

(30) Rauh, R. D. A Lithium/Dissolved Sulfur Battery with an Organic Electrolyte. *J. Electrochem. Soc.* **1979**, *126*, 523.

(31) Akridge, J. Li/S Fundamental Chemistry and Application to High-Performance Rechargeable Batteries. *Solid State Ionics* **2004**, *175*, 243–245.

(32) Liang, X.; Yun, J.; Wang, Y.; Xiang, H.; Sun, Y.; Feng, Y.; Yu, Y. A New High-Capacity and Safe Energy Storage System: Lithium-Ion Sulfur Batteries. *Nanoscale* **2019**, *11*, 19140–19157.

(33) Slater, M. D.; Kim, D.; Lee, E.; Johnson, C. S. Sodium-Ion Batteries. *Adv. Funct. Mater* **2013**, *23*, 947–958.

(34) Yabuuchi, N.; Kubota, K.; Dahbi, M.; Komaba, S. Research Development on Sodium-Ion Batteries. *Chem. Rev.* **2014**, *114*, 11636–11682.

(35) Rajagopalan, R.; Tang, Y.; Ji, X.; Jia, C.; Wang, H. Advancements and Challenges in Potassium Ion Batteries: A Comprehensive Review. *Adv. Funct. Mater* **2020**, *30*, 1909486.

(36) Min, X.; Xiao, J.; Fang, M.; Wang, W. (Alex); Zhao, Y.; Liu, Y.; Abdelkader, Amr. M.; Xi, K.; Kumar, R. V.; Huang, Z. Potassium-Ion Batteries: Outlook on Present and Future Technologies. *Energy Environ. Sci.* **2021**, *14*, 2186–2243.

(37) Wang, F.; Fan, X.; Gao, T.; Sun, W.; Ma, Z.; Yang, C.; Han, F.; Xu, K.; Wang, C. High-Voltage Aqueous Magnesium Ion Batteries. *ACS Cent. Sci.* **2017**, *3*, 1121–1128.

(38) Tang, B.; Shan, L.; Liang, S.; Zhou, J. Issues and Opportunities Facing Aqueous Zinc-Ion Batteries. *Energy Environ. Sci.* **2019**, *12*, 3288–3304.

(39) Ming, J.; Guo, J.; Xia, C.; Wang, W.; Alshareef, H. N. Zinc-Ion Batteries: Materials, Mechanisms, and Applications. *Materials Science and Engineering: R: Reports* **2019**, *135*, 58–84.

(40) Jayaprakash, N.; Das, S. K.; Archer, L. A. The Rechargeable Aluminum-Ion Battery. *Chem. Commun.* **2011**, *47*, 12610–12612.

(41) Zhang, Y.; Liu, S.; Ji, Y.; Ma, J.; Yu, H. Emerging Nonaqueous Aluminum-Ion Batteries: Challenges, Status, and Perspectives. *Adv. Mater.* **2018**, *30*, e1706310.

(42) Yuan, D.; Zhao, J.; Manalastas, W.; Kumar, S.; Srinivasan, M. Emerging Rechargeable Aqueous Aluminum Ion Battery: Status, Challenges, and Outlooks. *Nano Materials Science* **2020**, *2*, 248–263.

(43) Lu, W.; Xie, C.; Zhang, H.; Li, X. Inhibition of Zinc Dendrite Growth in Zinc-Based Batteries. *ChemSusChem* **2018**, *11*, 3996–4006.

(44) Crowther, O.; West, A. C. Effect of Electrolyte Composition on Lithium Dendrite Growth. *J. Electrochem. Soc.* **2008**, *155*, A806.

(45) Anji Reddy, M.; Fichtner, M. Batteries Based on Fluoride Shuttle. *J. Mater. Chem* **2011**, *21*, 17059.

(46) Mohammad, I.; Witter, R.; Fichtner, M.; Anji Reddy, M. Room-Temperature, Rechargeable Solid-State Fluoride-Ion Batteries. *ACS Appl. Energy Mater.* **2018**, *1*, 4766–4775.

(47) Nowroozi, M. A.; Mohammad, I.; Molaiyan, P.; Wissel, K.; Munnangi, A. R.; Clemens, O. Fluoride Ion Batteries – Past, Present, and Future. *J. Mater. Chem. A* **2021**.

(48) Kennedy, J. H. Thin-Film Galvanic Cell Pb□PbF[Sub 2]□PbF[Sub 2],CuF[Sub 2]□Cu. *J. Electrochem. Soc.* **1976**, *123*, 10.

(49) Danto, Y.; Poujade, G.; Pistré, J. D.; Lucat, C.; Salardenne, J. A PbIPbF2IBiF3IBi Thin Solid Film Reversible Galvanic Cell. *Thin Solid Films* **1978**, *55*, 347–354.

(50) Schoonman, J. A Solid-State Galvanic Cell with Fluoride-Conducting Electrolytes. *J. Electrochem. Soc.* **1976**, *123*, 1772.

(51) Gschwind, F.; Euchner, H.; Rodriguez-Garcia, G. Chloride Ion Battery Review: Theoretical Calculations, State of the Art, Safety, Toxicity, and an Outlook towards Future Developments. *Eur. J. Inorg. Chem.* **2017**, *2017*, 2784–2799.

(52) Sundberg, J. D.; Druffel, D. L.; McRae, L. M.; Lanetti, M. G.; Pawlik, J. T.; Warren, S. C. High-Throughput Discovery of Fluoride-Ion Conductors via a Decoupled, Dynamic, and Iterative (DDI) Framework. *npj Comput. Mater.* **2022**, *8*, 106.

(53) Davis, V. K.; Bates, C. M.; Omichi, K.; Savoie, B. M.; Momčilović, N.; Xu, Q.; Wolf, W. J.; Webb, M. A.; Billings, K. J.; Chou, N. H.; Alayoglu, S.; McKenney, R. K.; Darolles, I. M.; Nair, N. G.; Hightower, A.; Rosenberg, D.; Ahmed, M.; Brooks, C. J.; Miller, T. F.; Grubbs, R. H.; Jones, S. C. Room-Temperature Cycling of Metal Fluoride Electrodes: Liquid Electrolytes for High-Energy Fluoride Ion Cells. *Science* **2018**, *362*, 1144–1148.

(54) Hammad Fawey, M.; Chakravadhanula, V. S. K.; Reddy, M. A.; Rongeat, C.; Scherer, T.; Hahn, H.; Fichtner, M.; Kübel, C. In Situ TEM Studies of Micron-Sized All-Solid-State Fluoride Ion Batteries: Preparation, Prospects, and Challenges. *Microsc. Res. Tech.* **2016**, *79*, 615–624.

(55) Grenier, A.; Porras-Gutierrez, A. G.; Body, M.; Legein, C.; Chrétien, F.; Raymundo-Piñero, E.; Dollé, M.; Groult, H.; Dambournet, D. Solid Fluoride Electrolytes and Their Composite with Carbon: Issues and Challenges for Rechargeable Solid State Fluoride-Ion Batteries. *J. Phys. Chem. C* **2017**, *121*, 24962–24970.

(56) Liu, L.; Yang, L.; Liu, M.; Li, X.; Shao, D.; Luo, K.; Wang, X.; Luo, Z. SnF2-Based Fluoride Ion Electrolytes MSnF4 (M = Ba, Pb) for the Application of Room-Temperature Solid-State Fluoride Ion Batteries. *J Alloys Compd* **2020**, *819*, 152983.

(57) Nowroozi, M. A.; Wissel, K.; Donzelli, M.; Hosseinpourkahvaz, N.; Plana-Ruiz, S.; Kolb, U.; Schoch, R.; Bauer, M.; Malik, A. M.; Rohrer, J.; Ivlev, S.; Kraus, F.; Clemens, O. High Cycle Life All-Solid-State Fluoride Ion Battery with La2NiO4+d High Voltage Cathode. *Commun. Mater.* **2020**, *1*, 27.

(58) Rongeat, C.; Anji Reddy, M.; Diemant, T.; Behm, R. J.; Fichtner, M. Development of New Anode Composite Materials for Fluoride Ion Batteries. *J. Mater. Chem. A* **2014**, *2*, 20861–20872.

(59) Clemens, O.; Rongeat, C.; Reddy, M. A.; Giehr, A.; Fichtner, M.; Hahn, H. Electrochemical Fluorination of Perovskite Type BaFeO2.5. *Dalton Trans.* **2014**, *43*, 15771–15778.

(60) Nowroozi, M. A.; Wissel, K.; Rohrer, J.; Munnangi, A. R.; Clemens, O. Lasrmno$_4$: Reversible Electrochemical Intercalation of Fluoride Ions in the Context of Fluoride Ion Batteries. *Chem. Mater.* **2017**, *29*, 3441–3453.

(61) Wissel, K. Topochemical Fluorination and Defluorination in the Context of Fluoride-Ion Batteries and Tuning of Magnetic Properties. *UNSPECIFIED* **2020**.

(62) Dye, J. L. Preparation and Analysis of Metal/Solvent Solutions and the Formation of Alkali Metal Anions. *J. Phys. Chem.* **1980**, *84*, 1084–1090.

(63) Dye, J. L.; DaGue, M. G.; Yemen, M. R.; Landers, J. S.; Lewis, H. L. Transmission Spectra of Thin Films Which Contain Alkali Metal Anions and/or Trapped Electrons. *J. Phys. Chem.* **1980**, *84*, 1096–1103.

(64) Thomas, S. J. M.; Edwards, P. P.; Kuznetsov, V. L. Sir Humphry Davy: Boundless Chemist, Physicist, Poet and Man of Action. *ChemPhysChem* **2008**, *9*, 59–66.

(65) Gibson, G. E.; Argo, W. L. The Absorption Spectra of the Blue Solutions of Certain Alkali and Alkaline Earth Metals in Liquid Ammonia and in Methylamine. *J. Am. Chem. Soc.* **1918**, *40*, 1327–1361.

(66) Gibson, G. E.; Argo, W. L. The Absorption Spectra of the Blue Solutions of Sodium and Magnesium in Liquid Ammonia. *Phys. Rev.* **1916**, *7*, 33–48.

(67) Franklin, E. C. REACTIONS IN LIQUID Ammonia.[1]. *J. Am. Chem. Soc.* **1905**, *27*, 820–851.

(68) Boer, J. H. de; Verwey, E. J. W. Semi-Conductors with Partially and with Completely Filled$_3$ *d* -Lattice Bands. *Proc. Phys. Soc.* **1937**, *49*, 59–71.

(69) Mott, N. F.; Peierls, R. Discussion of the Paper by de Boer and Verwey. *Proc. Phys. Soc.* **1937**, *49*, 72–73.

(70) Dye, J. L. Recent Developments in the Synthesis of Alkalides and Electrides. *J. Phys. Chem.* **1984**, *88*, 3842–3846.

(71) Issa, D.; Dye, J. L. Synthesis of Cesium 18-Crown-6: The First Single-Crystal Electride? *J. Am. Chem. Soc.* **1982**, *104*, 3781–3782.

(72) Zhang, Y.; Xiao, Z.; Kamiya, T.; Hosono, H. Electron Confinement in Channel Spaces for One-Dimensional Electride. *J. Phys. Chem. Lett.* **2015**, *6*, 4966–4971.

(73) Li, J.; Zhang, X.; Fang, Z.; Cao, X.; Li, Y.; Sun, C.; Chen, Z.; Yin, F. First-Principles Calculations to Investigate Electronic, Elastic, and Optical Properties of One Dimensional Electride Y5Si3. *Results in Physics* **2021**, *28*, 104615.

(74) Sa, B.; Xiong, R.; Wen, C.; Li, Y.-L.; Lin, P.; Lin, Q.; Anpo, M.; Sun, Z. Electronic Anisotropy and Superconductivity in One-Dimensional Electride Ca_3 Si. *J. Phys. Chem. C* **2020**.

(75) Lee, K.; Kim, S. W.; Toda, Y.; Matsuishi, S.; Hosono, H. Dicalcium Nitride as a Two-Dimensional Electride with an Anionic Electron Layer. *Nature* **2013**, *494*, 336–340.

(76) Zhang, X.; Xiao, Z.; Lei, H.; Toda, Y.; Matsuishi, S.; Kamiya, T.; Ueda, S.; Hosono, H. Two-Dimensional Transition-Metal Electride Y_2 C. *Chem. Mater.* **2014**, *26*, 6638–6643.

(77) Tada, T.; Takemoto, S.; Matsuishi, S.; Hosono, H. High-Throughput Ab Initio Screening for Two-Dimensional Electride Materials. *Inorg. Chem.* **2014**, *53*, 10347–10358.

(78) McRae, L.; Radomsky, R.; Pawlik, J.; Druffel, D.; Sundberg, J.; Lanetti, M.; Donley, C.; White, K.; Warren, S. Design of Semiconducting Electrides via Electron-Metal Hybridization: The Case of Sc2C. **2021**.

(79) Hosono, H.; Kitano, M. Advances in Materials and Applications of Inorganic Electrides. *Chem. Rev.* **2021**, *121*, 3121–3185.

(80) Hirayama, M.; Matsuishi, S.; Hosono, H.; Murakami, S. Electrides as a New Platform of Topological Materials. *Phys. Rev. X* **2018**, *8*, 031067.

(81) Kang, S. H.; Bang, J.; Chung, K.; Nandadasa, C. N.; Han, G.; Lee, S.; Lee, K. H.; Lee, K.; Ma, Y.; Oh, S. H.; Kim, S.-G.; Kim, Y.-M.; Kim, S. W. Water- and Acid-Stable Self-Passivated Dihafnium Sulfide Electride and Its Persistent Electrocatalytic Reaction. *Sci. Adv.* **2020**, *6*, eaba7416.

(82) Druffel, D. L.; Kuntz, K. L.; Woomer, A. H.; Alcorn, F. M.; Hu, J.; Donley, C. L.; Warren, S. C. Experimental Demonstration of an Electride as a 2D Material. *J. Am. Chem. Soc.* **2016**, *138*, 16089–16094.

(83) Qi, S.; Li, C.; Wang, J.; Song, X.; Zhao, M.; Chen, G. Deciphering the Influence of Anionic Electrons of Surface-Functionalized Two-Dimensional Electrides in Lithium-Sulfur Batteries. *J. Phys. Chem. Lett.* **2023**, 7992–7999.

(84) Kuganathan, N.; Hosono, H.; Shluger, A. L.; Sushko, P. V. Enhanced N2 Dissociation on Ru-Loaded Inorganic Electride. *J. Am. Chem. Soc.* **2014**, *136*, 2216–2219.

(85) Menamparambath, M. M.; Park, J.-H.; Yoo, H.-S.; Patole, S. P.; Yoo, J.-B.; Kim, S. W.; Baik, S. Large Work Function Difference Driven Electron Transfer from Electrides to Single-Walled Carbon Nanotubes. *Nanoscale* **2014**, *6*, 8844–8851.

(86) J, A. SUR LES NITRURES “ANORMAUX” DES METAUX ALCALINO-TERREUX: “CA2N, SR2N ET SRN.” **1975**.

(87) Brese, N. E.; O’Keeffe, M. Synthesis, Crystal Structure, and Physical Properties of Sr2N. *J. Solid State Chem.* **1990**, *87*, 134–140.

(88) Gregory, D. H.; Bowman, A.; Baker, C. F.; Weston, D. P. Dicalcium Nitride, Ca2N—a 2D “Excess Electron” Compound; Synthetic Routes and Crystal Chemistry. *J. Mater. Chem* **2000**, *10*, 1635–1641.

(89) Haas, P.; Tran, F.; Blaha, P.; Schwarz, K.; Laskowski, R. Insight into the Performance of GGA Functionals for Solid-State Calculations. *Phys. Rev. B* **2009**, *80*.

(90) Kulik, H. J. Perspective: Treating Electron over-Delocalization with the DFT+U Method. *J. Chem. Phys.* **2015**, *142*, 240901.

(91) Walsh, A.; Scanlon, D. O. Electron Excess in Alkaline Earth Sub-Nitrides: 2D Electron Gas or 3D Electride? *J. Mater. Chem. C* **2013**, *1*, 3525.

(92) Ariya, S. M.; Prokofyeva, E. A.; Matveeva, I. I. Investigation of Metallic Nitrides II. The Subnitrides of Strontium and Barium. *J. Gen. Chem.* **1955**.

(93) Ahmad. Ph.D. Thesis. Doctoral dissertation, 1963.

(94) By, K.; SKAPSRI. Ca,N: A Nitride with a Layer Structure.

(95) Mudryk, Y.; Paudyal, D.; Pecharsky, V. K.; Gschneidner, K. A. Magnetic Properties of Gd_2 C: Experiment and First Principles Calculations. *J. Appl. Phys.* **2011**, *109*, 07A924.

(96) Lee, S. Y.; Hwang, J.-Y.; Park, J.; Nandadasa, C. N.; Kim, Y.; Bang, J.; Lee, K.; Lee, K. H.; Zhang, Y.; Ma, Y.; Hosono, H.; Lee, Y. H.; Kim, S.-G.; Kim, S. W. Ferromagnetic Quasi-Atomic Electrons in Two-Dimensional Electride. *Nat. Commun.* **2020**, *11*, 1526.

(97) Otani, S.; Hirata, K.; Adachi, Y.; Ohashi, N. Floating Zone Growth and Magnetic Properties of Y2C Two-Dimensional Electride. *J. Cryst. Growth* **2016**, *454*, 15–18.

(98) Druffel, D. L.; Pawlik, J. T.; Sundberg, J. D.; McRae, L. M.; Lanetti, M. G.; Warren, S. C. First-Principles Prediction of Electrochemical Electron-Anion Exchange: Ion Insertion without Redox. *J. Phys. Chem. Lett.* **2020**, *11*, 9210–9214.

(99) Weaver, S. M.; Sundberg, J. D.; Slamowitz, C. C.; Radomsky, R. C.; Lanetti, M. G.; McRae, L. M.; Warren, S. C. Counting Electrons in Electrides. *J. Am. Chem. Soc.* **2023**, *145*, 26472–26476.

(100) Bader, R. F. W. Atoms in Molecules. *Acc. Chem. Res.* **1985**, *18*, 9–15.

(101) Druffel, D. L.; Lanetti, M. G.; Sundberg, J. D.; Pawlik, J. T.; Stark, M. S.; Donley, C. L.; McRae, L. M.; Scott, K. M.; Warren, S. C. Synthesis and Electronic Structure of a 3D Crystalline Stack of MXene-Like Sheets. *Chem. Mater.* **2019**, *31*, 9788–9796.

(102) Xiao, A. W.; Galatolo, G.; Pasta, M. The Case for Fluoride-Ion Batteries. *Joule* **2021**.

CHAPTER 2: METHODS

2.1 Introduction

Materials chemistry research can be broadly divided into three categories: computational modeling, experimental synthesis, and characterization of structure and properties. Each of these aspects is essential for not only building a sophisticated model of a material's chemistry but also discovering new materials. My doctoral work at the University of North Carolina at Chapel Hill has been devoted to developing an in-depth understanding of all three of these aspects. Each of these methods will be discussed herein.

2.2 Computational Methods

My computational work has been devoted to applying existing models and methods to unique crystal systems. I have employed *ab initio* DFT to perform high-throughput studies of the properties of known materials, predict new thermodynamically stable phases, calculate the structure and electronic structure of novel materials, and model the kinetics of solid-state ion diffusion.

Unless otherwise stated, each DFT calculation in this thesis was performed via the Vienna *ab initio* Software Package (VASP)[1]. Projector augmented wave (PAW) pseudopotentials[2,3] were used in all calculations—Y and Sc pseudopotentials were chosen such that each would have a valency of 11 (rather than 3); all other elemental pseudopotentials were chosen via the default VASP settings. Pseudopotential files (POTCARs) were generated using the VASPKIT standard edition[4]. The use of specific functionals will be described in each of the following sections. When necessary, the Python Package for Materials Genomics (PyMatGen)[5] was used for the setup and analysis of the

calculations. The Simulated Materials Ecosystem (Simmate)[6] software, developed by the Warren lab, was used for high-throughput calculations and when otherwise noted. For a detailed description of the methods and settings used for Simmate calculations, I point you to the dissertation of my colleague, Dr. Jack Sundberg[7].

2.2.1 Geometry Optimization and Calculations of Structure

All initial geometry optimizations and single-point energy calculations were performed using the generalized gradient approximation (GGA) functional Perdew-Burke-Ernzerhof (PBE)[8]. However, the PBE functional consistently underestimates the electron-electron correlation, thus overestimating bond lengths in solid systems[9]. The PBEsol functional[9] was thus developed specifically to accurately calculate the lattice constants in solid crystalline systems. Therefore, I often used PBEsol is used for calculations of structure that will be compared directly to experimental measurements of lattice parameters, namely, from X-ray and electron diffraction.

However, I emphasize that structural calculations, even those using the PBEsol functional, still have a nontrivial margin of error, especially for systems with unusual electronic structures[10]. Figure 2-1, adapted from Ref. 10, shows the error of various functionals in calculating lattice constants of well-known semiconductors.

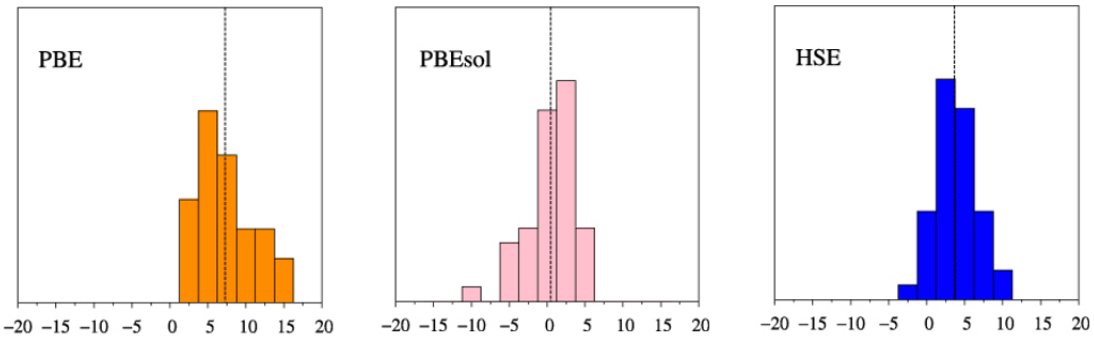


Figure 2-1. Errors in lattice constant calculations. These histograms represent the error (in pm) of lattice constants of 43 well-known semiconductors compared to experimental lattice constants. A vertical dashed line denotes the average error of each functional.

Although PBE and HSE06 consistently overestimate lattice constants, the range of errors in PBEsol is not noticeably less than that of PBEsol or HSE06[11]. Additionally, there is evidence that these errors may be dependent on structure type, with this study[10] reporting on diamond, wurtzite, zincblende, and rocksalt structures. Since all of the layered electrides described in this thesis are rocksalt-derived, I draw specific attention to the reported errors of rocksalt structures, as shown in Table 2-1.

Table 2-1. Experimental and calculated lattice parameters for rocksalt structures studied in ref. 10. All parameters are given in Å.

	Exp. Lattice	PBE	PBEsol	HSE
MgO	4.216	4.268	4.231	4.222
MgSe	5.460	5.530	5.476	5.508
CaS	5.689	5.716	5.640	5.704
CaSe	5.916	5.964	5.879	5.954
CaTe	6.348	6.388	6.294	6.390
SrS	5.990	6.063	5.985	6.043
SrSe	6.234	6.305	6.218	6.289
SrTe	6.640	6.719	6.615	6.707
BaS	6.389	6.435	6.350	6.414
BaSe	6.595	6.669	6.577	6.653
BaTe	7.007	7.027	6.919	7.018
MAE	--	0.054	0.033	0.038

Although Figure 2-1 demonstrates that the PBEsol functional is the most accurate of the three shown, once those values are parsed by structure type, it is evident that PBEsol often underestimates the lattice constants of rocksalt structures, and for many materials, HSE may be a better predictor of structure, with a similar mean absolute error (MAE) as that of PBEsol.

It is my intention that this discussion of the error associated with predicted lattice constants, regardless of functional, may serve as a reminder that first-principle predictions must be evaluated in the context of experimental observations. For the work of this thesis, both the PBEsol and HSE06 functionals are often used and will be noted when necessary.

2.2.2 Electronic Structure

Unlike calculations of structure, it is well established that a hybrid functional is necessary to calculate accurate electronic structures due to the overestimation of electron delocalization in GGA functionals. Therefore, all calculations of electronic structure were performed with the HSE06[11] functional mixed with PBE with a range-separation parameter (HFSCREEN) of 0.2, which is typical for HSE06.

2.2.2.1 Electron Localization Function

The electron localization function (ELF)[12] is a common method for computationally verifying the existence of an electride electron. Calculating an ELF with VASP[1] is relatively straightforward after completing a geometry optimization and single-point energy calculation with your functional of choice. The ELF calculation is performed by simply adding the LELF = TRUE tag to the input file (INCAR) and switching from GGA to the HSE06 hybrid functional.

Useful information from the ELF typically comes from its visualization in order to see where the electrons are localized in relation to atomic nuclei. The most straightforward ELF visualization is via an isosurface. The isosurface level can be set between 0 and 1, corresponding to an ELF value between 0 and 1, and will show all electrons localized above the set isosurface—i.e. an isosurface value of 0 will show all electron density regardless of localization and a value of 1 will show only perfectly localized electrons (which is not possible in practice). Unless otherwise noted, the program OVITO[13] was used for ELF visualization at an isosurface level of 0.5.

2.2.2.2 Band Structure

The band structure calculations performed for this thesis are primarily relevant to Chapter 6, in which I perform high-throughput calculations to find FIB electrolyte candidate materials. Although band gaps for each structure are available via the Materials Project[14] database, these were calculated via PBE and thus are severely underestimated. Therefore,

HSE06 calculations of the electronic structure of each material were performed via the "electronic-structure.vasp.matproj-hse-full" workflow in Simmate[6]. Band gaps were extracted from the "electronic-structure.vasp.matproj-band-structure-hse" workflow, and the density of states (DOS) was calculated via "electronic-structure.vasp.matproj-density-of-states-hse". When the partial density of states was evaluated by atom and/or by orbital, the VASPKIT density-of-states electronic utility was used.

2.2.3 Thermodynamic Stability

For a multielement system, thermodynamic stability is evaluated via a hull diagram, in which stable structures are located on the convex hull—i.e. they are more stable than any linear combination of structures of other stoichiometries. The energies for a hull diagram are calculated via a static energy calculation on an already relaxed structure. Energies are compared per atom, as the overall energy of a structure compounds with the number of atoms present. In order to uniformly compare the energy of each structure, the lowest-energy structure of each pure element (i.e. pure Y and pure S in the Y-S hull diagram) is artificially set to zero.

When a single structure's thermodynamic stability is being evaluated, it can be compared to the existing hull diagram of structures available on the Materials Project[14]. However, when a phase space has only been studied to a limited degree, as is the case with Y-S, there are likely many thermodynamically stable phases that have not yet been discovered. Evolutionary algorithms (EAs)[15] can thus be used to predict stable and metastable phases. For a more detailed explanation of the methods used in EAs, I refer you to the thesis of my colleague Dr. Jack Sundberg[7].

For the Y-S system, the Universal Structure Predictor: Evolutionary Xtallography (USPEX)[16] EA was used with unit cells of up to 30 atoms. The hull diagram was explored in

the range of 0.25 and 0.5 S stoichiometries to discover new anion-deficient phases, which we predicted were likely to be electrides.

2.2.4 Ion Diffusion

To evaluate a material's feasibility as an ionic conductor (and thus as a battery electrode or electrolyte), the E_a of ionic diffusion must be calculated. In this thesis, I use two methods for studying the solid-state diffusion of F^- in my structures, each with their own advantages.

2.2.4.1 Nudged Elastic Band

The nudged elastic band (NEB) method[17] calculates the E_a for a single diffusion event from point A to point B in a given structure. As the ion diffuses from point A to point B, it crosses through a transition state, which is modeled in NEB via a statistical approach. However, as many paths can be taken between points A and B, the NEB method finds the lowest-energy saddle point on the potential energy basin and calculates the energy as the ion moves across that path. NEB can be calculated with any set number of "images" or positions along the lowest-energy migration pathway. The number of images varies between studies in this thesis and thus will be noted for each calculation. The climbing image variation of NEB (CI-NEB)[18] is used for all of the calculations in Chapter 6, which drives the highest-energy image directly up to the saddle point, therefore capturing the full E_a for the pathway.

2.2.4.2 *Ab Initio* Molecular Dynamics

The other common method for determining the activation energy of diffusion is via AIMD simulations[19,20]. Although AIMD is much more computationally expensive than an NEB calculation, it allows diffusion to be studied without any assumptions of thermodynamic stability (i.e., the initial and final sites for diffusion)[21]. AIMD simulations can run for "long" timescales (up to 10s of ns) and can therefore observe multiple hopping events within one simulation. AIMD simulations also occur at elevated temperatures (rather than NEB at 0 K)

and can thus more accurately model experimental transition states. Simulations were performed for 24 temperatures ranging from 300 K to 1100 K. The diffusion constant was calculated for each temperature via the PyMatGen[5] toolkit, and the E_a of diffusion is calculated via the Arrhenius method.

2.3 Synthetic Methods

Throughout my doctoral work, I have developed a method to efficiently fluorinate electrides to transform them to 3D MXenes, synthesize novel electrides via high-temperature solid-state methods, and synthesize ternary fluorides via mechanochemical ball milling. All experiments were performed under inert atmosphere (Ar) unless otherwise stated.

2.3.1 Chemical Fluorination via XeF_2

I have developed a novel method for fluorinating Y_2C to form Y_2CF_2. Previously, Y_2CF_2 had only been synthesized directly from Y metal, graphite, and YF_3 via high-temperature solid-state synthesis at 1240 °C[22–24]. This method, using gaseous XeF_2 as the fluorinating agent, is the first method for (1) controllably reacting electrides and (2) synthesizing a 3D MXene at low temperatures.

2.3.1.1 Y_2C as a Reactant

Due to the accessibility of bare electrons, Y_2C is an extremely strong reducing agent. When in contact with air, Y_2C quickly oxidizes to form Y_2O_3 and C. Therefore, preventing the oxidation of Y_2C, both during and prior to reaction, is essential. In initial studies, Y_2C was synthesized[25] in large batches (>1 g) and immediately ground to powder. For more details on the initial synthesis of Y_2C, I point you to ref. 25. Powdered Y_2C was kept in a sealed scintillation vial in an Ar-filled glovebox (<1 ppm O_2) and used for up to 3 weeks after synthesis. However, these initial experiments had variable results, with exactly the same experimental parameters often producing conflicting results.

After controlled tests using Y_2C (1) immediately after synthesis and (2) after sitting in the glovebox for 2 weeks, I determined that these variable results are due to the slow yet continuous oxidation of Y_2C simply from being in the glovebox. Therefore, all reported experiments were performed with freshly synthesized Y_2C, not more than 48 hours after arc melting. All Y_2C was stored in the glovebox in ingot form to minimize the surface area in contact with the glovebox atmosphere. Immediately before use, the Y_2C ingot was cleaved so that a small piece (50-100 mg) could be ground for synthesis. This piece was hand-ground for ~5 minutes in an agate mortar and pestle within the glovebox and immediately transferred to the reactor. We have observed that these controls minimize the amount of oxidation of Y_2C and thus allow for extents of reaction to be consistent between experiments.

2.3.1.2 XeF_2 as a Fluorinating Agent

XeF_2 has a relatively low sublimation point, 128 °C[26], which I have exploited for the controllable fluorination of Y_2C. XeF_2 has previously been used as a fluorinating agent in select organic and inorganic syntheses[27–35], often dissolved in HF. Gaseous XeF_2 has been used as an etchant for Si[36], similar to pure F_2 gas.

As mentioned above, Y_2C is a very strong reducing agent. Similarly, due to the thermodynamic stability of Xe as a noble gas, XeF_2 is a very strong oxidizing agent. Therefore, the reaction between XeF_2 and Y_2C, shown below, is extremely thermodynamically favorable.

$$Y_2C(e^-)_2 + XeF_2 \rightarrow Y_2CF_2 + Xe + 2e^- \quad (2.1)$$

Because of the thermodynamic driving force for this reaction, I have observed that when solid Y_2C and solid XeF_2 come into contact, they immediately ignite, even in an inert (Ar) atmosphere. This ignition releases enough energy to cause the formation of YF_3, which is not accessible in a controlled low-temperature system. The irreversible formation of YF_3 significantly decreases the amount of active material and therefore must be avoided. I have

designed and implemented a set of reactors to chemically fluorinate Y_2C with XeF_2 in the gas phase while inhibiting any solid-solid contact.

2.3.1.2.1 XeF_2 Chemical Compatibility

In gas-phase reactions, the choice of reactor vessel is particularly important for inhibiting side reactions of the gaseous reagent with the container. The reactivity of XeF_2 makes this difficult, as it will react with most "inert" materials even at room temperature. The reactions of XeF_2 with Ta, SiO_2, Al_2O_3, steel (Fe and Cr), polyethylene, etc., are all thermodynamically favorable[14]. However, many of these reactions are not kinetically favorable at relatively low temperatures (<150 °C). We first tested Ta foil because it is malleable and can form a "pocket" for XeF_2 to sit in during reaction. However, immediately upon dropping a single XeF_2 crystal on Ta foil, a large flame was produced as TaF_5 was formed. Because of this exothermic reaction, Ta cannot come into contact with XeF_2 whatsoever. Although the reactions of XeF_2 with the other vessel materials listed above are also thermodynamically favorable, none have ignited when in contact with solid XeF_2 as Ta did. Previous studies on Si etching have even noted that XeF_2 does not etch SiO_2, instead only selectively etching Si[36]. Preliminary tests of XeF_2 with stainless steel, SiO_2, Al_2O_3, and high-density polyethylene (HDPE) did not produce a noticeable reaction, and thus were safe for use as a reaction vessel.

However, when reactions between Y_2C and XeF_2 are carried out at stoichiometric ratios, Y_2C is not fully converted to Y_2C even when given ample time and temperature, and no XeF_2 crystals remain. At most, we observed 70% conversion. We attribute this to interactions between XeF_2 and the container, whether chemical reactions or physical adsorption. As a result, all reactions described in this thesis are carried out at a 2.5x stoichiometric excess of XeF_2, which allows for the complete conversion of Y_2C to Y_2CF_2. We also note that some materials, such as stainless steel, will likely form a self-limiting passivating fluoride layer on the surface, preventing any further reaction with XeF_2.

2.3.1.3 Reactor Design

2.3.1.3.1 High-Temperature SiO_2 Reactor

As a proof-of-concept, initial XeF_2 and Y_2C experiments were performed at relatively high temperatures for long time frames to ensure a complete reaction. This initial reactor design allows for high temperatures, large volumes, and precise control over temperatures via a tube furnace and thermocouple. The reactor design, shown in Figure 2-2, consists of a quartz half-tube shell. The open end of the tube can be sealed shut with a full port ball valve tightened via a rubber O ring. We have not noticed any demonstrable difference in extent of reaction based on the length of the quartz tube. However, tubes of approximately 30 cm were used to allow the end of the tube to be at approximately the same position in the tube furnace throughout the reaction. The stainless steel ball valve does not fit into a standard Thermo Scientific Mini-Mite tube furnace and is inserted to sit flush with the side of the furnace to ensure that there is a reproducible small temperature gradient within the tube. The stainless steel ball valve is held at the exact height of the tube furnace by a lab jack to ensure that no strain is applied to the quartz tube.

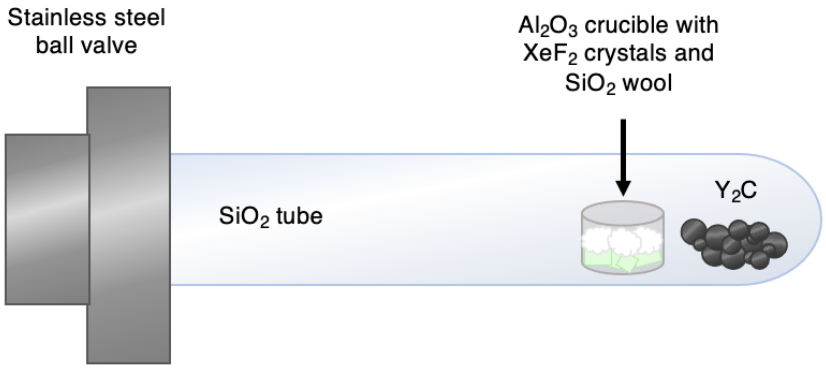


Figure 2-2. Schematic of the reactor for Y_2C/XeF_2 high-temperature reactions. Powdered Y_2C is placed in the bottom of an SiO_2 tube, followed by an Al_2O_3 crucible filled with XeF_2 crystals and packed with SiO_2 wool to prevent crystals from falling out. The tube is then closed with a stainless steel ball valve. This reactor is placed in a tube furnace for heating.

Approximately 100 mg of Y_2C was ground, and the resulting powder was immediately placed in the bottom of the quartz tube. XeF_2 was weighed and added to a small, open-top alumina crucible. A mixture of SiO_2 and Al_2O_3 wool is packed into the crucible on top of the XeF_2 crystals to ensure that they do not fall out and come into contact with the solid Y_2C. The porous nature of the wool allows for gaseous XeF_2 to easily diffuse out to react controllably with the Y_2C. Because SiO_2 and Al_2O_3 are not malleable, new wool should be used for each experiment due to its degradation and crumbling with extended use.

After the XeF_2-filled crucible was inserted into the quartz tube, it was immediately closed with a stainless steel ball valve, removed from the glovebox, and inserted into the tube furnace for reaction. If the tube is left open for an extended period of time, XeF_2 will slowly sublime at room temperature. If the tube is sealed shut but the timed reaction has not yet begun (i.e. sitting in the glovebox before being brought out to the tube furnace), then the Y_2C and XeF_2 will slowly react at room temperature, resulting in a falsely high extent of reaction.

After the reaction occurs in the tube furnace, the reaction vessel should be removed from the furnace and immediately brought into the glovebox antechamber to be pumped back into the glovebox. However, it is important to note that the reaction vessel cannot be opened until inside the glovebox. A relatively “quick” evacuation of the antechamber would be 3 vacuum cycles of 5 minutes each, causing the reaction vessel to be closed in the antechamber for at least 15 minutes until it is able to be brought into the glovebox and opened. We observed that during this 15 minutes, the reaction between XeF_2 and Y_2C continues until the vessel is opened and the components are removed. Therefore, for studies where knowing the exact extent of reaction is essential, this method is not suitable.

Throughout the reaction, excess XeF_2 will deposit on the “cold” end of the tube on the side of the stainless steel ball valve during reaction. When the reactor is opened in the glovebox, there will likely be recrystallized XeF_2 at the mouth of the tube. This XeF_2 makes it

impossible to remove the Y_2C powder without the two coming into contact and therefore must sublime away before the Y_2C can be removed. While waiting for this XeF_2 to sublime, the glovebox circulation should be turned off to ensure that F_2 gas does not react with the catalyst, which is a known irreversible reaction[37]. After the XeF_2 is sublimed, the glovebox should be purged for at least 15 minutes with fresh Ar gas.

2.3.1.3.2 Controllable Low-Temperature HDPE Reactor

For reactions between Y_2C and XeF_2, where the goal is to study the extent and rate of the reaction, it is essential to precisely start and stop the reaction. Thus, I have developed an alternate reaction setup using an HDPE tube that takes place solely inside of a glovebox to minimize the extra reaction time after the sample has been removed from heat (Figure 2-3). However, due to the melting point of high-density polyethylene (HDPE)[38], this reactor can only be used for experiments at <120 °C.

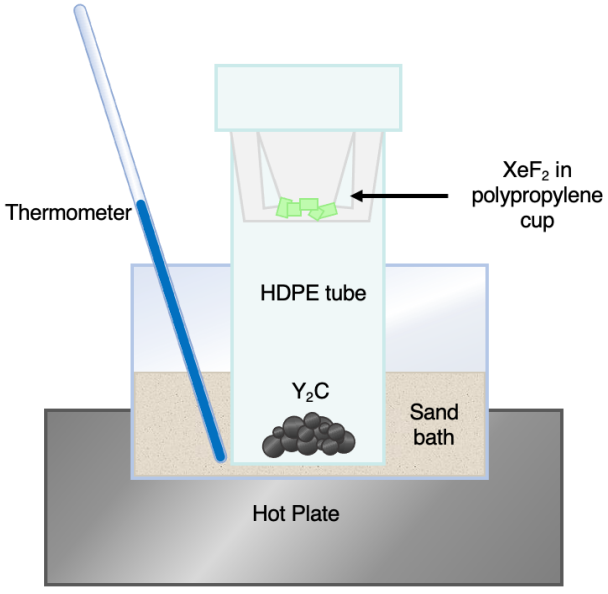


Figure 2-3. Schematic of reactor for Y_2C/XeF_2 low-temperature reactions. Powdered Y_2C is placed in the bottom of an HDPE tube, followed by a polypropylene cup containing XeF_2 crystals. The tube is closed with an HDPE lid and placed in a sand bath on a hot plate for the desired reaction temperatures and times.

A sand bath is heated to the desired temperature on a hot plate until the sand reaches a homogenous temperature, usually ~1 hour. The temperature is monitored using an external alcohol thermometer. The diameter of the sand bath should be approximately ½ the diameter of the hot plate surface to ensure even heating. A fresh piece of Y_2C, ~50 mg, is cleaved from the surface of a recently synthesized ingot. This piece is ground for 5 minutes in an agate mortar and pestle and immediately transferred to the bottom of an HDPE tube (3.175 cm inner diameter, 0.32 cm wall thickness, 60 mL volume). These tubes have straight walls (i.e., no narrowing at the mouth).

A 2.5x excess stoichiometric amount of XeF_2 is weighed and placed into a polypropylene "cup" with a bottom diameter of 2.75 cm and a top diameter of ~3.4 cm. This cup is produced by cutting ~1 cm off the top of a 15 mL disposable polypropylene beaker. Vertical cuts are then made into the cup to (1) allow for a proper fit in the HDPE tube and (2) avoid a seal against the HDPE tube to allow for gas flow. The top and bottom diameters of the cup allow it to fit snugly into the top of the HDPE tube. This cup is placed into the top of the tube, as high as possible, and the tube is closed and sealed with an HDPE lid (Figure 2-3). The reactor is then immediately placed in the sand bath to begin the reaction. For this reaction, Y_2C is at the bottom of the tube, submerged in the sand. XeF_2 is at the top of the tube, in a relatively "cool zone" due to the temperature gradient of the tube above the level of the sand bath. This is done purposefully to maintain the same partial pressure of XeF_2 for each reaction, as some of the XeF_2 remains or recrystallizes as a solid at the top of the tube.

When the desired reaction time has passed, the tube is immediately removed from the sand bath, the XeF_2 cup is removed, and the Y_2C/Y_2CF_2 powder is transferred to an XRD slide for analysis. This ensures that any reaction between Y_2C and remaining XeF_2 gas is ceased immediately upon removal from the sand bath. Any XeF_2 crystals remaining in the polypropylene cup can be recovered and used for future syntheses.

2.3.2 Synthesis of Yttrium Sulfide

My method for synthesizing yttrium sulfide electrides is based on methods used to synthesize transmission metal carbides (Y_2C, Sc_2C)[25,39]. All experiments were performed under an Ar atmosphere. Pure yttrium metal is first arc-melted twice to form a uniform button and ablate any surface oxides. This button is weighed, and a stoichiometric amount of Y_2S_3 powder is pressed into a 6 mm pellet using a Carver manual pellet press and die. Depending on the experiment, the stoichiometry of Y to Y_2S_3 will be determined to yield $Y_6S_{3.5}$, Y_6S_4, Y_6S_5, or YS. The Y button and Y_2S_3 pellet are transferred to the Cu hearth of the arc melter chamber, and the chamber is evacuated and cycled with Ar for 15 minutes. Because Y_2S_3 is not electrically conductive, the first arc melting step will be primarily to incorporate the pellet into the Y button. It is essential to only directly hit the Y metal with the plasma arc to prevent the ablation of Y_2S_3. The button is flipped over in the arc melter chamber, and melting is repeated for a total of 8 times, with each arc melting occurring for approximately 10 seconds to ensure that the material melts but the system does not overheat.

The pellet is then returned to a glovebox, loosely wrapped in Ta foil (Sigma-Aldrich, 0.025 mm thick, ≥99.9%), and placed in a quartz ampule (8 mm inner diameter, 12 mm outer diameter). This ampule is sealed under 1 mBar Ar using a hydrogen-oxygen torch. The ampule is then placed in a Mini-Mite tube furnace and heated to 1100 °C for 7 days with a linear 48-hour cool-down. Small changes in annealing time and temperature do not affect the result. When ready for analysis, the yttrium sulfide pellet is cleaved using a chisel and ground to a powder in an agate mortar and pestle.

2.3.3 Synthesis of ABF_6 compounds

Methods for synthesizing ABF_6 compounds and their hydrates were developed from previous reports of ABF_6 hydrates or other syntheses of ternary metal fluorides.

2.3.3.1 Aqueous Synthesis of Hydrates

$ZnTiF_6 \cdot 6H_2O$ and $MgTiF_6 \cdot 6H_2O$ were synthesized similarly to previous reports.[40] Because these materials are already hydrated, they do not need to be prepared in an Ar atmosphere and are thus prepared in a fume hood. Zinc carbonate basic, $ZnCO_3$ (Sigma-Aldrich, >58% Zn basis), is dissolved in fluorotitanic acid, H_2TiF_6 (dihydrogen hexafluorotitanate, 60% w/w aq. Soln.) and stirred on a stir plate for 60 minutes. The desired chemical reaction is as follows:

$$ZnCO_3 + H_2TiF_6 \rightarrow ZnTiF_6 + H_2O + CO_2 \quad (2.2)$$

This reaction produces CO_2 gas, and thus, the cessation of bubbling is an indicator of a complete reaction. The solution is then dropped into a wide glass Petri dish and H_2O is allowed to evaporate at room temperature until only crystals of $ZnTiF_6 \cdot 6H_2O$ remained. Depending on the volume of liquid and diameter of the Petri dish, this evaporation process will take between 1 and 5 days. This slow evaporation and crystallization produces large crystals that can span the diameter of the petri dish.

These crystals can be dehydrated through a combination of vacuum and elevated temperature. However, it is important to note that TiF_4 has a low sublimation point of 284 °C[41,42], and thus, extended vacuum or high temperatures will cause sublimation of TiF_4 simultaneously with any dehydration. Successful dehydration occurred by heating the powder to 115 °C for 1 hour on an N_2 Schlenk line, but this material is no longer crystalline. The correct 1:1:6 stoichiometry of Zn:Ti:F still remains, as evidenced by TEM EDS. Due to the sublimation of TiF_4, these materials cannot be sintered to reintroduce crystallinity.

2.3.3.2 Mechanochemical Ball Milling

Other ABF_6 phases are synthesized via mechanochemical ball milling.[43–49] Since we are directly synthesizing the anhydrous phase, all experiments are conducted under an Ar atmosphere. These methods were modified from the synthesis of $BaSnF_4$[43]. Any AF_2 and BF_4

materials can theoretically be used to synthesize ABF_6 compounds, depending on the thermodynamic stability of the ABF_6 phase and the chemical compatibility of the reagents. As an example, for the synthesis of $ZnSnF_6$, we combine stoichiometric amounts of ZnF_2 and SnF_4 to a total of 100 mg. No syntheses in which the total mass was greater than 100 mg were successful due to a low ball-to-powder ratio (BPR) in the ball mill[50,51]. The starting materials are mixed by hand for ~5 minutes to obtain a relatively homogeneous powder mixture. This mixture is placed in a 2.5 mL stainless steel ball mill jar on top of one stainless steel ball (diameter = 6.35 mm). This jar was closed with a Teflon O-ring and sealed with Kapton tape. This jar was placed into a holder and mixed using a Spex SamplePrep BM-400 Mixer/Mill. This sample is mixed in 30-minute intervals (with 30 minutes of rest in between intervals) for a total of 16 hours. The breaks are to ensure that the ball mill motor does not overheat. The resulting material, polycrystalline $ZnSnF_6$, is then pressed into a 6 mm pellet, sealed in a quartz ampoule, and sintered at 300 °C for 7 days to increase crystallinity.

2.4 Characterization Methods

Following synthesis, I have primarily used two methods to characterize a material's structure: powder X-ray diffraction (XRD) and transmission electron microscopy (TEM). To minimize sample oxidation, all samples are transferred to XRD and TEM instrument rooms in low-density polyethylene (LDPE) bags sealed with a ULINE heat sealer in an Ar-filled glovebox.

2.4.1 Powder X-ray Diffraction

XRD measurements were performed at room temperature on either a Rigaku SmartLab or PANalytical Empyrean diffractometer; both have a fixed X-ray wavelength of 1.54 Å from a Cu source. All experiments were performed in Bragg-Brentano geometry. Unless otherwise noted, all powder samples were loaded onto a quartz sample holder and covered with Kapton tape in a glovebox prior to characterization to prevent oxidation. The Kapton tape

covers the sample throughout data collection, and thus the broad Kapton peak at approximately 18° 2θ is background-subtracted for each diffractogram.

2.4.1.1 Rietveld Refinement

I have used the Rietveld method[52] to characterize the materials present in an XRD sample. The Rietveld method uses the least squares approach to match a calculated profile to the experimental pattern. This calculated profile can contain a number of inputs, including those from the instrument and X-ray source, but must include one or more crystal structure files. This profile is refined to match the peak positions, intensities, and shapes of the experimental pattern. Because this method is purely statistical (and therefore has no chemical intuition), Rietveld refinement can easily incorrectly fit the data depending on what parameters are allowed to be relaxed. Therefore, a basic understanding of the Rietveld method is essential for a user to gain an accurate quantitative understanding of their system.

Rietveld refinement uses peak position to determine unit cell parameters a, b, c, α, β, and γ. These parameters are fit via Bragg's law[53], where n is the diffraction order (1 unless otherwise stated), λ is the X-ray source wavelength (1.54 Å for all experiments herein), d_{hkl} is the spacing between two planes with given indices *hkl*, and θ is the angle of diffraction.

$$n\lambda = 2d_{hkl}\sin(\theta)$$

A structure file, typically a .cif file, can be input as a parameter for Rietveld refinement. This file includes not only a, b, c, α, β, and γ for the given structure but also the identities and positions of all atoms in the unit cell. When performing Rietveld refinement, the user can define which parameters are set and which can be refined. Unless otherwise noted, the crystal structure (i.e., space group and symmetry), preferred orientation, and site occupancies are initially fixed while the lattice parameters are relaxed. Often, this method is suitable for identifying phases and relative wt.% in a sample. When more information is needed, as is the

case with refining the Y-S patterns in Chapter 4, each of the remaining parameters is sequentially refined until the RWP is minimized.

The XRD peak intensity is primarily influenced by the structure factor and multiplicity of the crystallographic plane.[54,55] However, both of these factors will be altered if some crystallographic sites within a plane are vacant. Unit cell sites can often be partially occupied (between 0 and 1), where a random distribution of that site is either occupied or vacant. Understanding site occupancy is particularly important for rocksalt-derived electrides, where the only differences between the one-to-one rocksalt structure and the electride structure may be the occupancy of anions in certain planes. To best characterize site occupancy, I perform a full Rietveld refinement of the structure without refining site occupancy, and then refine site occupancy to best fit peak intensities.

The peak shape and width are used to determine the crystallite/domain size via the Scherrer equation[56], where τ is the mean domain size, K is a dimensionless shape factor, which is set at 0.9 for all calculations herein, and β is the full width at half maximum (FWHM) line broadening of the peak.

$$\tau = \frac{\mathrm{K}\lambda}{\beta cos\theta}$$

It is important to note that the Scherrer equation does not determine the size of powder particles but rather the size of microcrystalline domains within a powder particle. If the crystalline domains are large enough that they are broken during the powdering process, the Scherrer equation is no longer valid.

When two or more phases are present in a sample, multiple structure files can be input and refined. The peak intensities and shapes can then be used to determine the relative weight percent of each phase. This method is often used to determine the extent or yield of a reaction. In Chapter 3 of this thesis, I exclusively use this method to determine the extent of

Y_2C fluorination by refining the experimental pattern to both the Y_2C and Y_2CF_2 phases. For these experiments, the Y_2CF_2 phase often has low crystallinity and may only be present in small amounts. Rietveld refinement of these samples can thus be tricky, as the least squares approach often tries to fit the Y_2CF_2 phase to background noise rather than the true peaks. This is especially true when the background is allowed to be refined along with the calculated data.

To circumvent an incorrect fit, I have developed a set method for refining these samples. I collect data between 25º and 65º 2θ, as many identifiable peaks for both phases appear in that window, and Y_2CF_2 peaks are often indistinguishable from the background at angles higher than 65° 2θ. Additionally, this range avoids much of the broad amorphous peak associated with the Kapton tape. It is first essential to correctly fit the background prior to any refinement. This can, and often should, be done manually. Because of the Kapton tape covering the sample and the Ar filling the Kapton tape, the background of these samples does not follow the typical shape due to only instrument geometry and low-angle air scattering. Therefore, it may be necessary to include multiple background reference points that are not included in the standard background subtraction. After carefully setting the background, any subsequent Rietveld refinements should not include background refinement.

However, depending on the wt.% of Y_2CF_2, many of the peaks after 40° 2θ still may not be able to be properly fit due to their low intensities. For those samples in which the wt.% of Y_2CF_2 is low, any refinement beyond 40° 2θ adds uncertainty to the results, as the refinement least squares method may try to fit the background. Therefore, for these experiments, I fit only between 27° and 37° 2θ, which includes the two strongest peaks for both Y_2C and Y_2CF_2.

2.4.2 Transmission Electron Microscopy

Throughout my doctoral work, I have developed expertise in multiple characterization methods via transmission electron microscopy. For a more detailed study of the theory and operation of the transmission electron microscope (TEM), I point you to "Transmission Electron Microscopy" by Williams and Carter.[57] Most of my work has been completed on a ThermoScientific FEI Talos F200X scanning/transmission electron microscope (S/TEM), available at UNC. Atomic resolution high-angle annular dark field (HAADF) images of Y_6S_4 were taken on an aberration-corrected ThermoFisher Titan 80-300 scanning transmission electron microscope (STEM) at North Carolina State University. All experiments were performed at 200 kV. Both TEM instruments used have windowless EDS detectors[58] to minimize the amount of low-energy X-rays absorbed before reaching the detector.

Due to the rapid oxidation of all of my samples, TEM grids were prepared and loaded in a glovebox prior to analysis. All samples are hand-ground in an agate mortar and pestle, and 1 mg is transferred to 1-3 mL of either 1,3-dioxolane or dimethoxyethane. These solvents were chosen because they do not react with electrides[59]. Both solvents are distilled on an N_2 Schlenk line prior to use. 1,3-Dioxolane is also dried over molecular sieves while in the glovebox due to its affinity for water. For those samples in which small/thin particles are absolutely necessary (atomic resolution imaging, diffraction), powders are hand ground in 1 mL of solvent until all the solvent evaporates, and this process is repeated 5 times. This has been shown to significantly reduce particle size. Samples are then transferred to a scintillation vial and sealed with Teflon tape and parafilm. These samples are then sonicated outside of the glovebox for 30 minutes to maximize particle dispersion. After being brought back into the glovebox, 3 μL is taken from the top of the sample/solvent and dropped onto a 300 mesh Cu TEM grid with lacey carbon. Taking the volume from the top of the solvent ensures that only

the smallest dispersed particles are transferred to the TEM grid. The grid is placed into a grid box and the box is sealed in an LDPE bag to be transported to the TEM.

When specific planes are needed, a double tilt (α and β) sample holder is used. For all other samples, a single tilt (α only) sample holder is used. Transfer to the sample holder must occur quickly, as this is the only time the sample is fully exposed to air.

2.4.2.1 Imaging

Unless noted as a HAADF image, all images are bright field images taken in standard TEM mode. Lattice spacings are compared to those of a Crocidolite Asbestos sample and scaled accordingly. Lattice spacings are obtained by performing a fast Fourier transform (FFT)[60] on an area of interest and measuring the spacing in the reciprocal space pseudo-diffraction pattern. In Chapter 4, the crystallite regions were identified by isolating specific spots (corresponding to lattice planes) in the FFT. After reversing the Fourier transformation, an image including only those planes that correspond to the selected reciprocal space plot is formed. This image is colored and overlayed on top of the original image. This process was repeated for each spot visible in the FFT.

2.4.2.2 Energy Dispersive X-ray Spectroscopy

Energy dispersive X-ray spectroscopy (EDS)[61] uses characteristic X-rays emitted from the relaxation of an electron from an outer shell to a core shell of an atom. These X-rays are element-specific, and thus, by measuring the amount of X-rays emitted, we can quantify each of the elements present. Elements in the first row of the periodic table are difficult to measure quantitatively because they only produce a low-energy K peak. Heavier elements that contain multiple shells of electrons not only contain these low-energy K peaks but also higher-energy L and M peaks. Because of the low energy of K transitions, these X-rays are often reabsorbed by the sample itself or contaminants before reaching the EDS detector itself. Because light elements depend solely on these transitions, their quantitative values are often

underestimated. X-rays that must travel a longer path out of the sample also have a greater chance of being reabsorbed, and thus, the error in measuring light elements scales with the thickness of the particle. It is thus important to perform EDS measurements on thin particles, particularly when quantifying the amount of O of F in a sample.

I have also used the Monte Carlo electron flight simulator program CASINO[62,63] to model the amount of characteristic X-rays that will be absorbed by the sample depending on composition, density, and thickness. Although particles often do not have uniform thickness and other factors also play a role in the low quantification of light elements, these models offer insight into how thin particles will need to be to obtain even a qualitative measurement of these elements.

2.4.2.3 Electron Diffraction

While X-ray diffraction is ideal for measuring the bulk structural properties of a material, electron diffraction allows the structure of a specific particle, or even a crystallite, to be studied. For electron diffraction, it is essential that the chosen particle is thin[57]. If a particle is too thick, multiple crystallites may exist in the axis of the electron beam; therefore, a single diffraction pattern cannot be isolated. Once a sufficiently thin particle is found, I first perform an initial EDS scan to confirm that the particle is the target material and not a contaminant. Once the material is confirmed, I increase the magnification in bright field TEM mode to 96,000x and then turn on diffraction imaging mode. Depending on the specific particle and sample dispersion on the TEM grid, a selected area (SA) aperture is chosen and added. When particles are grouped closely together, the smallest aperture is often necessary to single out only the particle of interest. It is thus easiest to obtain clean diffraction patterns from particles that are thin, small enough to potentially be only one crystalline domain, and not physically close to any other particles on the grid.

2.4.2.3.1 Finding Zone Axes

Unlike XRD patterns, which are a combination of all orientations of particles in the sample, each electron diffraction pattern is taken on only one orientation of a single crystallite and thus only contains planes visible from its zone axis (ZA). Therefore, when the goal of electron diffraction is to visualize or measure specific planes, it may be necessary to orient the particle in a very particular way.

When a TEM sample is prepared, particles are drop cast onto the grid in a solvent that is subsequently evaporated. For rocksalt-based layered materials, specific diffraction patterns are frequently sampled. If the particle's crystal structure contains planes that are mechanically weaker than others, as is the case with layered materials, particles will often cleave into nonsymmetrical elongated shapes similar to rectangular prisms. These elongated or platelet-like shapes will thus often fall onto their broadest planar side when drop-cast onto the grid. For layered materials, this means that their zone axis on a TEM grid is often perpendicular to the layers, or 001 in a conventional unit cell. The diffraction pattern of the 001 ZA will have a hexagonal pattern and is easily identifiable. However, other ZAs may also have similar hexagonal patterns, and thus, the spacings of specific reflections can be measured and compared to expected values.

For simulations and indexing of electron diffraction patterns, the JEMS software[64] developed by Dr. Pierre Stadelmann is an extremely useful tool, and I recommend it to any TEM user. After inputting a crystal structure (.cif) file, JEMS allows the user to simulate thousands of diffraction patterns from various zone axes, as well as high-resolution images, contrast transfer functions, and converged beam patterns. A user can index a diffraction pattern in JEMS in one of two ways. If the user has some chemical intuition of potential ZAs, any diffraction pattern can be manually simulated, and the spacings of reflections can be compared to those in the experimental pattern. Alternatively, the user can use their

experimental pattern as an input in the “spot pattern indexing” tool, which compares experimental angles and spacings between reflections to those expected in predicted patterns and tabulates the patterns with the lowest error in both angle and spacing. The user can then manually search through these patterns to find the best fit.

If multiple similar patterns exist, tilting the sample and obtaining diffraction patterns on other ZAs will confirm the orientation. However, it is important that each of these diffraction patterns is “on zone”—exactly oriented down the ZA rather than slightly tilted. When a crystal is slightly tilted off the ZA, clear diffraction spots are visible due to the large Ewald sphere of high-energy electrons. An “off-zone” diffraction pattern will still have all standard reflections, but the intensity of these spots will not decrease radially from the beam. Instead, there will be either an arc of intense reflections centered outside the visible pattern or a visible off-beam center of intensity, depending on how far the particle is from the intended ZA. The sample must simply be tilted until the center of intensity corresponds to the center of the diffraction pattern, meaning that the crystal is exactly on the zone axis. After two on-zone diffraction patterns are taken and their respective α and β tilts are recorded, the exact orientation of the particle can be determined.

All ZAs have orientational relationships with one another, which can be visualized in a stereogram, as shown in Figure 2-4a. However, many DPs contain similar reflections and are indistinguishable by manual measurement alone. To determine the ZA of an uncertain pattern such as this, the sample should be tilted until the crystal is on another ZA. Once a unique diffraction pattern is taken (i.e., there is no uncertainty in the ZA of the crystal), the stereogram can be used to verify the ZA of another undetermined diffraction pattern by checking the relative angles between them.

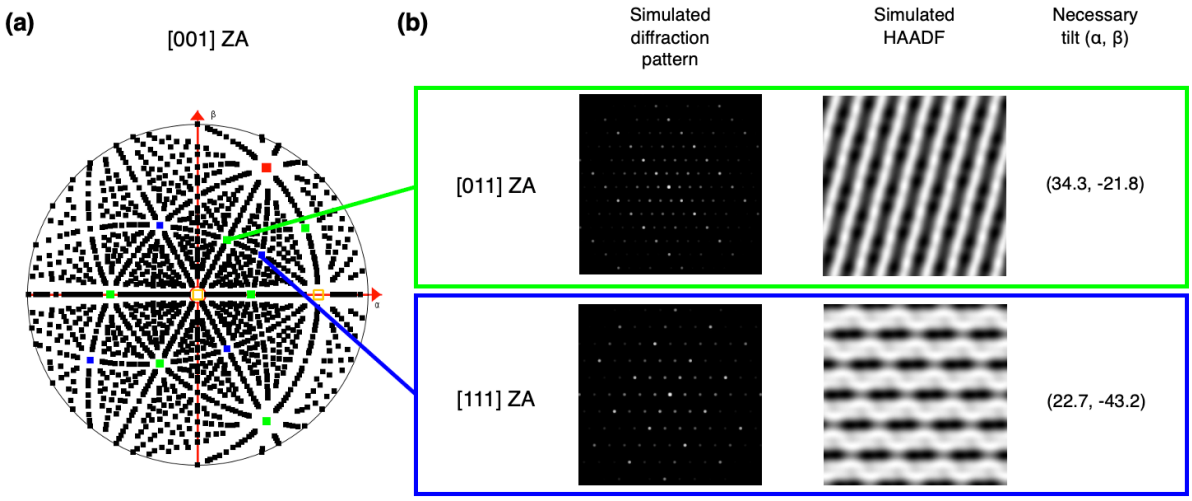


Figure 2-4. JEMS[64] example for finding ZA. (a) JEMS stereogram of the 001 ZA. Each square on the stereogram represents a ZA. The colored ZAs are those with the lowest indices. **(b)** Example ZAs from the stereogram. JEMS can produce simulated diffraction patterns and HAADF images, and the exact tilt needed to reach the desired ZA from the current ZA is determined.

Often, particles need to be tilted to specific orientations to image specific planes, as is the case in both Chapters 4 and 5 of this thesis. To find a specific ZA, two on-zone patterns must first be captured, their tilts recorded, and their ZAs correctly assigned. These two ZAs and their corresponding tilts can be input to the "goniometer" function of JEMS, which uses a stereogram similar to that in Figure 2-4a to correctly orient the simulation. It is necessary to input two ZAs, as the rotational orientation around the center of the stereogram is unknown from a single pattern. After the crystal orientation has been fully indexed, any desired ZA can be chosen, and the necessary tilts to reach this zone from the current orientation will be output by the JEMS program (Figure 2-4b).

REFERENCES

(1) Hafner, J. Ab-Initio Simulations of Materials Using VASP: Density-Functional Theory and Beyond. *J. Comput. Chem.* **2008**, *29*, 2044–2078.

(2) Kresse, G.; Furthmüller, J. Efficient Iterative Schemes for *Ab Initio* Total-Energy Calculations Using a Plane-Wave Basis Set. *Phys. Rev. B* **1996**, *54*, 11169–11186.

(3) Blöchl, P. E. Projector Augmented-Wave Method. *Phys. Rev. B* **1994**, *50*, 17953–17979.

(4) Wang, V.; Xu, N.; Liu, J.-C.; Tang, G.; Geng, W.-T. VASPKIT: A User-Friendly Interface Facilitating High-Throughput Computing and Analysis Using VASP Code. *Comput. Phys. Commun.* **2021**, 108033.

(5) Ong, S. P.; Richards, W. D.; Jain, A.; Hautier, G.; Kocher, M.; Cholia, S.; Gunter, D.; Chevrier, V. L.; Persson, K. A.; Ceder, G. Python Materials Genomics (Pymatgen): A Robust, Open-Source Python Library for Materials Analysis. *Comp. Mater. Sci.* **2013**, *68*, 314–319.

(6) Sundberg, J. D.; Benjamin, S. S.; McRae, L. M.; Warren, S. C. Simmate: A Framework for Materials Science. *JOSS* **2022**, *7*, 4364.

(7) A NEW FRAMEWORK FOR MATERIAL INFORMATICS AND ITS APPLICATION TOWARD ELECTRIDE-HALIDE MATERIAL SYSTEMS https://cdr.lib.unc.edu/concern/dissertations/r494vw405 (accessed Jul 5, 2024).

(8) Perdew, J. P.; Burke, K.; Ernzerhof, M. Generalized Gradient Approximation Made Simple. *Phys. Rev. Lett.* **1996**, *77*, 3865–3868.

(9) Perdew, J. P.; Ruzsinszky, A.; Csonka, G. I.; Vydrov, O. A.; Scuseria, G. E.; Constantin, L. A.; Zhou, X.; Burke, K. Restoring the Density-Gradient Expansion for Exchange in Solids and Surfaces. *Phys. Rev. Lett.* **2008**, *100*, 136406.

(10) Lucero, M. J.; Henderson, T. M.; Scuseria, G. E. Improved Semiconductor Lattice Parameters and Band Gaps from a Middle-Range Screened Hybrid Exchange Functional. *J. Phys. Condens. Matter* **2012**, *24*, 145504.

(11) Krukau, A. V.; Vydrov, O. A.; Izmaylov, A. F.; Scuseria, G. E. Influence of the Exchange Screening Parameter on the Performance of Screened Hybrid Functionals. *J. Chem. Phys.* **2006**, *125*, 224106.

(12) Savin, A.; Nesper, R.; Wengert, S.; Fässler, T. F. ELF: The Electron Localization Function. *Angew. Chem. Int. Ed* **1997**, *36*, 1808–1832.

(13) Stukowski, A. Visualization and Analysis of Atomistic Simulation Data with OVITO–the Open Visualization Tool. *Modelling Simul. Mater. Sci. Eng.* **2010**, *18*, 015012.

(14) Jain, A.; Ong, S. P.; Hautier, G.; Chen, W.; Richards, W. D.; Dacek, S.; Cholia, S.; Gunter, D.; Skinner, D.; Ceder, G.; Persson, K. A. Commentary: The Materials Project: A

Materials Genome Approach to Accelerating Materials Innovation. *APL Mater.* **2013**, *1*, 011002.

(15) Le, T. C.; Winkler, D. A. Discovery and Optimization of Materials Using Evolutionary Approaches. *Chem. Rev.* **2016**, *116*, 6107–6132.

(16) Glass, C. W.; Oganov, A. R.; Hansen, N. USPEX—Evolutionary Crystal Structure Prediction. *Comput. Phys. Commun.* **2006**, *175*, 713–720.

(17) Jónsson, H.; Mills, G.; Jacobsen, K. W. Nudged Elastic Band Method for Finding Minimum Energy Paths of Transitions. In *Classical and Quantum Dynamics in Condensed Phase Simulations*; Berne, B. J.; Ciccotti, G.; Coker, D. F., Eds.; World Scientific, 1998; pp. 385–404.

(18) Henkelman, G.; Uberuaga, B. P.; Jónsson, H. A Climbing Image Nudged Elastic Band Method for Finding Saddle Points and Minimum Energy Paths. *J. Chem. Phys.* **2000**, *113*, 9901–9904.

(19) Publication Series of the John von Neumann Institute for Computing (NIC) NIC Series Volume.

(20) He, X.; Zhu, Y.; Epstein, A.; Mo, Y. Statistical Variances of Diffusional Properties from Ab Initio Molecular Dynamics Simulations. *npj Comput. Mater.* **2018**, *4*, 18.

(21) Mo, Y.; Ong, S. P.; Ceder, G. Insights into Diffusion Mechanisms in P2 Layered Oxide Materials by First-Principles Calculations. *Chem. Mater.* **2014**, *26*, 5208–5214.

(22) Druffel, D. L.; Lanetti, M. G.; Sundberg, J. D.; Pawlik, J. T.; Stark, M. S.; Donley, C. L.; McRae, L. M.; Scott, K. M.; Warren, S. C. Synthesis and Electronic Structure of a 3D Crystalline Stack of MXene-Like Sheets. *Chem. Mater.* **2019**, *31*, 9788–9796.

(23) Maeda, K.; Wakayama, H.; Washio, Y.; Ishikawa, A.; Okazaki, M.; Nakata, H.; Matsuishi, S. Visible-Light-Induced Photocatalytic Activity of Stacked MXene Sheets of $Y_2 CF_2$. *J. Phys. Chem. C* **2020**, *124*, 14640–14645.

(24) Khorasani Baghini, Z.; Mostafaei, A.; Abbasnejad, M. Y2CF2 and Lu2CF2 MXenes under Applied Strain: Electronic, Optical, and Photocatalytic Properties. *J Alloys Compd* **2022**, *922*, 166198.

(25) Zhang, X.; Xiao, Z.; Lei, H.; Toda, Y.; Matsuishi, S.; Kamiya, T.; Ueda, S.; Hosono, H. Two-Dimensional Transition-Metal Electride Y_2 C. *Chem. Mater.* **2014**, *26*, 6638–6643.

(26) Weinstock, B.; Weaver, E. E.; Knop, C. P. The Xenon-Fluorine System. *Inorg. Chem.* **1966**, *5*, 2189–2203.

(27) Tius, M. A. Xenon Difluoride in Synthesis. *Tetrahedron* **1995**, *51*, 6605–6634.

(28) Burns, R. C.; MacLeod, I. D.; O'Donnell, T. A.; Peel, T. E.; Phillips, K. A.; Waugh, A. B. Xenon Difluoride as a Selective Inorganic Fluorinating Reagent. *Journal of Inorganic and Nuclear Chemistry* **1977**, *39*, 1737–1739.

(29) Simpson, W. C.; Varekamp, P. R.; Shuh, D. K.; Yarmoff, J. A. Soft X-Ray Photoelectron Spectroscopy Study of the Reaction of XeF2 with GaAs. *J. Vac. Sci. Technol. A* **1995**, *13*, 1709–1713.

(30) Hills, M. M. The Interaction of XeF2 with Sapphire. *Appl. Surf. Sci.* **1994**, *78*, 165–177.

(31) Burgess, J. S.; Baldwin, J. W.; Robinson, J. T.; Bulat, F. A.; Houston, B. H. Fluorinated Carbon Nanomaterials: Xef_2 Fluorination of Graphene. In *Fluorine-Related Nanoscience with Energy Applications*; Nelson, D. J.; Brammer, C. N., Eds.; ACS Symposium Series; American Chemical Society: Washington, DC, 2011; Vol. 1064, pp. 11–30.

(32) Abdi, G.; Filip, A.; Krajewski, M.; Kazimierczuk, K.; Strawski, M.; Szarek, P.; Hamankiewicz, B.; Mazej, Z.; Cichowicz, G.; Leszczyński, P. J.; Fijałkowski, K. J.; Szczurek, A. Toward the Synthesis, Fluorination and Application of N-Graphyne. *RSC Adv.* **2020**, *10*, 40019–40029.

(33) Masyagutova, G. A.; Ostakhov, S. S.; Mamykin, A. V.; Ovchinnikov, M. Yu.; Fakhreeva, A. V.; Khursan, S. L. Crystallochemiluminescence Accompanying the Fluorination of Europium (III) Nitrate by Xenon Difluoride in Acetonitrile Solution. *J. Fluor. Chem.* **2019**.

(34) Zhang, W.; Spinelle, L.; Dubois, M.; Guérin, K.; Kharbache, H.; Masin, F.; Kharitonov, A. P.; Hamwi, A.; Brunet, J.; Varenne, C.; Pauly, A.; Thomas, P.; Himmel, D.; Mansot, J. L. New Synthesis Methods for Fluorinated Carbon Nanofibres and Applications. *J. Fluor. Chem.* **2010**, *131*, 676–683.

(35) Bardin, V. V.; Adonin, N. Yu. Reactions of Aromatic Compounds with Xenon Difluoride. *Russ. J. Org. Chem.* **2016**, *52*, 1400–1407.

(36) Hills, M. M.; Arnold, G. S. Chemical Treatment of Fused Silica with Xenon Difluoride. *Appl. Surf. Sci.* **1991**, *47*, 77–90.

(37) Sugawara, K.; Wach, Th.; Wanner, J.; Jakob, P. Desorption Kinetics of Copper Fluorides in the Reaction of Fluorine with Copper Surfaces. *J. Chem. Phys.* **1995**, *102*, 544–550.

(38) High-density polyethylene (HDPE) | Linseis Messgeräte GmbH https://www.linseis.com/en/wiki-en/high-density-polyethylene-hdpe-an-inside-look/ (accessed Jul 5, 2024).

(39) McRae, L. M.; Radomsky, R. C.; Pawlik, J. T.; Druffel, D. L.; Sundberg, J. D.; Lanetti, M. G.; Donley, C. L.; White, K. L.; Warren, S. C. Sc2c, a 2D Semiconducting Electride. *J. Am. Chem. Soc.* **2022**, *144*, 10862–10869.

(40) Chattopadhyay, T.; Devreux, F.; Peters, K.; Peters, E. M.; Gmelin, E.; Ghosh, B. Crystal Structure and Phase Transitions in $MnTiF_6$.$6H_2$ O and $ZnTiF_6$.$6H_2$ O. *J. Phys. C: Solid State Phys.* **1988**, *21*, 1321–1334.

(41) Zmbov, K. F.; Margrave, J. L. Mass Spectrometric Studies at High Temperatures. XVI. Sublimation Pressures for Titanium(III)Fluoride and the Stabilities of TiF2(g) and TiF(g). *J. Phys. Chem.* **1967**, *71*, 2893–2895.

(42) Oota, T.; Yamai, I.; Yokoyama, M. Vapor Phase Growth of Titania Whiskers by Hydrolysis of Titanium Flouride. *J. Cryst. Growth* **1984**, *66*, 262–268.

(43) Liu, L.; Yang, L.; Liu, M.; Li, X.; Shao, D.; Luo, K.; Wang, X.; Luo, Z. SnF2-Based Fluoride Ion Electrolytes MSnF4 (M = Ba, Pb) for the Application of Room-Temperature Solid-State Fluoride Ion Batteries. *J Alloys Compd* **2020**, *819*, 152983.

(44) Nowroozi, M. A.; Mohammad, I.; Molaiyan, P.; Wissel, K.; Munnangi, A. R.; Clemens, O. Fluoride Ion Batteries – Past, Present, and Future. *J. Mater. Chem. A* **2021**.

(45) Achary, K. R.; Rao, Y. B.; Kamadurai, R. K.; Patro, L. N. Mechanochemical Synthesis and Fluoride Ion Conductivity Studies in $Srsnf_4$ Polymorphs. *J. Phys. Chem. C* **2023**.

(46) Preishuber-Pflügl, F.; Wilkening, M. Mechanochemically Synthesized Fluorides: Local Structures and Ion Transport. *Dalton Trans.* **2016**, *45*, 8675–8687.

(47) Heise, M.; Scholz, G.; Düvel, A.; Heitjans, P.; Kemnitz, E. Mechanochemical Synthesis, Structure, and Properties of Solid Solutions of Alkaline Earth Metal Fluorides: Ma1−xMbxF2 (M: Ca, Sr, Ba). *Solid State Sciences* **2016**, *60*, 65–74.

(48) Lee, J.; Zhang, Q.; Saito, F. Mechanochemical Synthesis of Ternary Fluorides with Perovskite Structures. *Chem. Lett.* **2001**, *30*, 700–701.

(49) Read, J. A.; Behl, W. K. Mechanochemical Synthesis of Carbon Fluorides. *Electrochem. Solid-State Lett.* **2009**, *12*, A16.

(50) Salili, S. M.; Ataie, A.; Sadighi, Z.; Aslan, M. H.; Oral, A. Y.; Ozer, M.; Çaglar, S. H. Effect of Ball Size and Ball to Powder Ratio Variation on Crystallite Size and Formation of Nanocrystalline Materials in Planetary Ball Mill. In; AIP Conference Proceedings; AIP, 2011; pp. 127–130.

(51) Kuziora, P.; Wyszyńska, M.; Polanski, M.; Bystrzycki, J. Why the Ball to Powder Ratio (BPR) Is Insufficient for Describing the Mechanical Ball Milling Process. *Int. J. Hydrogen Energy* **2014**, *39*, 9883–9887.

(52) Rietveld, H. M. The Rietveld Method. *Phys. Scr.* **2014**, *89*, 098002.

(53) Jauncey, G. E. The Scattering of X-Rays and Bragg's Law. *Proc Natl Acad Sci USA* **1924**, *10*, 57–60.

(54) March, A. Mathematische Theorie Der Regelung Nach Der Korngestah Bei Affiner Deformation. *Z. Kristallogr. Cryst. Mater.* **1932**, *81*, 285–297.

(55) Introduction to Diffraction in Materials Science and Engineering | Wiley https://www.wiley.com/en-be/Introduction+to+Diffraction+in+Materials+Science+and+Engineering-p-9780471247241 (accessed Jul 5, 2024).

(56) P, S. Bestimmung Der Grosse Und Inneren Struktur von Kolloidteilchen Mittels Rontgenstrahlen. *Nach Ges Wiss Gottingen* **1918**.

(57) *Transmission Electron Microscopy*; Carter, C. B.; Williams, D. B., Eds.; Springer International Publishing: Cham, 2016.

(58) Schlossmacher, P.; Klenov, D. O.; Freitag, B.; von Harrach, H. S. Enhanced Detection Sensitivity with a New Windowless XEDS System for AEM Based on Silicon Drift Detector Technology. *Micros. Today* **2010**, *18*, 14–20.

(59) Druffel, D. L.; Kuntz, K. L.; Woomer, A. H.; Alcorn, F. M.; Hu, J.; Donley, C. L.; Warren, S. C. Experimental Demonstration of an Electride as a 2D Material. *J. Am. Chem. Soc.* **2016**, *138*, 16089–16094.

(60) Nussbaumer, H. J. The Fast Fourier Transform. In *Fast fourier transform and convolution algorithms*; Springer series in information sciences; Springer Berlin Heidelberg: Berlin, Heidelberg, 1982; Vol. 2, pp. 80–111.

(61) Shindo, D.; Oikawa, T. Energy Dispersive X-Ray Spectroscopy. In *Analytical electron microscopy for materials science*; Springer Japan: Tokyo, 2002; pp. 81–102.

(62) Hovington, P.; Drouin, D.; Gauvin, R. CASINO: A New Monte Carlo Code in C Language for Electron Beam Interaction -Part I: Description of the Program. *Scanning* **2006**, *19*, 1–14.

(63) Drouin, D.; Hovington, P.; Gauvin, R. CASINO: A New Monte Carlo Code in C Language for Electron Beam Interactions—Part II: Tabulated Values of the Mott Cross Section. *Scanning* **1997**, *19*, 20–28.

(64) Stadelmann, P. Image Analysis and Simulation Software in Transmission Electron Microscopy. *Microsc. Microanal.* **2003**, *9*, 60–61.

CHAPTER 3: 3D MXENE SYNTHESIS VIA FLUORINATION OF AN ELECTRIDE

3.1 Introduction

Crystalline stacked MXene sheets (3D MXenes) have gained increasing attention due to their unique semiconducting and photocatalytic properties, along with their improved crystallinity and kinetics compared to those of their 2D MXene counterparts[1–6]. However, the current synthetic strategies for 3D crystalline MXenes are high-temperature, either via solid-state or chemical vapor deposition (CVD) synthesis, which limits the accessibility of phases that are not stable at high temperatures[7,8]. Therefore, developing a room-/low-temperature method for synthesizing 3D MXenes would not only increase the synthetic efficiency of currently known phases but also open up an avenue for synthesizing metastable 3D MXenes. The potential applications of these materials are manifold—including photocatalysis and energy storage, as well as for precursors for exfoliation into new 2D MXenes[2,3,9].

It has been noted previously that MXenes are structurally related to electrides[9,10], or crystalline materials with bare electrons occupying distinct lattice sites. For example, the 3D MXene Y_2CF_2 is similar to the electride $Y_2C^{2+}[e^-]_2$, with either fluoride ions or electride electrons occupying layers between sheets of Y_2C, as shown in Figure 3-1.

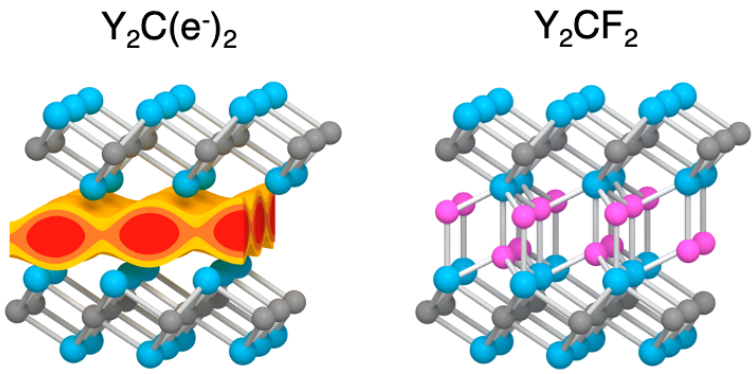


Figure 3-1. The Y_2C electride and 3D MXene Y_2CF_2. The blue atoms represent Y, the gray atoms represent C, and the pink atoms represent F. Red/orange/yellow isosurfaces represent electron localization at electride sites.

However, the extreme reducing nature of the accessible bare electrons makes it difficult to carry out controlled, reproducible reactions with electrides. There have been some successful attempts to promote electride conversion reactions, such as halogenation of Ca_2N, Sr_2N, and Ba_2N electrides or reactions between mayenite and H_2, Au, or NH_3 to reduce the additive to an anion (H^-, Au^-, or NH_2^-)[11–16]. However, these cases are limited and not generalizable and all occur at high temperatures. Therefore, developing a method for the controlled reactions of highly reducing electrides would allow for the exploration of converting electrides into other exotic materials with distinct properties.

Here, we demonstrate the direct fluorination of an electride to yield a 3D MXene. By exposing the Y_2C electride to gaseous XeF_2[17–24], we are able to fully fluorinate Y_2C to form the 3D MXene Y_2CF_2. We have observed that the kinetic barrier for this conversion is low, only requiring modest temperatures (<120 °C) and even proceeding at room temperature. This method for synthesizing 3D MXenes via direct halogenation of electrides may unlock a new class of highly ordered crystalline 3D MXenes with unique properties and applications in sensing, electronics, and energy storage.

3.2 Full Conversion from an Electride to a 3D MXene

We chemically fluorinated Y_2C in the presence of XeF_2 gas in a quartz tube sealed with a stainless steel ball valve (Figure 2-2) under an Ar atmosphere. To prevent the solid Y_2C and solid XeF_2 from reacting in the solid phase, XeF_2 crystals were placed in an alumina ampoule and packed with SiO_2 wool. After being placed in a furnace at 60 °C for 12 hours, all Y_2C was fully converted to Y_2CF_2 with no discernable side reactions or products. We confirmed this reaction via X-ray diffraction (XRD) and Rietveld refinement[25], as shown in Figure 3-2. Y_2C fully converts to Y_2CF_2 at temperatures between 50 ºC and 150 ºC, above which we have observed the formation of YF_3. Therefore, all studies reported herein were performed at temperatures less than 120 °C.

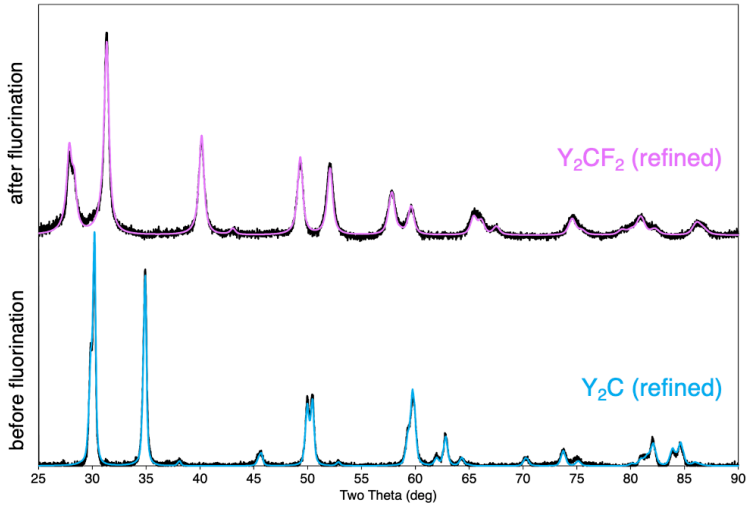


Figure 3-2. XRD of Y_2C before and after exposure to XeF_2. Before fluorination (bottom, blue), Rietveld refinement matches all peaks to the Y_2C structure. After fluorination (top, pink), all Y_2C peaks disappear, and new polycrystalline crystalline Y_2CF_2 is present.

The peaks in post-fluorination Y_2CF_2 are broader than those of the Y_2C reagent, indicating smaller crystallite sizes. The Scherrer equation[26] (2.4) was used to calculate domains of ~22.9 nm in the Y_2C sample before fluorination (blue) and domains of ~15.2 nm in the synthesized Y_2CF_2 (pink). We hypothesize that this decrease in domain size is due to

the ease of nucleating the Y2CF2 phase, which could occur at multiple locations within a single Y2C domain.

It is important to note that the quality and degree of oxidation of the initial Y_2C electride greatly influence the kinetics of fluorination. In air, Y_2C will fully react with O_2 to form Y_2O_3 and amorphous C on the minute-to-hour timescale due to the extreme reducing nature of the electride electrons[27,28]. Even in a glovebox with <1 ppm O_2, a coating of Y_2O_3 will form on the surface of Y_2C particles within minutes, as evidenced by X-ray photoelectron spectroscopy (XPS).

Figure 3-3 shows an example of two fluorinations of Y_2C with identical parameters: 90 °C for 45 minutes, with one reaction run with freshly synthesized Y_2C and the other with Y_2C that had been in the glovebox for 14 days. The reaction run with oxidized Y_2C hardly fluorinated at all, with Rietveld refinement showing that the product contained just 14.7% Y_2CF_2. The identical reaction run with freshly synthesized Y_2C, on the other hand, was refined to have 72.5% Y_2CF_2. We therefore observed that Y_2C stored in a glovebox, even in ingot form, is oxidized enough to significantly hinder fluorination.

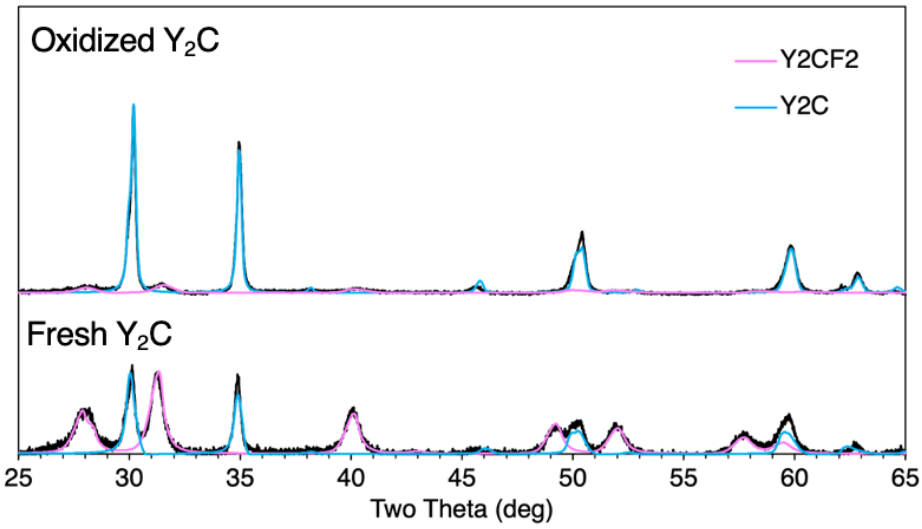


Figure 3-3. XRD of the fluorination of fresh (bottom) and oxidized (top) Y_2C. Each sample was refined via Rietveld refinement to the Y_2C (blue) and Y_2CF_2 (pink) structures.

We also note that when the initial Y_2C material is synthesized from low-quality (oxidized) Y metal, subsequent fluorination of the Y_2C does not proceed, even when performed immediately after synthesis. This suggests that oxygen species within the particles play an even larger role than those on the surface in hindering diffusion kinetics of fluoride. We therefore performed all subsequent experiments on Y_2C synthesized with high-quality Y metal and stored in the glovebox in ingot form, decreasing the Y_2C surface area exposed to the glovebox atmosphere. We also consider that there may be contamination of the Y_2C ingot by species other than O_2. For example, water vapor within the glovebox could both oxidize and hydrogenate the material. While oxidation is limited to the surface of the ingot, the resulting hydride could diffuse much farther into the sample, even contaminating materials stored in ingot form enough to affect fluoride diffusion. We therefore only used Y_2C freshly synthesized within 48 hours of the experiment.

3.3 Study of Solid-State Kinetics

Although an electrochemical fluorination of Y_2C was recently reported[29], these experiments must be performed in the presence of other materials such as conductive additives and electrolytes. The presence of these materials hinders the quantification of reaction kinetics of a single phase due to the potential for side-reactions or solid-solid reactions with the Y_2C. For example, it was noted that some Y_2CF_2 was formed when preparing the electrode, as ball milling Y_2C and the electrolyte $Ca_{0.5}Ba_{0.5}F_2$ led to some reaction between the two species[29]. We therefore sought to measure the activation (E_a) of fluorination of Y_2C via our gas-phase method using the Arrhenius method. The Arrhenius equation is classically written in the following form, where k is the rate constant, A is a preexponential factor, K_B constant, and T is the temperature in Kelvin:

$$k = Ae^{E_a/K_BT} \tag{3.1}$$

It is therefore necessary to determine a rate constant, *k*, for the fluorination of Y_2C which depends on temperature. We use the Avrami method[30–34], which describes solid-state nucleation and transformation reactions at a constant temperature:

$$y(t) = 1 - e^{-kt^n} \tag{3.2}$$

where *y(t)* is the extent of reaction at time *t* and *n* is the Avrami exponent. The extent of reaction *y(t)* has been determined in the literature by a number of characterization methods[31,35–38]; we use the wt.% of our Y_2CF_2 product determined by Rietveld refinement for this study. It is important to note that using wt.% Y_2CF_2 as a measure of the extent of reaction is an approximation. It has been computationally predicted that some F^- can intercalate into the Y_2C ABC-stacked structure before a phase transformation to the fully fluorinated AA-stacked Y_2CF_2 structure[29]. As a result, some fluorine may intercalate into Y_2C but not be captured by our method. To test this hypothesis, we performed an experiment in which only 15% of the stoichiometric ratio of XeF_2 was added to the reactor, and the reaction was allowed to proceed at 90 °C for 4 hours. After the reaction, Rietveld refinement revealed 13.4% Y_2CF_2 (Figure A-1), which is close to complete conversion within error. This experiment also gave insight into the kinetics and timescale of fluorination, as the experiment run at 90 °C for 4 hours came nearly to completion.

Uncertainty may also exist in the Rietveld refinement itself, especially in samples with less than 10% Y_2CF_2. The as-synthesized Y_2CF_2 crystallites are small and have broad XRD peaks as a result. Especially at high angles, some peaks may be less than 3 times the intensity of the background and thus difficult to identify. To avoid mischaracterization due to noise, we chose reaction times and temperatures such that the extent of reaction was greater than 10% Y_2CF_2.

To study the kinetics of the reaction, we performed fluorinations at five temperatures ranging between 50 °C and 90 °C. These temperatures were chosen such that the extent of reaction was between 10% and 80% and that this occurred between 15 and 100 minutes. To precisely measure the time and temperature of the reaction, we performed these experiments in an HDPE reactor on a hot plate in an Ar-filled glovebox (Figure 2-3). Figure 3-4 shows the extents of reaction of 13 experimental trials at various times and temperatures. Each temperature also has a data point at 0 minutes, corresponding to a y-intercept of 100% Y_2C. First-order reaction kinetics are assumed due to the predicted intercalation mechanism of F^- into Y_2C, and thus *ln(y)* vs. time is assumed to be linear.

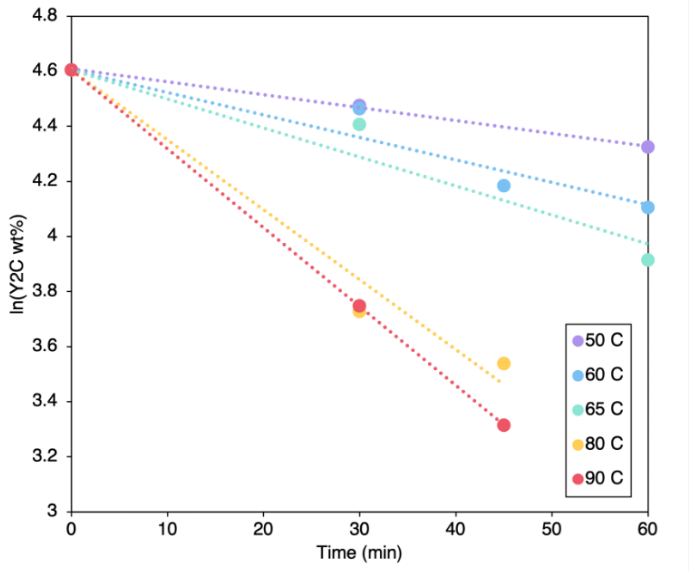


Figure 3-4. Extents of Y2C fluorination. Rietveld refinement was used to determine the amount of Y_2C remaining in the sample, which is plotted as ln(y) here.

To determine the reaction rate constant for each temperature, the Avrami equation (3.2) can be linearized to the following form[34]:

$$\ln\left[\ln\left(\frac{1}{1-y}\right)\right] = n\ln[k] + n\ln[t]. \tag{3.3}$$

This linearization was performed for each reaction temperature, as shown in Figure 3-5. The value of *n*, the Avrami exponent, is dependent on the dimensionality and process of crystal

growth, where values of 0.5-1.5 are attributed to diffusion-controlled transformations[39,40], with lower values indicating faster diffusion. We would therefore expect the value of n to decrease with increasing temperature. As *ln(t)* is the x-axis of this plot, the value of *n* can be determined simply by calculating the slope at each temperature. The value of the rate constant *k* can thus be determined from the *n*ln[k]* term of the linearized Avrami equation (3.3).

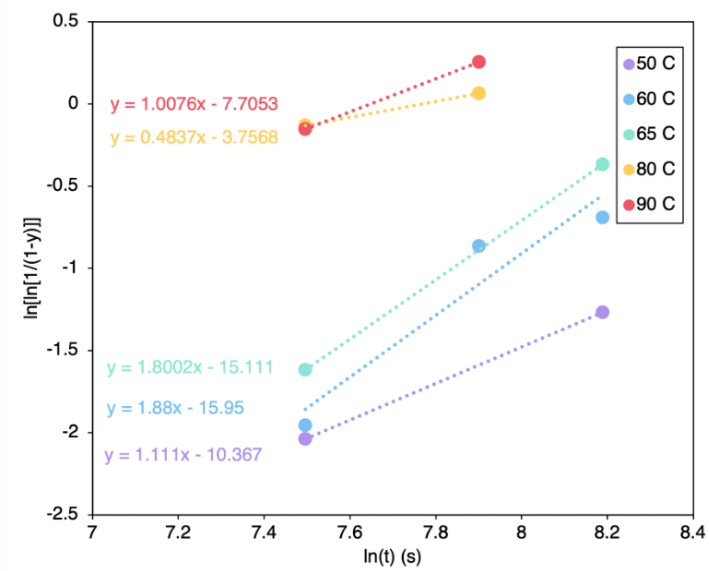


Figure 3-5. Linearized Avrami plots at each temperature. Each slope was determined by linear regression of experiments run at a corresponding temperature.

Table 3-1 lists the rate constants determined by the Avrami method for each temperature. As the temperature increases, the rate constants also trend upward, as expected for first-order reactions.

Table 3-1. Rate constants as determined via the Avrami method. Each rate constant was calculated by the linearized Avrami equation, as shown in Figure 3-5.

T (°C)	k (1/s)
50	8.86×10^{-5}
60	2.07×10^{-4}
65	2.26×10^{-4}
80	4.24×10^{-4}
90	4.77×10^{-4}

These rate constants can now be used to calculate the activation energy for diffusion via the Arrhenius equation (3.1), as shown in the Arrhenius plot of Figure 3-6.

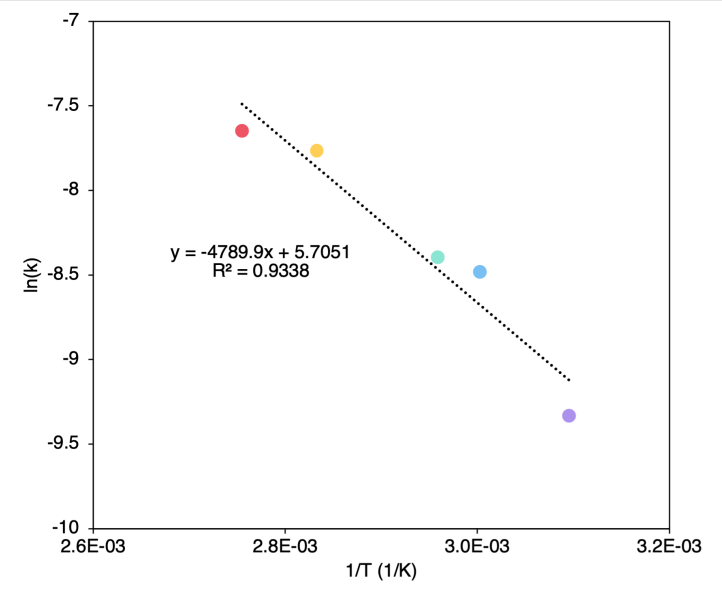


Figure 3-6. Arrhenius plot of the fluorination of Y_2C. Each data point was determined via the Avrami method described above.

We experimentally measured the activation energy for fully converting Y_2C to Y_2CF_2 to be 413 meV ± 63.5 meV from a linear regression of the Arrhenius plot. For comparison, the value calculated via NEB for F^- diffusion through the Y_2CF_2 structure is 196 meV[9]. This disagreement may be due to a variety of factors. (1) The calculated diffusion barrier takes into account only a single hopping event through the AA-stacked Y_2CF_2 structure. However, there is a possibility that the experimental formation of Y_2CF_2 depends on additional reaction steps, such as nucleation, grain-boundary hopping, the restacking from ABC-stacked Y_2C to AA-stacked Y_2CF_2, or even diffusion past a surface oxide. (2) Each rate constant was calculated from a limited number of experiments. For some temperatures, only two time points were used determine the rate constant, potentially leading to large errors. (3) It is unclear from this data whether the E_a for diffusion is dependent on temperature. The Arrhenius plot (Fig. 3-6) may instead be better fit by two distinct slopes, one at low T (50 to 65 ºC) and one at higher T (80

to 90 ºC). This conclusion cannot yet be drawn with only five experimental rate constants, and thus collecting additional data at more temperature intervals may clarify the temperature dependence of the activation energy.

3.4 Room-Temperature Conversion of Y_2C to Y_2CF_2

Although all of the previous reactions were performed below the sublimation temperature of XeF_2, which is 128 °C[41,42], gaseous XeF_2 was still able to react with Y_2C. XeF2 has a high vapor pressure, which is approximately 4.5 Torr at 25 ºC. We therefore sought to further exploit the high vapor pressure by performing this reaction at room temperature. We sealed powdered Y_2C and solid XeF_2 in a high-density polyethylene (HDPE) tube under an Ar atmosphere (glovebox) and left untouched for 28 days. Any fluorination of Y_2C is thus due to the high vapor pressure of XeF_2, as the two solids were physically separated and not allowed to contact.

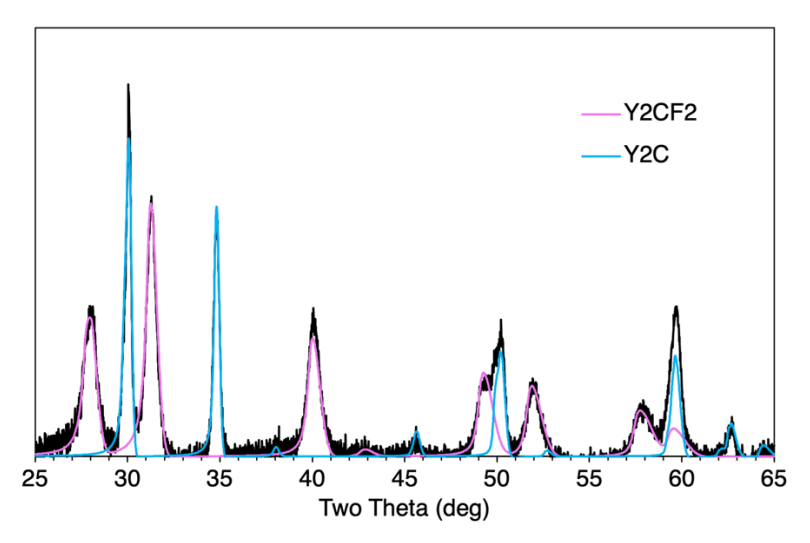


Figure 3-7. XRD pattern of Y_2CF_2 synthesized at room temperature. The blue line represents the Rietveld fit of the remaining Y_2C, and the pink line represents the Rietveld fit of Y_2CF_2.

This room temperature reaction produced Y_2CF_2, as characterized by XRD. There are some remaining characteristic Y_2C peaks, indicating an incomplete fluorination. Rietveld

refinement revealed this sample to be 67.9 wt.% Y_2CF_2. However, as this sample was removed from the HDPE tube, no XeF_2 crystals remained despite being initially present in a 2.5× stoichiometric excess, and the HDPE was slightly discolored. After opening the tube, the HDPE slowly returned to its original color after ~24 hours. We therefore hypothesize that this partial extent of fluorination is due not only to the kinetics of the reaction but also to the competitive solubility of XeF_2 in the walls of the HDPE tube. We therefore predict that if this reaction were run with either (a) more of a molar excess of XeF_2 or (b) in a reaction vessel that does not interact with XeF_2, a phase-pure synthesis of the 3D MXene Y_2CF_2 could occur at room temperature.

3.5 Conclusions

In this study, we performed the first room-temperature synthesis of a 3D crystalline MXene, Y_2CF_2 via the controlled reaction of the electride Y_2C with gaseous XeF_2. Phase-pure Y_2CF_2 was synthesized at temperatures as low as 50 ºC. We then exploited this method to study the kinetics of fluorination. Preliminary experiments suggest high rate constants, with full conversions occurring at 90 ºC in less than two hours. Additional data at multiple times and temperatures is needed to confirm the temperature-dependence of the activation energy for diffusion. This method for synthesizing 3D MXenes from electrides allows for not only lower-temperature, more efficient syntheses of 3D crystalline MXenes, but also a method to study the kinetics of solid-state diffusion in solid-state materials without the need for an electrolyte.

REFERENCES

(1) Yun, Q.; Lu, Q.; Zhang, X.; Tan, C.; Zhang, H. Three-Dimensional Architectures Constructed from Transition-Metal Dichalcogenide Nanomaterials for Electrochemical Energy Storage and Conversion. *Angew. Chem. Int. Ed* **2018**, *57*, 626–646.

(2) Li, K.; Liang, M.; Wang, H.; Wang, X.; Huang, Y.; Coelho, J.; Pinilla, S.; Zhang, Y.; Qi, F.; Nicolosi, V.; Xu, Y. 3D Mxene Architectures for Efficient Energy Storage and Conversion. *Adv. Funct. Mater.* **2020**, *30*.

(3) Khorasani Baghini, Z.; Mostafaei, A.; Abbasnejad, M. Y2CF2 and Lu2CF2 MXenes under Applied Strain: Electronic, Optical, and Photocatalytic Properties. *J Alloys Compd* **2022**, *922*, 166198.

(4) Maeda, K.; Wakayama, H.; Washio, Y.; Ishikawa, A.; Okazaki, M.; Nakata, H.; Matsuishi, S. Visible-Light-Induced Photocatalytic Activity of Stacked MXene Sheets of Y_2CF_2. *J. Phys. Chem. C* **2020**, *124*, 14640–14645.

(5) Li, K.; Wang, X.; Li, S.; Urbankowski, P.; Li, J.; Xu, Y.; Gogotsi, Y. An Ultrafast Conducting Polymer@MXene Positive Electrode with High Volumetric Capacitance for Advanced Asymmetric Supercapacitors. *Small* **2020**, *16*, e1906851.

(6) Zhan, C.; Naguib, M.; Lukatskaya, M.; Kent, P. R. C.; Gogotsi, Y.; Jiang, D.-E. Understanding the Mxene Pseudocapacitance. *J. Phys. Chem. Lett.* **2018**, *9*, 1223–1228.

(7) Druffel, D. L.; Lanetti, M. G.; Sundberg, J. D.; Pawlik, J. T.; Stark, M. S.; Donley, C. L.; McRae, L. M.; Scott, K. M.; Warren, S. C. Synthesis and Electronic Structure of a 3D Crystalline Stack of MXene-Like Sheets. *Chem. Mater.* **2019**, *31*, 9788–9796.

(8) Wang, D.; Zhou, C.; Filatov, A. S.; Cho, W.; Lagunas, F.; Wang, M.; Vaikuntanathan, S.; Liu, C.; Klie, R. F.; Talapin, D. V. Direct Synthesis and Chemical Vapor Deposition of 2D Carbide and Nitride MXenes. *Science* **2023**, *379*, 1242–1247.

(9) Druffel, D. L.; Pawlik, J. T.; Sundberg, J. D.; McRae, L. M.; Lanetti, M. G.; Warren, S. C. First-Principles Prediction of Electrochemical Electron-Anion Exchange: Ion Insertion without Redox. *J. Phys. Chem. Lett.* **2020**, *11*, 9210–9214.

(10) Bae, S.; Espinosa-García, W.; Kang, Y.; Egawa, N.; Lee, J.; Kuwahata, K.; Khazaei, M.; Ohno, K.; Kim, Y.; Han, M. J.; Hosono, H.; Dalpian, G. M.; Raebiger, H. MXene Phase with C_3 Structure Unit: A Family of 2D Electrides. *Adv. Funct. Mater.* **2021**, *31*, 2100009.

(11) Miyakawa, M.; Kamioka, H.; Hirano, M.; Kamiya, T.; Sushko, P. V.; Shluger, A. L.; Matsunami, N.; Hosono, H. Photoluminescence from Au Ion-Implanted Nanoporous Single-Crystal. *Phys. Rev. B* **2006**, *73*, 205108.

(12) Nakao, T.; Ogasawara, K.; Kitano, M.; Matsuishi, S.; Sushko, P. V.; Hosono, H. Ship-in-a-Bottle Synthesis of High Concentration of N2 Molecules in a Cage-Structured Electride. *J. Phys. Chem. Lett.* **2021**, *12*, 1295–1299.

(13) Hayashi, K.; Matsuishi, S.; Kamiya, T.; Hirano, M.; Hosono, H. Light-Induced Conversion of an Insulating Refractory Oxide into a Persistent Electronic Conductor. *Nature* **2002**, *419*, 462–465.

(14) Bailey, A. S.; Hughes, R. W.; Hubberstey, P.; Ritter, C.; Smith, R. I.; Gregory, D. H. New Ternary and Quaternary Barium Nitride Halides; Synthesis and Crystal Chemistry. *Inorg. Chem.* **2011**, *50*, 9545–9553.

(15) Bowman, A.; Smith, R. I.; Gregory, D. H. Synthesis and Structure of the Ternary and Quaternary Strontium Nitride Halides, Sr2N(X, X′) (X, X′=Cl, Br, I). *J. Solid State Chem.* **2006**, *179*, 130–139.

(16) Bowman, A.; Mason, P. V.; Gregory, D. H. Heteroanionic Intercalation into Positively Charged Inorganic Hosts: The First Nitride Mixed Halides. *Chem. Commun.* **2001**, 1650–1651.

(17) Hills, M. M. The Interaction of XeF2 with Sapphire. *Appl. Surf. Sci.* **1994**, *78*, 165–177.

(18) Hills, M. M.; Arnold, G. S. Chemical Treatment of Fused Silica with Xenon Difluoride. *Appl. Surf. Sci.* **1991**, *47*, 77–90.

(19) Zhang, W.; Spinelle, L.; Dubois, M.; Guérin, K.; Kharbache, H.; Masin, F.; Kharitonov, A. P.; Hamwi, A.; Brunet, J.; Varenne, C.; Pauly, A.; Thomas, P.; Himmel, D.; Mansot, J. L. New Synthesis Methods for Fluorinated Carbon Nanofibres and Applications. *J. Fluor. Chem.* **2010**, *131*, 676–683.

(20) Bardin, V. V.; Adonin, N. Yu. Reactions of Aromatic Compounds with Xenon Difluoride. *Russ. J. Org. Chem.* **2016**, *52*, 1400–1407.

(21) Masyagutova, G. A.; Ostakhov, S. S.; Mamykin, A. V.; Ovchinnikov, M. Yu.; Fakhreeva, A. V.; Khursan, S. L. Crystallochemiluminescence Accompanying the Fluorination of Europium (III) Nitrate by Xenon Difluoride in Acetonitrile Solution. *J. Fluor. Chem.* **2019**.

(22) Burns, R. C.; MacLeod, I. D.; O'Donnell, T. A.; Peel, T. E.; Phillips, K. A.; Waugh, A. B. Xenon Difluoride as a Selective Inorganic Fluorinating Reagent. *Journal of Inorganic and Nuclear Chemistry* **1977**, *39*, 1737–1739.

(23) Tius, M. A. Xenon Difluoride in Synthesis. *Tetrahedron* **1995**, *51*, 6605–6634.

(24) Pattanathummasid, C.; Yasufuku, N.; Asahi, R.; Kutana, A.; Hagihara, M.; Mori, K.; Takami, T. Topochemical Fluoride Exchange Reaction with Anionic Electrons toward Fluoride-Ion Conduction in Layered Ba_{2-} A NF_{1-} (A = Na, K). *Chem. Mater.* **2024**.

(25) Rietveld, H. M. The Rietveld Method. *Phys. Scr.* **2014**, *89*, 098002.

(26) P, S. Bestimmung Der Grosse Und Inneren Struktur von Kolloidteilchen Mittels Rontgenstrahlen. *Nach Ges Wiss Gottingen* **1918**.

(27) McRae, L. M.; Radomsky, R. C.; Pawlik, J. T.; Druffel, D. L.; Sundberg, J. D.; Lanetti, M. G.; Donley, C. L.; White, K. L.; Warren, S. C. Sc2c, a 2D Semiconducting Electride. *J. Am. Chem. Soc.* **2022**, *144*, 10862–10869.

(28) Zhang, X.; Xiao, Z.; Lei, H.; Toda, Y.; Matsuishi, S.; Kamiya, T.; Ueda, S.; Hosono, H. Two-Dimensional Transition-Metal Electride Y_2 C. *Chem. Mater.* **2014**, *26*, 6638–6643.

(29) Tojigamori, T.; Matsui, N.; Suzuki, K.; Hirayama, M.; Abe, T.; Kanno, R. Fluorination/Defluorination Behavior of Y_2 C in Fluoride-Ion Battery Anodes. *ACS Appl. Energy Mater.* **2024**, *7*, 1100–1108.

(30) Johnson W., A. Reaction Kinetics in Process of Nucleation and Growth. *Transactions of Transactions of the American Institute of Mining and Metallurgical Engineers* **1939**.

(31) Málek, J. The Applicability of Johnson-Mehl-Avrami Model in the Thermal Analysis of the Crystallization Kinetics of Glasses. *Thermochim. Acta* **1995**, *267*, 61–73.

(32) Avrami, M. Kinetics of Phase Change. I General Theory. *J. Chem. Phys.* **1939**, *7*, 1103.

(33) Avrami, M. Kinetics of Phase Change. II Transformation-Time Relations for Random Distribution of Nuclei. *J. Chem. Phys.* **1940**, *8*, 212–224.

(34) Jonas, J. J.; Quelennec, X.; Jiang, L.; Martin, É. The Avrami Kinetics of Dynamic Recrystallization. *Acta Mater.* **2009**, *57*, 2748–2756.

(35) Lorenzo, A. T.; Arnal, M. L.; Albuerne, J.; Müller, A. J. DSC Isothermal Polymer Crystallization Kinetics Measurements and the Use of the Avrami Equation to Fit the Data: Guidelines to Avoid Common Problems. *Polym. Test.* **2007**, *26*, 222–231.

(36) Hillier, I. H. Modified Avrami Equation for the Bulk Crystallization Kinetics of Spherulitic Polymers. *J. Polym. Sci. A Gen. Pap.* **1965**, *3*, 3067–3078.

(37) Shirzad, K.; Viney, C. A Critical Review on Applications of the Avrami Equation beyond Materials Science. *J. R. Soc. Interface* **2023**, *20*, 20230242.

(38) Khanna, Y. P.; Taylor, T. J. Comments and Recommendations on the Use of the Avrami Equation for Physico-chemical Kinetics. *Polym. Eng. Sci.* **1988**, *28*, 1042–1045.

(39) Wollstadt, S.; De Souza, R. A.; Clemens, O. Kinetic Study of the Interdiffusion of Fluorine and Oxygen in the Perovskite-Type Barium Ferrate System $BaFeO_{2.5-}F_2$. *J. Phys. Chem. C* **2021**, *125*, 2287–2298.

(40) Cai, Z.-X. Dislocation-Assisted-Diffusion Model for the Kinetics of Bismuth Cuprate 2212-to-2223 Transformation. *IEEE Transactions on Applied Superconductivity* **1999**, *9*, 2714–2717.

(41) Weinstock, B.; Weaver, E. E.; Knop, C. P. The Xenon-Fluorine System. *Inorg. Chem.* **1966**, *5*, 2189–2203.

(42) Holt, J. R., -. The Interaction of Xenon Difluoride with Si(100). **2002**.

CHAPTER 4: Sc_2C – A 2D SEMICONDUCTING ELECTRIDE[a]

Lauren M. McRae[†], *Rebecca C. Radomsky*[†], *Jacob T. Pawlik*[†], *Daniel L. Druffel*[†], *Jack D. Sundberg*[†], *Matthew G. Lanetti*[†], *Carrie L. Donley*[‡], *Kelly L. White*[†], and *Scott C. Warren*[*,†]

†Department of Chemistry, University of North Carolina at Chapel Hill, Chapel Hill, North Carolina 27599, United States

‡Chapel Hill Analytical and Nanofabrication Laboratory (CHANL), University of North Carolina at Chapel Hill, Chapel Hill, North Carolina 27599, United States

4.1 Introduction

Challenges in energy storage, electronics, and catalysis motivate the search for exotic materials with extreme properties, and electrides—crystals with bare electrons trapped at stoichiometric concentrations[1–3]—offer some of the most exceptional. These electrons have been ejected from atomic orbitals to reside in vacant lattice sites and, because they are so weakly bound, are better electron donors than alkali metals[4–6], can offer electrical conductivity that rivals silver[6], and can catalyze challenging reactions[6]. These properties have led to the exploration of electrides in applications where electron-rich materials are needed: N_2 and CO_2 reduction[7,8], electride's properties based on its structure or composition are underdeveloped. For example, unlike in conventional materials, it is not known how to tune the band gap of

[a]Portions of this chapter reproduced with permission from McRae, L. M.; Radomsky, R. C.; Pawlik, J. T.; Druffel, D. L.; Sundberg, J. D.; Lanetti, M. G.; Donley C. L.; White, K. L.; Warren, S. C. Sc2C: a 2D Semiconducting Electride. *Journal of the American Chemical Society* **2022**, 144 (24), 10862-10869. Copyright 2022 American Chemical Society.

electrides. And, even more critically, simple rules that could predict whether a material is an electride remain imprecise[3,14].

Presently, just two rules for predicting electrides are widely accepted: (1) the metal atoms that form the coordination sphere around the electride electron must be electropositive[15], and (2) the compound must be electron rich[16]. For example, in $[Ca_2N]^+(e^-)$[17], calcium is electropositive, and the compound is electron rich because the preferred oxidation states (Ca^{2+}, N^{3-}) and stoichiometry provide an extra electron, forming an electride. These rules are far too broad, however, because many compounds fulfill these rules but are not electrides.

To improve these rules, experiments have begun to identify the metals that can be adjacent to an electride electron. So far, only Ca[5], Sr[18,19], Ba[20], Y[21,22], Hf[23], and Gd[24,25] have been incorporated next to the electride site, while Sc and several of the lanthanide series have been computationally identified as candidates[26–28]. This delicate balance between electron counting and electronegativity was recently explored in the case of Ca_5Pb_3 (not an electride) and $Ca_3Hf_2Pb_3$ (an electride), as replacing calcium for hafnium makes the compound electron rich[16]. Despite these findings, the limit of cation electronegativity in the formation of electrides is not yet known. Therefore, to develop improved design rules for electrides and for their structure-property relationships, we explore the Sc_2C predicted electride[26] in comparison to the known Y_2C electride[22].

The question of nearest-neighbor electronegativity is essential because two experimentally observed electrides— Y_2C and Hf_2S—are “hybrid” electrides[3], where the electride electron has some overlap with the adjacent metal orbitals, and electronegativity of the metal may be correlated with the degree of hybridization. This covalency plays an important role in defining the electronic structure of the electride because the electride electron is normally found around the Fermi level. Thus, as hybridization occurs, tunable band

structures become possible, and indeed, Y_2C is a semi-metal. While there are examples of 0D electrides[28–31] and electride-like structures[32] with semiconducting character, this is unique among the 2D electrides[3,33]. This peculiarity raises the question of whether greater degrees of hybridization between metal and electride electron could lead to new categories of electride materials[34]. These questions motivate our exploration of the M_2C system, especially of layered Sc_2C.

To highlight uncertainties within the Sc_2C system, we briefly outline previous findings and predictions. Sc_2C was originally synthesized in 1967 and assigned to the NaCl structure type, which we refer to below as the cubic phase[35]. In 1969, different authors reassigned the structure as layered (R-3m) on the basis of its powder x-ray diffraction (PXRD) pattern[21,36], even though the pattern was missing several important reflections.

In 1989, the structure was again reassigned as the cubic phase[37] (Figure 4-1a, updated with our findings). This assignment appears to be correct and it is not known whether a layered Sc_2C electride exists. Currently, a 2D Sc_2C MXene structure has been explored computationally[38,39] and calculations predict that layered Sc_2C would be an electride[26]. In addition, 2D Sc_2C has been predicted to store an impressive 8% hydrogen by weight[40,41] and reversibly store fluoride as a battery anode at capacities that exceed state-of- the-art lithium-ion batteries[10]. Thus, if a layered Sc_2C electride does exist, it could allow these exciting predictions to be realized.

In this study, we predict that layered Sc_2C is stable using an evolutionary algorithm and experimentally explore the phase diagram around the desired composition. We then calculate the electronic structure of the synthesized material and compare it to Y_2C to understand periodic trends. We find that as the cation becomes more electronegative, the band gap opens with Y_2C as a semimetal and Sc_2C as a small band gap semiconductor. The synthesized layered Sc_2C is the first 2D electride with semiconducting properties, opening up

a fascinating new class of electride materials with several possible applications in energy storage or optoelectronics.

4.2 Phase Diagram Exploration

Although layered Sc_2C is unknown, we and Hirayama *et al.*[26] have hypothesized that it exists because Sc is chemically similar to Y and layered Y_2C is a stable phase. To investigate whether layered Sc_2C is thermodynamically stable, we used USPEX to explore the scandium-carbon phase space. The phase diagram we obtained indicates that the Sc_2C composition is on the hull, and that the layered $R\bar{3}m$ structure is stable by 28 meV/atom (Figure 4-1b). This modest relative stability could suggest why the layered phase had not previously been synthesized.

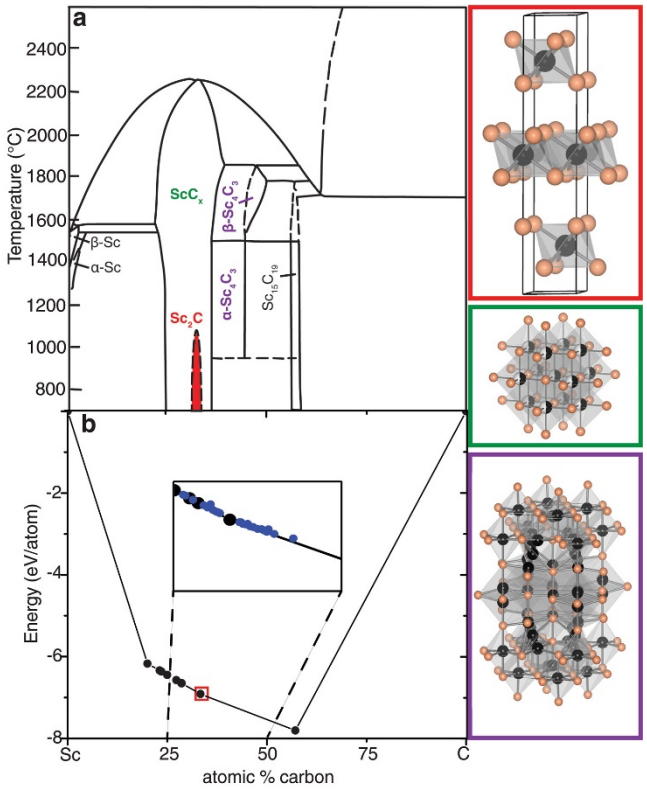


Figure 4-1. Phase exploration of the Sc-S system. (a) The binary phase diagram of the Sc-C system adapted from Velikanova et. al. The layered Sc_2C is shown in red. **(b)** The hull diagram for the Sc-C phase, as calculated with USPEX. The conventional unit cell for layered Sc_2C (red), cubic ScC_x (green), and α-Sc_4C_3 (purple) are shown.

The possibility that layered Sc_2C is thermodynamically stable motivated us to make this compound via high-temperature solid-state synthesis. In the Y_2C synthesis, we observed that high oxygen content in the yttrium led to formation of the cubic phase (YC_x). With this in mind, compared to the synthesis performed in Rassaerts et. al.'s 1967 study, we suspected that our use of high purity scandium with a lower oxygen content would allow us to experimentally realize our computational prediction. We arc-melted scandium and carbon in ratios from 2:0.9 to 2:1.15, respectively. These arc-melted samples had a high content of the cubic structure (ScC_x), but arc-melting has a rapid cool-down, so the structure may not be at equilibrium. Therefore, we followed arc-melting with annealing for 7 days at 1100°C to increase the likelihood of observing the thermodynamically favored layered phase. We found that the cubic structure is stable both at compositions with deficient carbon and excess carbon. However, at a composition of 2:0.99, the layered structure was observed, and this is reflected in the new binary phase diagram we propose for the Sc-C system (Figure 4-1a)[37]. There is uncertainty in the assignment of the temperature at which the congruent layered-to-cubic phase change occurs, but our experiments indicate that the layered phase is stable to at least 1100°C.

4.3 Structural Characterization

To fully understand the structure of the layered phase, we first performed PXRD experiments of the product at room temperature and refined the pattern using the Rietveld method[42] (Figure 4-2). The pattern indexed as the $R\bar{3}m$ structure with lattice parameters of a = b = 3.337 Å and c = 16.346 Å. This refinement includes the incorporation of preferred orientation at {104} with a March coefficient of 0.754. The sample contained up to 15% of the cubic ScC_x, which we attribute to a relatively low stability of the layered phase as well as possible oxygen contamination in the Sc reactant. To quantitatively compare the predicted and experimental structures, we further optimized the structure from USPEX using the PBEsol

functional. The calculated lattice parameters were 0.68% smaller in a and 0.09% smaller in c, which is within the typical error between PBEsol and experiment. This further confirms that the synthesized material is layered Sc_2C.

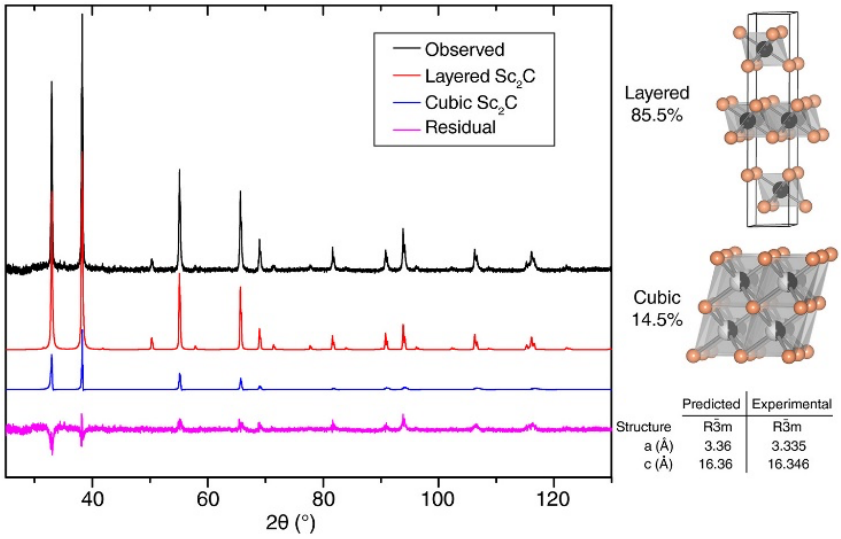


Figure 4-2. X-ray diffraction patterns of the experimental structure compared to the calculated layered and cubic Sc2C phases. The calculated amounts of the layered and cubic are shown as determined by the Rietveld method. The predicted and experimental lattice parameters are compared.

To better understand the effect of annealing in these samples, we obtained high-resolution transmission electron microscopy (HRTEM) of the product at room temperature under high vacuum. In Figure 4-3, we compare the Fast Fourier Transforms (FFTs) of these samples, where the non-annealed sample shows a ring pattern while the annealed sample shows well-defined spots. From the FFT images, we constructed filtered HRTEM images to create a color-coded map of crystalline domains where we compare the crystallinity of Sc_2C before and after annealing. The filtered HRTEM images and FFTs confirm that the domain size is small prior to annealing, likely due to kinetic trapping from rapid cooling after arc-melting. Even with annealing, there was still about 15% of the cubic phase present, which we attribute to a small amount of oxygen in the sample. In an attempt to leach any oxygen present

in the reaction container, we tried the synthesis in the presence of a titanium sponge. This did not improve the layered content of the sample. We, therefore, suspect that impurities in the product must come from impurities present in the Sc reactant[43].

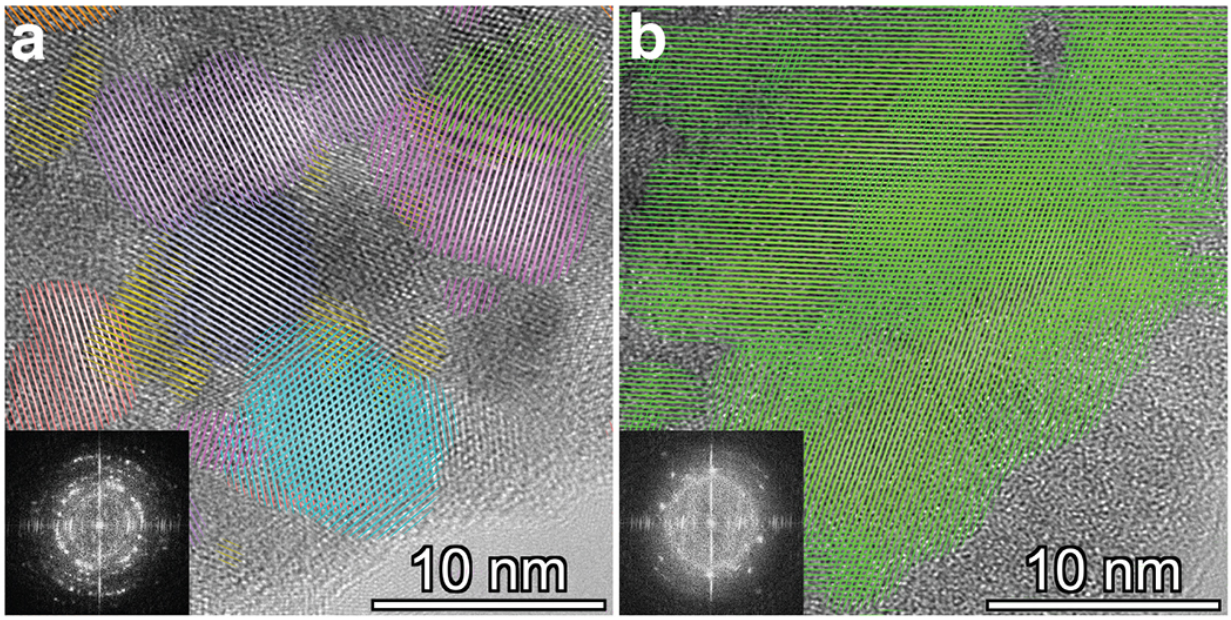


Figure 4-3. Filtered HRTEM images of Sc_2C particles. (a) A high-resolution TEM image of Sc_2C before annealing, with colored lattice planes corresponding to different crystallite regions determined through FFTs. **(b)** A high-resolution TEM image of Sc_2C after annealing for 7 days, with the lattice planes of the single crystallite region in green.

In addition, we used TEM to confirm that the layered Sc_2C phase is dominant after annealing. While refinement of the XRD pattern indicates that there is a small amount of cubic Sc_2C (14.5%) compared to layered Sc_2C (85.5%), the refinement has some uncertainty because the layered and cubic patterns are similar. In electron diffraction, the most common spatial frequency corresponds to a d-spacing of 2.3 Å, which we assign to either {104} in the layered structure or {101} in the cubic structure. This ambiguity motivated us to find distinct peaks for the layered phase. To identify the phase of these domains, we sought to acquire diffraction patterns containing the {117} reflection of the layered phase (50° 2θ in XRD pattern), which is expected at 5.501 nm^{-1}, for which there are no reflections in the cubic phase. In

Figure 4-4, we observe diffraction spots at 5.479 nm^{-1}, which can only be assigned to these planes in the layered phase. Simulations of the cubic structure with varied arrangements of carbon and carbon vacancies also failed to show a diffraction peak at 5.501 nm^{-1}. Importantly, the prevalence of {117} in diffraction patterns increases upon annealing, in agreement with XRD. In addition, XRD and TEM lattice spacings agree within 0.6%. This data confirms the experimental structure from XRD and corroborates the Rietveld refinement result.

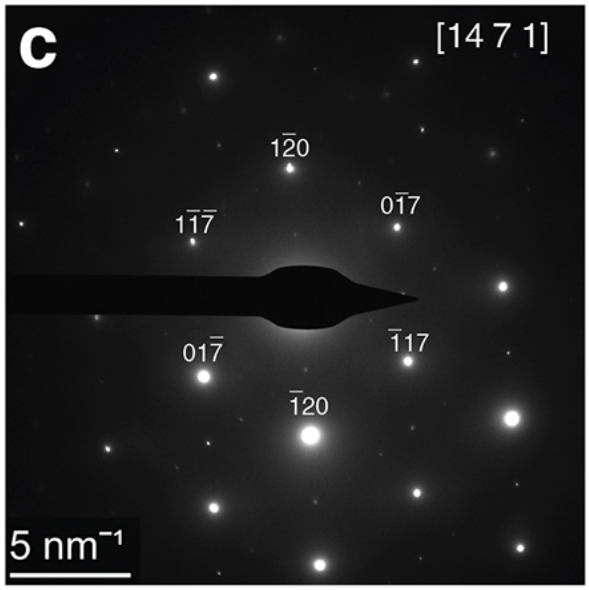


Figure 4-4. Electron diffraction pattern of annealed Sc_2C. This pattern, taken on the [14 7 1] zone axis, contains the {117} family of planes of layered Sc_2C, which is not present in the cubic phase.

4.4 Electronic Structure Characterization

Having confirmed the existence of layered Sc_2C as a thermodynamically stable material, we examined the material's electride character. In the experimental structure determined from our Rietveld refinement, there was a longer scandium-scandium distance (3.53 Å) than in scandium metal (3.22 Å) and Sc_2O_3 (3.27 Å). This increased distance could indicate that electride electrons are present, so we sought evidence by calculating the electron localization function (ELF) using the hybrid DFT functional HSE-06. The ELF

measures the degree of electron spatial localization compared to a reference electron with the same spin and provides a map of electron probability across a system. The ELF of Sc_2C shows localization of electrons that are not associated with either the scandium or carbon atoms and indicates that there is electride character in the layered structure (Figure 4-5a).

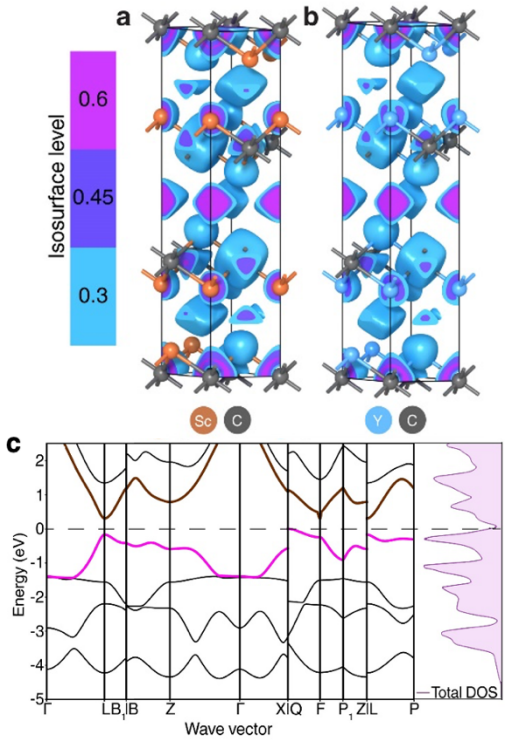


Figure 4-5. Electronic structure of Sc_2C. (a) The 3D ELF of Sc2C, where the gradient of isosurface level spans from 0.3-0.6. This scale is the same for each ELF. **(b)** The 3D ELF of Y2C. **(c)** The Sc2C band structure, total density of states (purple), and partial density of the electride states as a percentage of the total (blue). The valence and conduction bands are highlighted in red and green, respectively.

We calculated the band structure and density of states (DOS) with HSE-06 and found that Sc_2C is a semi-conductor with a 0.305 eV indirect band gap and a 0.476 eV direct band gap (Figure 4-5c). We attempted to further purify Sc_2C, but the cubic phase remained in all experiments. This prevented us from making electrical and optical band gap measurements on pure layered Sc_2C.

To understand how cation electronegativity plays a role in band structure, we compare these results to the electronic structure of Y_2C. The known hybrid electride Y_2C has a similar ELF to Sc_2C, where there is electron character that is not associated with either the yttrium or carbon atoms (Figure 4-5b). Yttrium has an electronegativity value of 1.22, whereas scandium has a value of 1.36[44]. Therefore, Sc_2C has the most electronegative metal adjacent to the electride site yet synthesized in a 2D electride. Although Y_2C is a semimetal, we find that Sc_2C is an indirect band gap semiconductors. In these systems, increasing cation electronegativity correlates with an increasing band gap.

From these observations, we propose a model in which increasing electronegativity of metal leads to increased hybridization. As electronegativity of the metal increases, unoccupied states lower in energy and become closer in energy to the occupied electride states. Because the metal and electride states are close in energy and can physically overlap, the states hybridize. The consequence of this hybridization is that the bonding states are stabilized and adopt some character of the metal orbitals while the anti-bonding states are destabilized and adopt some character of the electride orbitals. Thus, increasing metal electronegativity leads to increasing hybridization and a larger splitting between occupied and unoccupied states—i.e., the band gap increases.

4.5 Stability in Air

We tested the stability of this novel material in air because electrides are good reducing agents. Indeed, our calculations[45] of Sc_2C's work function—3.78 eV on the (0001) plane—suggested that it could be a good electron donor, although less so than Y_2C[22], which has a slightly smaller work function and is more electropositive.

To explore the material's reactivity, we performed PXRD experiments after letting micron-sized particles sit in air for varying intervals of time (Figure 4-6). The data shows that the material oxidizes slowly, with almost no change after sitting in air for one day. However,

after four days, we observe that diffraction peaks shift to higher angles with decreased intensity and increased width. These attributes indicate a decrease in crystallinity and the formation of an amorphous material, which is the dominant phase by the final timepoint. Thus, unlike Hf2S, Sc2C is not naturally self-passivating.

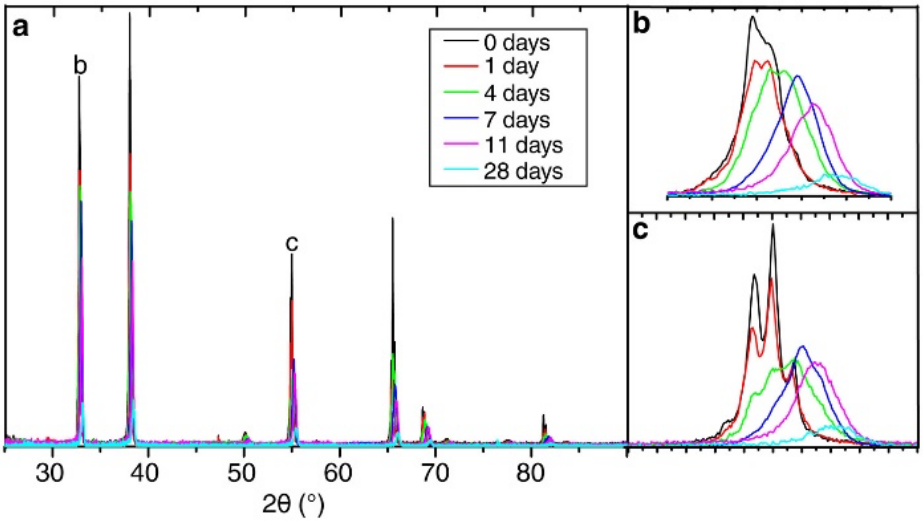


Figure 4-6. PXRD of Sc2C oxidation. (a) X-ray diffraction patterns after various amounts of oxidation. **(b)** The diffraction pattern zoomed in between 54-56° two-theta. **(c)** The diffraction pattern zoomed in between 32.4-33.4° two-theta.

4.6 Conclusions

We have synthesized a new 2D inorganic electride, Sc_2C, which is the first semiconducting 2D electride. The discovery of this phase within the disordered rocksalt region of the Sc-C phase diagram suggests, in general, that other new electrides might be found within the rocksalt regions of many binary phase diagrams. This has led to a new design rule for semiconducting 2D electrides: that more electronegative cations in 2D electrides lead to higher degrees of hybridization, resulting in greater splitting of valence and conduction bands. This first example of a semiconducting 2D electride suggests possible applications as a catalyst or photocatalyst, where the already-excellent electron-donating properties of the

electride could be further enhanced by photoexcitation. In the case of Sc_2C, its small band gap specifically allows applications as an IR photodetector. These and other applications—e.g., in hydrogen storage[40,41] or as a fluoride ion battery electrode[10]—can now be experimentally explored.

REFERENCES

(1) Matsuishi, S.; Toda, Y.; Miyakawa, M.; Hayashi, K.; Kamiya, T.; Hirano, M.; Tanaka, I.; Hosono, H. High-Density Electron Anions in a Nanoporous Single Crystal: [Ca24Al28O64]4+(4e-). *Science* **2003**, *301*, 626–629.

(2) Dye, J. L. Electrides: Early Examples of Quantum Confinement. *Acc. Chem. Res.* **2009**, *42*, 1564–1572.

(3) Hosono, H.; Kitano, M. Advances in Materials and Applications of Inorganic Electrides. *Chem. Rev.* **2021**, *121*, 3121–3185.

(4) Toda, Y.; Yanagi, H.; Ikenaga, E.; Kim, J. J.; Kobata, M.; Ueda, S.; Kamiya, T.; Hirano, M.; Kobayashi, K.; Hosono, H. Work Function of a Room-Temperature, Stable Electride [Ca24Al28O64]4+(e–)4. *Adv. Mater.* **2007**, *19*, 3564–3569.

(5) Gregory, D. H.; Bowman, A.; Baker, C. F.; Weston, D. P. Dicalcium Nitride, Ca2N—a 2D "Excess Electron" Compound; Synthetic Routes and Crystal Chemistry. *J. Mater. Chem* **2000**, *10*, 1635–1641.

(6) Zhang, X.; Yang, G. Recent Advances and Applications of Inorganic Electrides. *J. Phys. Chem. Lett.* **2020**, *11*, 3841–3852.

(7) Kuganathan, N.; Hosono, H.; Shluger, A. L.; Sushko, P. V. Enhanced N2 Dissociation on Ru-Loaded Inorganic Electride. *J. Am. Chem. Soc.* **2014**, *136*, 2216–2219.

(8) Qi, M.; Tang, C.; Zhou, Z.; Ma, F.; Mo, Y. Electride-Sponsored Radical-Controlled CO2 Reduction to Organic Acids: A Computational Design. *Chem. Eur. J* **2020**, *26*, 6234–6239.

(9) Hu, J.; Xu, B.; Yang, S. A.; Guan, S.; Ouyang, C.; Yao, Y. 2D Electrides as Promising Anode Materials for Na-Ion Batteries from First-Principles Study. *ACS Appl. Mater. Interfaces* **2015**, *7*, 24016–24022.

(10) Druffel, D. L.; Pawlik, J. T.; Sundberg, J. D.; McRae, L. M.; Lanetti, M. G.; Warren, S. C. First-Principles Prediction of Electrochemical Electron-Anion Exchange: Ion Insertion without Redox. *J. Phys. Chem. Lett.* **2020**, *11*, 9210–9214.

(11) Toda, Y.; Matsuishi, S.; Hayashi, K.; Ueda, K.; Kamiya, T.; Hirano, M.; Hosono, H. Field Emission of Electron Anions Clathrated in Subnanometer-Sized Cages in [Ca24Al28O64]4+(4e-). *Adv. Mater.* **2004**, *16*, 685–689.

(12) Hosono, H.; Hayashi, K.; Kamiya, T.; Atou, T.; Susaki, T. New Functionalities in Abundant Element Oxides: Ubiquitous Element Strategy. *Sci. Technol. Adv. Mater.* **2011**, *12*, 034303.

(13) Menamparambath, M. M.; Park, J.-H.; Yoo, H.-S.; Patole, S. P.; Yoo, J.-B.; Kim, S. W.; Baik, S. Large Work Function Difference Driven Electron Transfer from Electrides to Single-Walled Carbon Nanotubes. *Nanoscale* **2014**, *6*, 8844–8851.

(14) Dale, S. G.; Johnson, E. R. Theoretical Descriptors of Electrides. *J. Phys. Chem. A* **2018**, *122*, 9371–9391.

(15) Redko, M. Y.; Jackson, J. E.; Huang, R. H.; Dye, J. L. Design and Synthesis of a Thermally Stable Organic Electride. *J. Am. Chem. Soc.* **2005**, *127*, 12416–12422.

(16) Li, K.; Gong, Y.; Wang, J.; Hosono, H. Electron-Deficient-Type Electride Ca5Pb3: Extension of Electride Chemical Space. *J. Am. Chem. Soc.* **2021**, *143*, 8821–8828.

(17) Walsh, A.; Scanlon, D. O. Electron Excess in Alkaline Earth Sub-Nitrides: 2D Electron Gas or 3D Electride? *J. Mater. Chem. C* **2013**, *1*, 3525.

(18) Brese, N. E.; O'Keeffe, M. Synthesis, Crystal Structure, and Physical Properties of Sr2N. *J. Solid State Chem.* **1990**, *87*, 134–140.

(19) Chanhom, P.; Fritz, K. E.; Burton, L. A.; Kloppenburg, J.; Filinchuk, Y.; Senyshyn, A.; Wang, M.; Feng, Z.; Insin, N.; Suntivich, J.; Hautier, G. Sr3CrN3: A New Electride with a Partially Filled d-Shell Transition Metal. *J. Am. Chem. Soc.* **2019**, *141*, 10595–10598.

(20) Reckeweg, O.; DiSalvo, F. J. Crystal Structure of Dibarium Mononitride, Ba2N, an Alkaline Earth Metal Subnitride. *Zeitschrift für Kristallographie - New Crystal Structures* **2005**, *220*, 549–550.

(21) Atoji, M.; Kikuchi, M. Crystal Structures of Cubic and Trigonal Yttrium Hypocarbides; A Dimorphically Interphased Single-crystal Study. *J. Chem. Phys.* **1969**, *51*, 3863–3872.

(22) Zhang, X.; Xiao, Z.; Lei, H.; Toda, Y.; Matsuishi, S.; Kamiya, T.; Ueda, S.; Hosono, H. Two-Dimensional Transition-Metal Electride Y_2 C. *Chem. Mater.* **2014**, *26*, 6638–6643.

(23) Kang, S. H.; Bang, J.; Chung, K.; Nandadasa, C. N.; Han, G.; Lee, S.; Lee, K. H.; Lee, K.; Ma, Y.; Oh, S. H.; Kim, S.-G.; Kim, Y.-M.; Kim, S. W. Water- and Acid-Stable Self-Passivated Dihafnium Sulfide Electride and Its Persistent Electrocatalytic Reaction. *Sci. Adv.* **2020**, *6*, eaba7416.

(24) Mudryk, Y.; Paudyal, D.; Pecharsky, V. K.; Gschneidner, K. A. Magnetic Properties of Gd_2 C: Experiment and First Principles Calculations. *J. Appl. Phys.* **2011**, *109*, 07A924.

(25) Lee, S. Y.; Hwang, J.-Y.; Park, J.; Nandadasa, C. N.; Kim, Y.; Bang, J.; Lee, K.; Lee, K. H.; Zhang, Y.; Ma, Y.; Hosono, H.; Lee, Y. H.; Kim, S.-G.; Kim, S. W. Ferromagnetic Quasi-Atomic Electrons in Two-Dimensional Electride. *Nat. Commun.* **2020**, *11*, 1526.

(26) Hirayama, M.; Matsuishi, S.; Hosono, H.; Murakami, S. Electrides as a New Platform of Topological Materials. *Phys. Rev. X* **2018**, *8*, 031067.

(27) Inoshita, T.; Jeong, S.; Hamada, N.; Hosono, H. Exploration for Two-Dimensional Electrides via Database Screening and *Ab Initio* Calculation. *Phys. Rev. X* **2014**, *4*, 031023.

(28) Zhou, J.; Shen, L.; Yang, M.; Cheng, H.; Kong, W.; Feng, Y. P. Discovery of Hidden Classes of Layered Electrides by Extensive High-Throughput Material Screening. *Chem. Mater.* **2019**, *31*, 1860–1868.

(29) Ma, Y.; Eremets, M.; Oganov, A. R.; Xie, Y.; Trojan, I.; Medvedev, S.; Lyakhov, A. O.; Valle, M.; Prakapenka, V. Transparent Dense Sodium. *Nature* **2009**, *458*, 182–185.

(30) Dong, X.; Oganov, A. R.; Goncharov, A. F.; Stavrou, E.; Lobanov, S.; Saleh, G.; Qian, G.-R.; Zhu, Q.; Gatti, C.; Deringer, V. L.; Dronskowski, R.; Zhou, X.-F.; Prakapenka, V. B.; Konôpková, Z.; Popov, I. A.; Boldyrev, A. I.; Wang, H.-T. A Stable Compound of Helium and Sodium at High Pressure. *Nat. Chem.* **2017**, *9*, 440–445.

(31) Tang, H.; Wan, B.; Gao, B.; Muraba, Y.; Qin, Q.; Yan, B.; Chen, P.; Hu, Q.; Zhang, D.; Wu, L.; Wang, M.; Xiao, H.; Gou, H.; Gao, F.; Mao, H.-K.; Hosono, H. Metal-to-Semiconductor Transition and Electronic Dimensionality Reduction of Ca2N Electride under Pressure. *Adv Sci (Weinh)* **2018**, *5*, 1800666.

(32) Mizoguchi, H.; Okunaka, M.; Kitano, M.; Matsuishi, S.; Yokoyama, T.; Hosono, H. Hydride-Based Electride Material, LnH2 (Ln = La, Ce, or Y). *Inorg. Chem.* **2016**, *55*, 8833–8838.

(33) Liu, C.; Nikolaev, S. A.; Ren, W.; Burton, L. A. Electrides: A Review. *J. Mater. Chem. C* **2020**.

(34) Park, J.; Hwang, J.-Y.; Lee, K. H.; Kim, S.-G.; Lee, K.; Kim, S. W. Tuning the Spin-Alignment of Interstitial Electrons in Two-Dimensional Y2C Electride via Chemical Pressure. *J. Am. Chem. Soc.* **2017**, *139*, 17277–17280.

(35) Rassaerts, H.; Nowotny, H.; Vinek, G.; Benesovsky, F. Zum System Scandium—Kohlenstoff, 1. Mitt.: *Monatshefte für Chemie* **1967**, *98*, 460–468.

(36) Krikorian, N. H.; Bowman, A. L.; Krupka, M. C.; Arnold, G. P. The Preparation and Crystal Structureof Sc4C3. *High Temp Science* **1969**, *1*, 360–366.

(37) Velikanova, T. Ya.; Eremenko, V. N.; Artyukh, L. V.; Bondar, A. A.; Gordiichuk, O. V. Phase Diagrams of Sc-M(IV?VII)-C Systems. *Powder Metall. Met. Ceram.* **1989**, *28*, 711–718.

(38) Khazaei, M.; Arai, M.; Sasaki, T.; Chung, C.-Y.; Venkataramanan, N. S.; Estili, M.; Sakka, Y.; Kawazoe, Y. Novel Electronic and Magnetic Properties of Two-Dimensional Transition Metal Carbides and Nitrides. *Adv. Funct. Mater* **2013**, *23*, 2185–2192.

(39) Bae, S.; Espinosa-García, W.; Kang, Y.; Egawa, N.; Lee, J.; Kuwahata, K.; Khazaei, M.; Ohno, K.; Kim, Y.; Han, M. J.; Hosono, H.; Dalpian, G. M.; Raebiger, H. MXene Phase with C_3 Structure Unit: A Family of 2D Electrides. *Adv. Funct. Mater.* **2021**, *31*, 2100009.

(40) Hu, Q.; Sun, D.; Wu, Q.; Wang, H.; Wang, L.; Liu, B.; Zhou, A.; He, J. MXene: A New Family of Promising Hydrogen Storage Medium. *J. Phys. Chem. A* **2013**, *117*, 14253–14260.

(41) Hu, Q.; Wang, H.; Wu, Q.; Ye, X.; Zhou, A.; Sun, D.; Wang, L.; Liu, B.; He, J. Two-Dimensional Sc2C: A Reversible and High-Capacity Hydrogen Storage Material Predicted by First-Principles Calculations. *Int. J. Hydrogen Energy* **2014**, *39*, 10606–10612.

(42) Rietveld, H. M. The Rietveld Method. *Phys. Scr.* **2014**, *89*, 098002.

(43) Kononov, A.; Kuznetsov, S.; Polyakov, E. Electrorefining in Molten Salts — an Effective Method of High Purity Tantalum, Hafnium and Scandium Metal Production. *J Alloys Compd* **1995**, *218*, 173–176.

(44) Allred, A. L. Electronegativity Values from Thermochemical Data. *Journal of Inorganic and Nuclear Chemistry* **1961**, *17*, 215–221.

(45) Fall, C. J.; Binggeli, N.; Baldereschi, A. Deriving Accurate Work Functions from Thin-Slab Calculations. *J. Phys.: Condens. Matter* **1999**, *11*, 2689–2696.

CHAPTER 5: THE YTTRIUM SULFIDE ELECTRIDES

5.1 Introduction

Batteries with high capacities and fast charge times are imperative in the effort to advance renewable energy. Currently, lithium-ion batteries (LIBs) dominate the field of rechargeable energy storage due to their high efficiency and relatively large energy density. However, their short lifespans, limited charge capacities, and scarce resources have left a need for better batteries[1]. Anion shuttle batteries, where a negative ion (such as F^-) is shuttled from the cathode to the anode rather than a positive ion (such as Li^+), have been proposed as alternatives to LIBs due to their high predicted capacities[2–6]. However, fluoride-ion batteries (FIBs) remain relatively unexplored due to the lack of materials with sufficient F^- conductivity[7].

The concept of electron-anion exchange (EAX)[8] has proposed electrides—materials with bare electrons situated in vacant crystallographic lattice sites—as promising F^- intercalation materials due to the similar size and charge of the F^- ion and the electride electron. Y_2C, in particular, has been studied and experimentally demonstrated to reversibly intercalate F^- in an electrochemical system[9]. After electrochemical discharge, the layered Y_2C electride is converted into Y_2CF_2[10], with F^- ions occupying the layer previously occupied by bare electride electrons. F^- hopping events occur solely within this layer between octahedral and tetrahedral sites, which is sterically limited based on transition-state interactions between the diffusion F^- ion and nearest-neighbor Y atoms. Even so, the activation energy (E_a) for diffusion has been modeled to be 196 meV[8], almost a factor of two smaller than that for Li^+ diffusion in commercial LIB electrodes. Upon conversion from Y_2C to Y_2CF_2, the material also undergoes a stacking sequence shift from ABC-stacked Y_2C to AA-stacked Y_2CF_2. This shift also has an

associated activation energy, thus increasing the overall energy barrier to fully fluorinating Y_2C.

We have sought to discover electrides with improved sterics to further decrease the activation energy of fluorination and thus increase the ionic conductivity. To address the sterically hindered diffusion process, we have investigated Y-S phases, which have a much larger anion in the host lattice (S^{2-} ionic radius = 184 pm) than layered carbides (C^{2-} ionic radius = 135 pm). We predict that larger anions in the host lattice will lead to larger interlayer spaces for ionic diffusion, decreasing any steric hindrance to F^- hopping as a result.

The Y-S phase diagram has been largely unexplored thus far, with only three known binary phases, YS[11,12], Y_5S_7[13], and Y_2S_3[14]. As written, none of these phases are anion deficient, so these phases would not appear to be electrides. However, the YS phase has a typical NaCl-type rocksalt structure. Often, binary rocksalt phases have a large phase width, allowing for large concentrations of disordered anion or cation vacancies. For example, in the Y-C phase diagram[15] in Figure 5-1a, the YC_x rocksalt spans from 15% to 66% C. Similarly, in the Sc-S phase diagram[16] in Figure 5-1b, the S composition in the ScS_x rock salt region ranges from 41% to 55%. Although the Y-S phase diagram has not been explored, the similar chemistry of yttrium and scandium would likely indicate that the YS_x rocksalt phase will have a similar nonzero width.

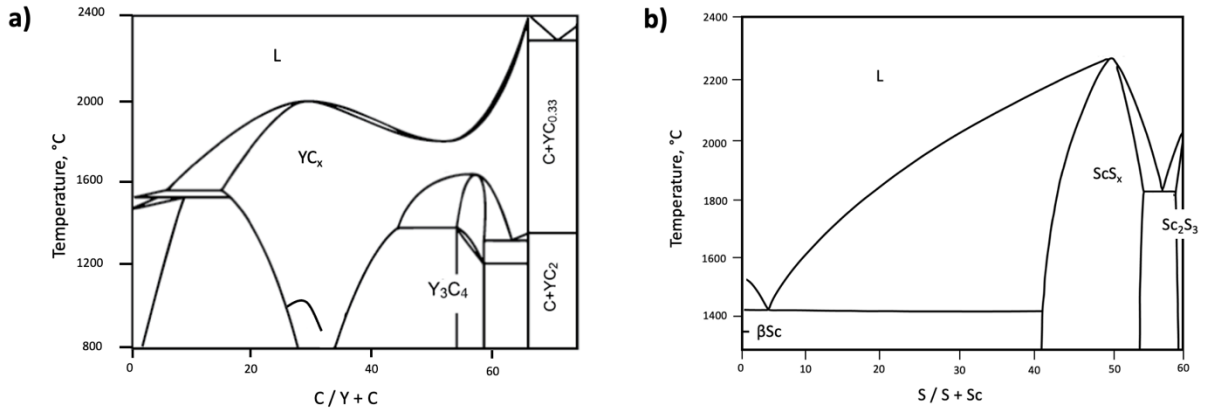


Figure 5-1. Y-C and Sc-S binary phase diagrams. (a)[15] The YC_x disordered rocksalt region shows a large phase width. The region within the YC_x phase at 33% C (below 1000 C) is the ordered (layered) Y_2C electride. **(b)**[16] The Sc-S phase diagram, while less explored, shows a similar disordered rock salt region.

Many rocksalt regions also contain rocksalt-derived phases created by ordered vacancies in the structure. These ordered structures are more thermodynamically stable than disordered rocksalt structures of the same stoichiometry at low temperatures and thus are present on phase and hull diagrams. For example, the Y_2C electride phase is an ordered Y-C rocksalt phase with 33% C, in which the C vacancies are entirely found in alternating planes. The layered phase is more stable than the disordered YC_x phase at temperatures below ~1000 ºC. The newly discovered Sc_2C electride phase[17], which was not known before a detailed investigation into the phase diagram via an evolutionary algorithm, similarly exists as an ordered phase within the disordered ScC_x rocksalt. We therefore hypothesize that anion-deficient Y-S electrides exist within the YS_x phase but have not yet been discovered.

In this study, we performed an evolutionary algorithm[18] search of the anion-deficient side of the Y-S phase diagram and discovered multiple stable phases. We confirm that these phases are indeed electrides via their electron localization functions[19] (ELFs). We then experimentally target these phases via arc melting and high-temperature solid-state synthesis. The resulting structural characterization provides insight into anion disorder in Y-S electrides.

We then perform molecular dynamics (MD) simulations to study the diffusion of F^- throughout the Y_6S_4 electride, testing our hypothesis that F^- diffusion barriers will be low due to large S^{2-} anions in the lattice.

5.2 Phase Diagram Exploration

To investigate new phases on the S-poor side of the Y-S phase diagram, we used USPEX[18] to perform a variable composition evolutionary algorithm search (Fig. 5-2a) of up to 30 atoms between 25% and 50% S composition, which is where we would expect rocksalt-derived structures to form. This search identified three previously unknown thermodynamically stable phases, Y_6S_4, Y_6S_5, and Y_8S_7. Each of these phases is more stable than a linear combination of Y and YS by 14 meV, 14 meV and 11 meV, respectively. Multiple other phases were also discovered within 5 meV (the maximum error associated with our calculations) of the hull and thus may also be stable. All of these phases are derivatives of the YS rocksalt phase with varying arrangements of S vacancies. There are no stable phases on the hull identified between Y_6S_4 and Y, indicating that a Y_2S structure similar to those of Y_2C and Sc_2C is not stable.

However, each phase that is stable or within 5 meV of the hull follows a vacancy scheme similar to that of layered electrides. In fully layered M_2X materials[20–24], anion sites are ordered into alternating layers of anions and electrons. The Y-S phases are similar but, because they do not have as high of a vacancy concentration, excess S anions are situated in the electron layer (Fig. 5-2b). The arrangement of the S anions depends on the Y:S stoichiometry, with Figure 5-2c showing a top-down view of the partially filled interlayer of Y_6S_4 and Y_6S_5 compared to the fully occupied YS rocksalt phase.

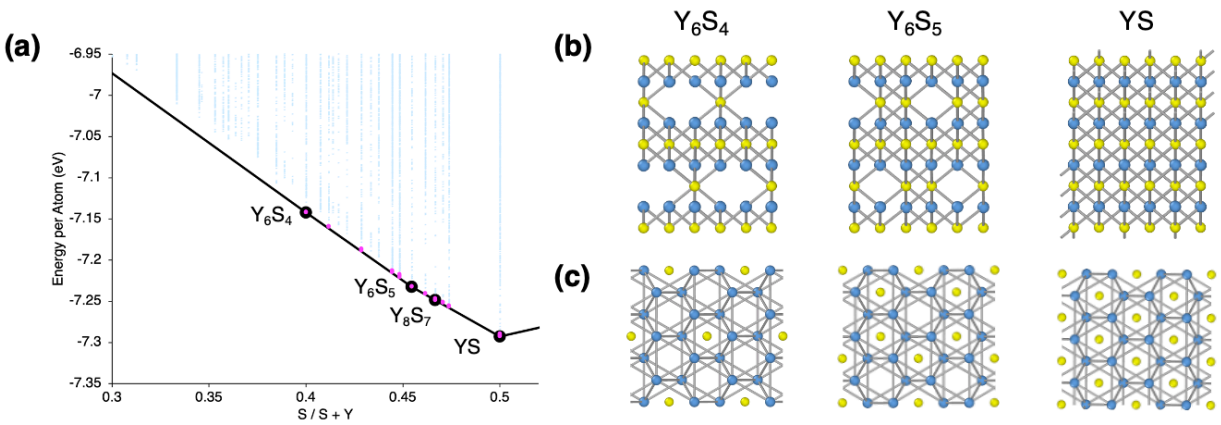


Figure 5-2. New Y-S phases discovered by an evolutionary algorithm. (a) The hull diagram for Y-S phases as determined via USPEX. Structures on the hull are represented by black dots, structures within 5 meV are represented by pink dots, and all other structures are represented by blue dots. **(b)** Side view of Y_6S_4, Y_6S_5, and YS. The blue atoms represent Y, and the yellow atoms represent S. **(c)** Top-down view of the partially filled anion layers in Y_6S_4 and Y_6S_5 and the corresponding filled layer in Y_6S_6.

Within the partially filled anion layers of Y_8S_7, Y_6S_5, and Y_6S_4, the S:vacancy ratios are 3:1, 2:1, and 1:2, respectively. In the Y_8S_7 phase, each vacancy is isolated from other vacancies. In Y_6S_5, the S atoms are arranged in a honeycomb pattern, with six S atoms surrounding one vacancy such that the vacancies are also isolated from each other. The Y_6S_4 structure shows the opposite occupancy as the Y_6S_5 structure, with one S atom surrounded by 6 vacancies in a honeycomb pattern. In fact, the Y_6S_4 structure is extremely similar to the layered electrides Y_2C and Sc_2C, with the sole difference being that 1/3 of the octahedral anion sites in the electride layer are filled with S^{2-} anions. We therefore refer to these S^{2-} anions as "pillars" between layers of the "Y_2S" host material and henceforth refer to Y_6S_4 as a pillared structure.

5.3 Electronic Structures

To assess whether these materials are electrides, we performed electron localization function (ELF) calculations on Y_6S_4 and Y_6S_5 as well as the fully occupied YS phase (Figure 5-3).

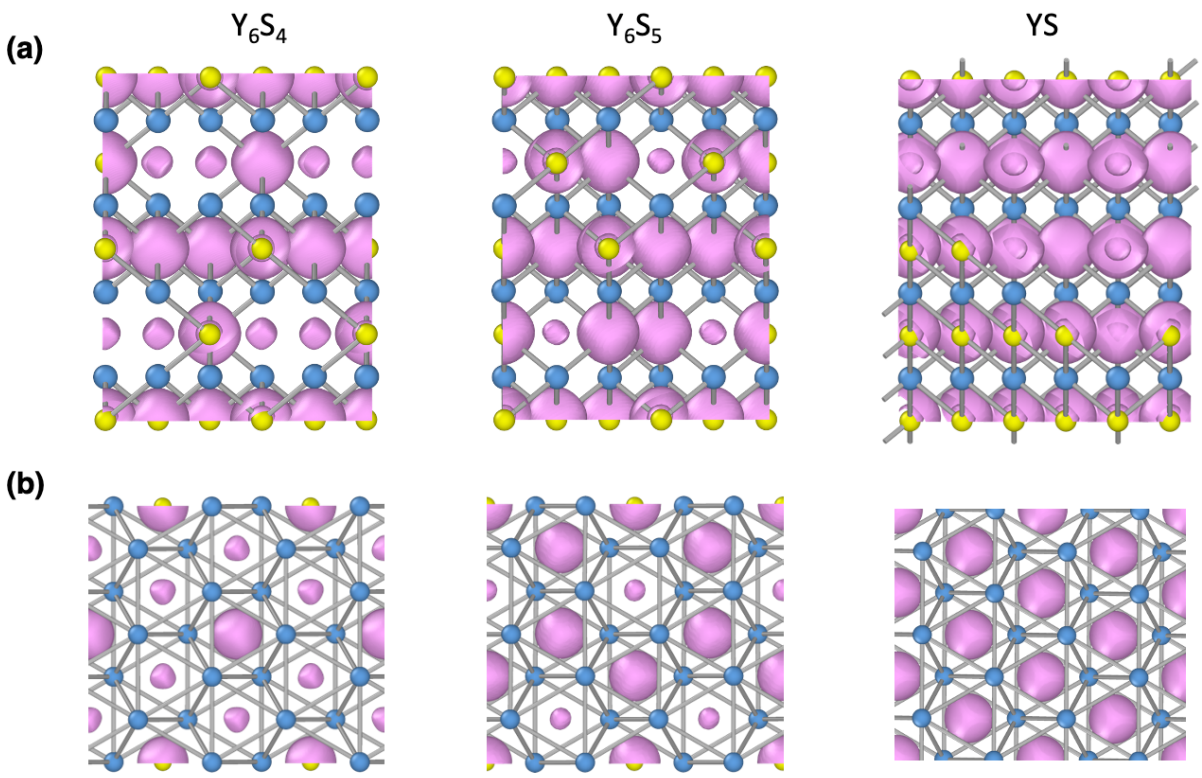


Figure 5-3. Electron Localization Functions of Y_6S_4, Y_6S_5, and YS. The blue atoms represent Y, and the yellow atoms represent S. Pink represents the ELF with an isosurface value of 0.5. **(a)** Side view of each structure. **(b)** Top-down view of the partially filled anion layers in Y_6S_4 and Y_6S_5 and the fully filled anion layer in Y_6S_6.

Both Y_6S_4 and Y_6S_5 are considered electrides, with electron density localized in the vacant octahedral anion sites. Because the electride sites in Y_6S_5 are isolated, it is considered a zero-dimensional (0D) electride. However, the electron density in Y_6S_4 is connected in a two-dimensional (2D) honeycomb pattern when viewed at a lower isosurface level, and is thus considered a 2D electride (Figure 5-4). We used the BadELF algorithm[25] to quantify the amount of electron density localized within a single octahedral electride site in Y_6S_4 to be 1.7 e^-. As there are two of these sites per formula unit, the Y_6S_4 electride can be formally written as $[Y_6S_4]^{3.4+}(e^{1.7-})_2$.

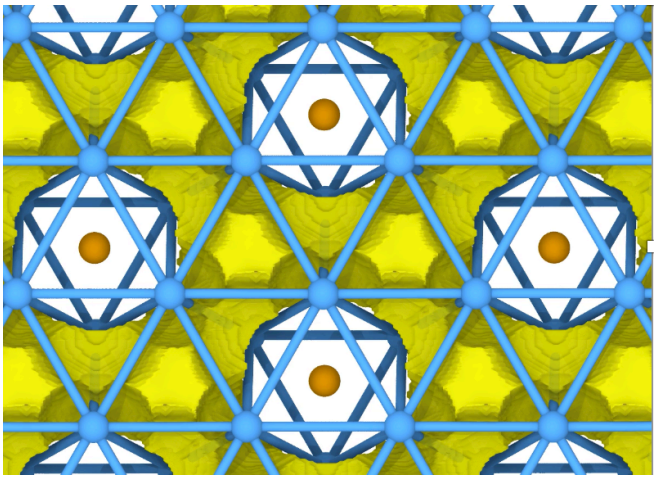


Figure 5-4. Connectivity of electron density in the Y_6S_4 electride. In this top-down view of the partially occupied anion layer of the Y_6S_4 electride, S atoms (orange) occupy octahedral sites within the framework of Y atoms (blue). Electride electron density (yellow) fills the other octahedral sites, connecting through tetrahedral sites to form a 2D network.

5.4 Structural Characterization

The identification of these phases as electrides motivated us to synthesize the Y_6S_4 and Y_6S_5 electrides and the YS rocksalt phase via high-temperature solid-state synthesis. We first arc-melted stoichiometric ratios of Y metal and Y_2S_3. Because the Y_6S_4 and Y_6S_5 structures are each more stable than a linear combination of Y and YS by 14 meV, we then annealed the resulting materials for 7 days at 1100 ^oC with a linear cool-down over 48 hours to target the thermodynamically stable phases.

We performed PXRD measurements on each material to investigate their structures and compare them to our predicted structures via Rietveld refinement[26], as shown in Figure 5-5. As predicted by DFT, the experimental patterns show that as the stoichiometric amount of S decreases, the lattice slightly contracts. However the lattice parameters predicted via the PBEsol[27] functional are slightly smaller than the experimental parameters for each material.

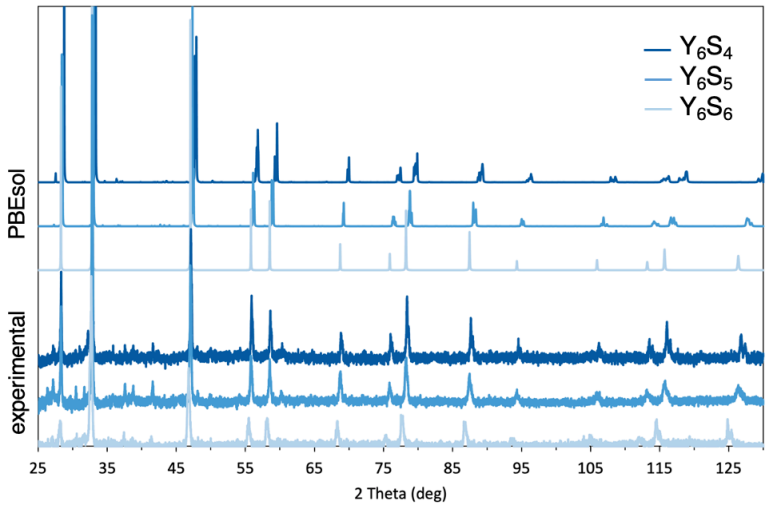


Figure 5-5. Experimental and predicted XRD patterns of the Y-S phases. This raw data, prior to Rietveld refinement, shows that the experimental lattice parameters follow the predicted trend in which lattice parameters increase with S content.

As the Y_6S_4 phase is a 2D electride, we hypothesize that it has a 2D percolation pathway which could be exploited for F^- diffusion and storage. We therefore chose to focus on this structure for more detailed characterization. There is some debate within the community on which DFT functional best predicts the structure of crystalline materials, and we have thus performed geometry relaxations on Y_6S_4 with the PBE[28], PBEsol[27], and HSE06[29] functionals, as shown in Figure 5-6. Although the PBEsol functional is typically chosen for structural characterization, we have chosen to refine our patterns to the HSE functional for two reasons. First, a report[30] by Lucero, Henderson, and Scuseria shows that the mean squared errors (MSEs) for the HSE and PBEsol functionals on rocksalt structures are similar: 0.38 Å and 0.33 Å, respectively. Additionally, we compared our predicted patterns to the experimental parameters of YS, a previously known structure, and chose the HSE functional because its predicted structure gives a diffraction pattern that most closely resembles experiment. Table 5-1 shows the lattice parameters for Y_6S_4 calculated via each functional.

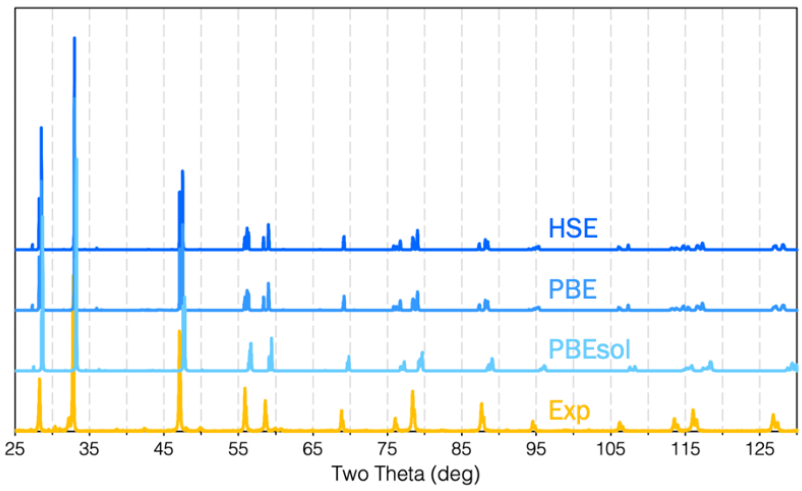


Figure 5-6. XRD patterns predicted by different functionals. Comparison of experimental XRD pattern of Y_6S_4 to those relaxed with HSE, PBE, and PBEsol functionals.

Table 5-1. Y_6S_4 experimental lattice parameters compared to various DFT functionals.

	HSE	PBE	PBEsol	Experiment
a (Å)	6.626	6.624	6.584	6.671
b (Å)	6.625	6.625	6.584	6.668
c (Å)	6.670	6.697	6.626	6.678
Vol (Å^3)	240.16	240.13	234.57	242.85

An in-depth refinement of the Y_6S_4 experimental structure revealed impurities corresponding to Y_2SO_2[31]. This phase is isostructural to Y_2CF_2, with layers of S and O anions alternating with layers of Y cations (Figure B-1). Because this phase is thermodynamically stable, any O in the starting materials, arc-melting chamber, or annealing process will cause Y_2SO_2 to form. The amount of Y_2SO_2 varied between 3 wt.% and 10 wt.% by Rietveld refinement. Because the Y:S ratio in Y_2SO_2 is greater than that in the target Y_6S_4, the formation and phase separation of Y_2SO_2 leaves the remaining Y-S phase slightly more S-rich than the targeted Y_6S_4 stoichiometry.

We therefore modified our synthetic strategy to account for this change in stoichiometry. To determine the correct starting stoichiometry for targeting the Y_6S_4 phase, we performed syntheses with initial Y:S ratios of 2:1, 6:3.5, and 6:4. Our evolutionary algorithm

studies predicted that the YS_x rocksalt window does not extend to S concentrations lower than 40%; therefore, we do not predict that the Y_2S or $Y_6S_{3.5}$ phase is stable. Because there are no stable phases that are more Y-rich than Y_6S_4, we expect these experiments to form a phase-separated combination of Y metal and Y_6S_4. Figure 5-7a shows that annealing all of the samples increased the size of the domains and that the domains in the Y_2S sample were smaller than those in the $Y_6S_{3.5}$ and Y_6S_4 samples. Before annealing, we expected some elemental Y to still be present in the sample because of the short melting times and fast cooling times of the arc-melter. This was indeed observed by PXRD but, after annealing, the amount of elemental Y significantly decreased in both the $Y_6S_{3.5}$ and Y_6S_4 samples (Fig. 5-7b). Rietveld refinement of each sample showed that before annealing, samples with more initial S had larger lattice parameters than those predicted by HSE06 (Fig. 5-7c). After annealing, however, the unit cell parameters of the Y_2S sample significantly increased, while those of the $Y_6S_{3.5}$ sample only slightly increased, and those of the Y_6S_4 sample slightly decreased. These studies led us to choose the initial reagent stoichiometry of $Y_6S_{3.5}$ to target the Y_6S_4 phase due to its large domains, small amount of elemental Y, and lattice parameters that most closely match those predicted by HSE06. All further analyses were carried out on samples produced from this ratio of starting materials.

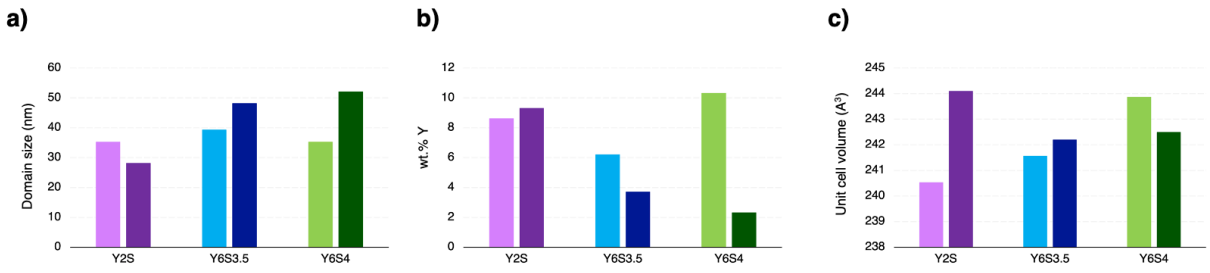


Figure 5-7. XRD studies of varying Y:S reagent stoichiometries. All bars show the unannealed sample on the left (lighter) and the annealed sample on the right (darker) of materials with reagent stoichiometries of Y_2S (purple), $Y_6S_{3.5}$ (blue) and Y_6S_4 (green). **(a)** The Scherrer equation was used to determine the domain sizes of each sample. **(b)** Rietveld refinement was used to determine the wt.% of crystalline elemental Y in each sample. **(c)**

Rietveld refinement from the HSE06-predicted phase was used to determine the lattice parameters of each sample.

These XRD studied confirm that we synthesized a anion-deficient YS_x rocksalt phase, but there remains some ambiguity regarding the arrangement of S atoms within the lattice. The predicted XRD patterns of Y_6S_4, Y_6S_5, and YS—all rocksalts with different concentrations and arrangements of S—are highly similar, with only slight differences in lattice constants and peak intensities (Fig. 5-5, top). Therefore, we cannot yet conclude whether our experimental structure has the same S:vacancy ordering as our predicted Y_6S_4 electride. We therefore sought to perform more detailed structural investigations via both Rietveld refinement and transmission electron microscopy (TEM).

We performed a more in-depth Rietveld refinement on our experimental Y_6S_4 structure and compared it to multiple calculated structures. We first refined our pattern to the predicted Y_6S_4 electride structure allowing lattice parameters and S occupancies to refine. Each S site occupancy remained close to 1, which is expected due to the absence of more S-deficient rocksalt phases. with no changes in occupancy (Figure 5-8a). Although the refined pattern matched the experimental pattern well, there was some disagreement in the intensities of the first two major peaks at 28.3º and 32.9º 2θ, as seen in the residual plot (green). There is also a small peak at 32.5º 2θ that corresponds to elemental Y and is not included in this refinement. The first peak at 28.3º 2θ corresponds to the 002 family of planes within the Y_6S_4 structure, as shown in Figure 5-8b. These planes are parallel to the partially filled S interlayer, and thus an increased S occupancy in this layer would decrease the experimental intensity of this peak.

This mismatch in the 002 plane leads us to believe that the S arrangements in our calculated figure do not match our experimental figure. To study this further, we refined our experimental pattern to a YS_x rocksalt structure. We created this structure by inserting S atoms into each empty octahedral site, resulting in a one-to-one structure identical to that of

the known YS rocksalt phase. However, our created structure does not abide by the same symmetry operations as the rocksalt phase and thus has a stoichiometry of Y_6S_6 in one unit cell, allowing for occupancies to be refined to most closely match any experimental phase. This structure was able to more accurately refine the experimental pattern (Fig. 5-8c), with a R_{wp} of 3.03%. The newly refined occupancies of each of the six S sites (Fig. 5-8d) are listed in Table 5-2.

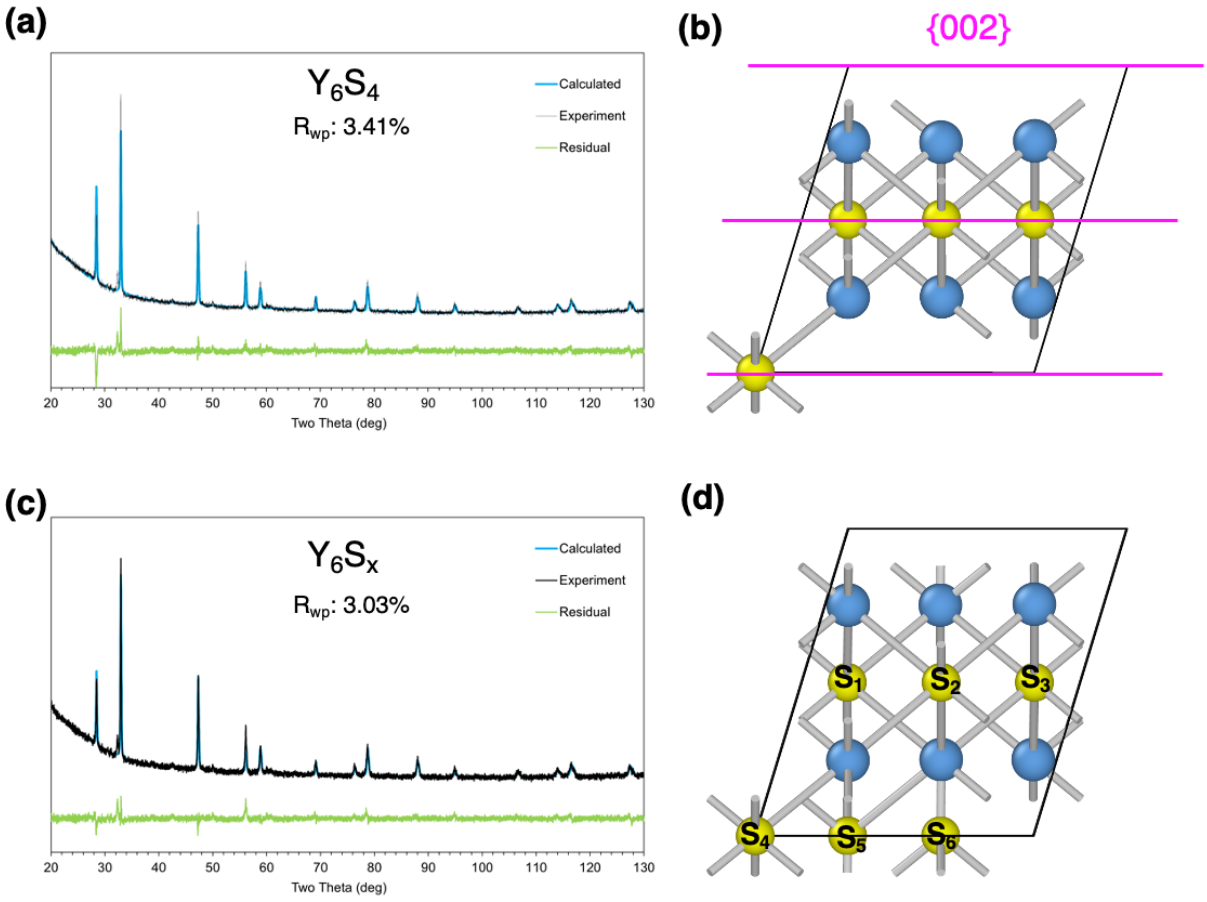


Figure 5-8. Rietveld refinement of the ordered and disordered structures of experimental Y_6S_4. (a) Rietveld refinement of the experimental structure to the ordered Y_6S_4 structure. **(b)** Unit cell of the ordered Y_6S_4 structure with the 002 family of planes highlighted in pink. **(c)** Rietveld refinement of the experimental structure to the Y_6S_x structure where S site occupancies were allowed to refine. **(d)** The Y_6S_x structure with each S site labeled.

Table 5-2. Refined occupancy of each S site in Y_6S_6. Sites correspond to those in Figure 5-8d.

Site	Occupancy
S_1	0.980
S_2	0.980
S_3	0.980
S_4	0.886
S_5	0.888
S_6	0.890

These occupancies suggest that multiple aspects of our experimental structure remain ambiguous. If this structure was refined exactly to the Y_6S_4 structure, four sites would be fully occupied, and two would be fully vacant. Instead, these data suggest that the S sites are either more disordered or ordered differently than originally predicted. Three S sites within the same layer, S_1, S_2, and S_3, remain almost fully occupied after refinement, suggesting that S sites and vacancies are ordered in layers along the z axis, as predicted. Within the layer where S vacancies exist, the occupancies of each site are almost identical, at 0.886, 0.888, and 0.890. This suggests that we not only have more S within this layer than originally predicted but also that the vacancies are disordered within these three sites. However, we note that the R_{wp} of each refinement are relatively similar and larger than expected for a perfectly matched pattern. There therefore remains some uncertainty in the arrangement of S atoms.

The S occupancies obtained via Rietveld refinement suggest an experimental stoichiometry of $Y_6S_{5.6}$. We thus performed energy dispersive X-ray spectroscopy (EDS) within the TEM to quantify the atomic ratio of Y to S to determine whether it more closely matched that of Y_6S_4 (1 : 0.66) or that of $Y_6S_{5.6}$ (1 : 0.933). After performing EDS on 6 thin particles (Figure B-2), we determined the Y:S ratio to be 1 : 0.78±0.10. This ratio falls between those of the predicted Y_6S_4 and refined $Y_6S_{5.6}$ and thus does not confirm either structure.

This in-depth investigation of the experimental YS_x structure and vacancy concentration via Rietveld refinement and EDS has not clearly identified which model structure is most accurate. The best fit Rietveld refinement suggests that nearly all of the S vacancies exist within one S layer, as predicted by DFT. However, we note that refinements of structures with varying S arrangements produced refinements that were nearly as strong, indicating that the Y:S stoichiometry and arrangement will be difficult to determine by Rietveld refinement alone. The exact concentration of vacancies remains ambiguous, as the best fit Rietveld refinement predicts a Y:S composition of 1: 0.933 while EDX measures a Y:S composition of 1 : 0.78±0.10. Because of this ambiguity, we plan to perform more in-depth studies of the experimental structure by varying parameters such as the Y:S ratio and annealing time/temperature to more closely target the predicted structure.

5.5 Computational Fluorination

Although the structure of the experimental Y_6S_x phase remains unclear, we are interested in performing in-depth studies of fluorination on the ideal Y_6S_4 structure, as we have hypothesized that both the large interlayer space and S pillars in the Y_6S_4 electride structure will allow for decreased sterics in the diffusion of F^- throughout the structure compared to purely layered electrides such as Y_2C. We therefore sought to investigate the kinetics of fluoride diffusion via *ab initio* molecular dynamics (MD) simulations. We first predicted the ground state of the Y_6S_4F structure by relaxing and calculating the energy of an F^- occupying an octahedral site (Figure 5-9a) and a tetrahedral site (Figure 5-9b).

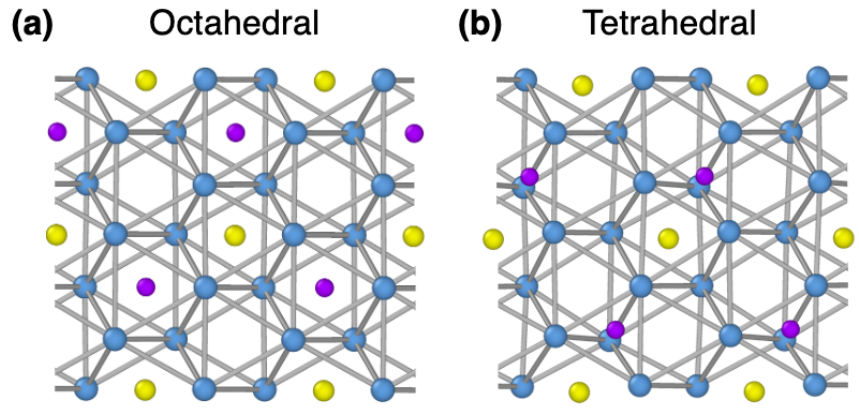


Figure 5-9. Y_6S_4F structure. (a) F^- (purple) is located in **(a)** an octahedral site or **(b)** a tetrahedral site within the partially occupied interlayer of the Y_6S_4 structure. Both structures were geometrically relaxed prior to energy calculations.

Both of these structures were dynamically stable (i.e., F^- did not move out of the starting octahedron/tetrahedron), indicating that both sites exist as a local energy minimum. However, we calculated that F^- is 17 meV/atom more stable in the tetrahedral site than in the octahedral site. We thus used this structure (Fig. 5-9b) as our starting structure for a series of MD simulations ranging from 300 K to 1200 K. Simulations were run for 10s of ns to observe multiple hopping events at each temperature. The diffusion coefficient *D* can be calculated for each MD simulation via the mean squared displacement (MSD) of fluoride over time[32]. Table 5-3 lists the diffusion constant and simulation time for each temperature.

Table 5-3. Diffusion constants of F^- through Y_6S_4.

T (K)	D (cm^2/s)	Simulation Time (ns)
300	4.245 x10^{-6}	52.8
310	5.679 x10^{-6}	29.9
320	5.144 x10^{-6}	22.9
330	2.142 x10^{-6}	43.5
340	2.086 x10^{-6}	82.1
350	3.638 x10^{-6}	46.9
367	1.255 x10^{-5}	7.04
383	3.032 x10^{-6}	40.3
400	8.367 x10^{-6}	25.0
450	3.792 x10^{-6}	23.9
500	7.911 x10^{-6}	23.7
550	1.101 x10^{-5}	21.4
600	1.324 x10^{-5}	22.9
650	4.232 x10^{-6}	47.8
700	8.540 x10^{-6}	41.2
750	1.593 x10^{-5}	44.9
800	1.623 x10^{-5}	42.2
850	1.362 x10^{-5}	45.0
900	1.236 x10^{-5}	33.5
950	1.499 x10^{-5}	24.9
1000	1.799 x10^{-5}	30.3
1050	1.352 x10^{-5}	25.1
1100	2.437 x10^{-5}	31.1
1150	3.864 x10^{-5}	31.3
1200	1.330 x10^{-5}	29.8

The Arrhenius equation is then used to calculate E_a for diffusion:

$$D = D_0 e^{-E_a/RT} \tag{5.1}$$

where D represents the diffusion coefficient at temperature T, D_0 represents the room-temperature diffusion coefficient, E_a is the activation energy, R is the ideal gas constant, and T is the temperature in K. Figure 5-10 shows the Arrhenius plot of F^- diffusion. We can then use the Einstein relation[33] to calculate the F^- mobility and ionic conductivity:

$$D = \mu K_B T \tag{5.2}$$

where μ is the mobility and K_B is the Boltzmann constant. Mobility can then be used to calculate ionic conductivity via the following relation:

$$\sigma = nq\mu \tag{5.3}$$

where σ is the ionic conductivity, n is the density of ions, and q is the charge of the ion.

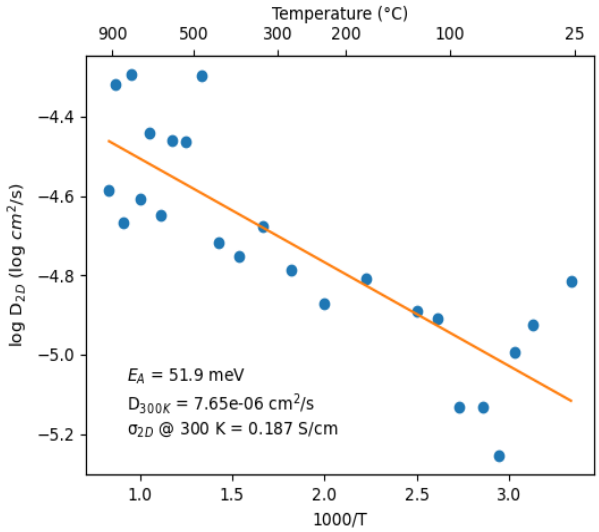


Figure 5-10. Arrhenius plot of F^- diffusion via MD. Each data point represents an *ab initio* MD simulation performed at a single temperature. D values were calculated via the MSD of F^-.

The E_a for F^- diffusion through Y_6S_4 was calculated to be 51.9 meV. It is important to note that the predicted activation energies and conductivities through a perfect crystal are often lower than the experimental values due to grain boundaries, impurities, and defects. Additionally, if a MD simulation begins with a structure that is not the most stable structure, the initial MSD will be artificially high, as ions are not yet in their ground state. Thus, we sought to confirm the ground state structure of Y_6S_4F. In an *ab initio* MD simulation, elevated temperatures can provide ions with enough energy to hop from one ground-state site to another. However, if the ions do not start in the ground state, their initial movement will be associated with finding the ground state site. In the case of our MD simulations, we often see that two F^- ions diffuse through the structure until they colocalize within one octahedral site

(Fig. 5-11), where they remain for a longer period of time. Over time, the F^- ions diffuse in and out of their co-located octahedron but often return to this position. We therefore suspected that this colocalized structure is the ground state structure of Y_6S_4F.

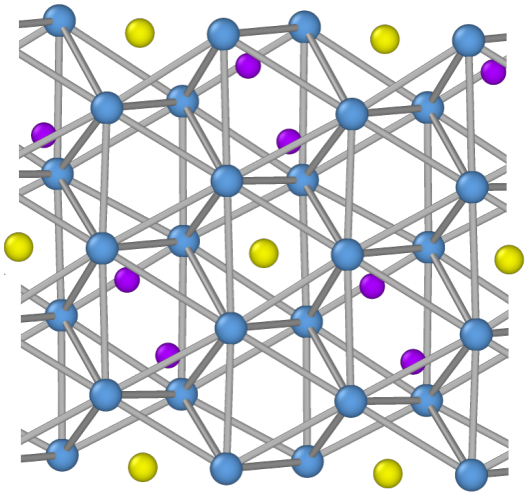


Figure 5-11. Predicted ground-state structure of Y_6S_4F. This structure was geometry relaxed prior to a single-point energy calculation but also frequently appeared throughout MD simulations.

We thus performed a structural relaxation and single-point energy calculation on a Y_6S_4F supercell with two F atoms within one octahedral site and determined that this structure is 36.4 meV/atom more stable than the tetrahedral structure used to start the MD simulations (Fig. 5-9b). We can therefore approximate the real activation energy to be 88.3 meV, which is the sum of the MD value and the difference between the initial structure and the ground state. This value is likely an over approximation, as F^- ions often find the ground state early in the MD simulations, and thus, their MSD from that point forward would be representative of the true E_a. We therefore expect the true E_a to be between 51.9 meV and 88.3 meV.

For comparison, the E_a for F^- diffusion through the Y_2C electride is ~196 meV[8], and Li^+ through commercial electrodes $LiCoO_2$[34] and graphite[35] are ~300 meV each. This difference is amplified exponentially, as E_a is exponentially related to diffusivity. Thus, conductivity is a better measure of differences in device performance. The ionic conductivity of F through Y_6S_4,

including the ground-state adjustment described above, is 150 mS/cm. For comparison, the best current FIB electrolyte, CsF in water, has an ionic conductivity of 152 mS/cm[36].

5.6 Conclusions

Although the Y-S phase space had previously been largely unexplored, we hypothesized that multiple ordered Y-S electride phases exist within a disordered YS_x rocksalt region but remained undiscovered. We explored this hypothesis via an evolutionary algorithm, where Y_6S_4, Y_6S_5, and Y_8S_7 structures, all derived from the YS rocksalt, were discovered to be on the hull and electrides. As Y_6S_4 is the most Y-rich of these materials, we experimentally targeted this phase via high-temperature solid-state synthesis and performed structural characterization. Rietveld refinement suggests that the interayer arrangements of S may be the same as predicted, with one full layer of S alternating with layers containing S vacancies. However, the intralayer concentration and arrangements of these vacancies remain ambiguous, and thus continuing this analysis, along with continuing investigations into ideal synthetic parameters, remains a compelling direction of research.

We also computationally investigated the fluorination of the predicted Y_6S_4 structure via MD. The E_a for fluoride diffusion was calculated to be between 51.9 meV and 88.3 meV, depending on the ground state structure, while the conductivity was calculated to be between 150 and 187 mS/cm. These values indicate extremely fast kinetics of F^- through Y_6S_4, suggesting that Y_6S_4 would be an ideal FIB electrode.

REFERENCES

(1) Tarascon, J.-M.; Dusastre, V.; Grätzel, M. Issues and Challenges Facing Rechargeable Lithium Batteries. In *Materials for Sustainable Energy: A Collection of Peer-Reviewed Research and Review Articles from Nature Publishing Group*; Co-Published with Macmillan Publishers Ltd, UK, 2010; pp. 171–179.

(2) Gschwind, F.; Euchner, H.; Rodriguez-Garcia, G. Chloride Ion Battery Review: Theoretical Calculations, State of the Art, Safety, Toxicity, and an Outlook towards Future Developments. *Eur. J. Inorg. Chem.* **2017**, *2017*, 2784–2799.

(3) Mohammad, I.; Witter, R.; Fichtner, M.; Anji Reddy, M. Room-Temperature, Rechargeable Solid-State Fluoride-Ion Batteries. *ACS Appl. Energy Mater.* **2018**, *1*, 4766–4775.

(4) Anji Reddy, M.; Fichtner, M. Batteries Based on Fluoride Shuttle. *J. Mater. Chem* **2011**, *21*, 17059.

(5) Xiao, A. W.; Galatolo, G.; Pasta, M. The Case for Fluoride-Ion Batteries. *Joule* **2021**.

(6) Nowroozi, M. A.; Mohammad, I.; Molaiyan, P.; Wissel, K.; Munnangi, A. R.; Clemens, O. Fluoride Ion Batteries – Past, Present, and Future. *J. Mater. Chem. A* **2021**.

(7) Sundberg, J. D.; Druffel, D. L.; McRae, L. M.; Lanetti, M. G.; Pawlik, J. T.; Warren, S. C. High-Throughput Discovery of Fluoride-Ion Conductors via a Decoupled, Dynamic, and Iterative (DDI) Framework. *npj Comput. Mater.* **2022**, *8*, 106.

(8) Druffel, D. L.; Pawlik, J. T.; Sundberg, J. D.; McRae, L. M.; Lanetti, M. G.; Warren, S. C. First-Principles Prediction of Electrochemical Electron-Anion Exchange: Ion Insertion without Redox. *J. Phys. Chem. Lett.* **2020**, *11*, 9210–9214.

(9) Tojigamori, T.; Matsui, N.; Suzuki, K.; Hirayama, M.; Abe, T.; Kanno, R. Fluorination/Defluorination Behavior of Y_2 C in Fluoride-Ion Battery Anodes. *ACS Appl. Energy Mater.* **2024**, *7*, 1100–1108.

(10) Druffel, D. L.; Lanetti, M. G.; Sundberg, J. D.; Pawlik, J. T.; Stark, M. S.; Donley, C. L.; McRae, L. M.; Scott, K. M.; Warren, S. C. Synthesis and Electronic Structure of a 3D Crystalline Stack of MXene-Like Sheets. *Chem. Mater.* **2019**, *31*, 9788–9796.

(11) Hulliger, F.; Hull, G. W. Superconductivity in Rocksalt-Type Compounds. *Solid State Commun.* **1970**, *8*, 1379–1382.

(12) Vaitheeswaran, G.; Kanchana, V.; Svane, A.; Christensen, N. E.; Olsen, J. S.; Jørgensen, J. E.; Gerward, L. High-Pressure Structural Study of Yttrium Monochalcogenides from Experiment and Theory. *Phys. Rev. B* **2011**, *83*, 184108.

(13) Adolphe, C. Contribution à l'étude d'un Groupe de Sulfures Isostructuraux de Terres Rares et d'yttrium de Type Y5S7 et FeY4S7. **1965**.

(14) Schleid, T. Crystal Structures of D-Y_2S_3 and Y_2OS_2. *European Journal of Solid State and Inorganic Chemistry* **1992**.

(15) Otani, S.; Hirata, K.; Adachi, Y.; Ohashi, N. Floating Zone Growth and Magnetic Properties of Y2C Two-Dimensional Electride. *J. Cryst. Growth* **2016**, *454*, 15–18.

(16) Moffatt, W. G. *The Handbook of Binary Phase Diagrams, Volume 4*; reprint.; Genium Publishing Corporation, 1976.

(17) McRae, L. M.; Radomsky, R. C.; Pawlik, J. T.; Druffel, D. L.; Sundberg, J. D.; Lanetti, M. G.; Donley, C. L.; White, K. L.; Warren, S. C. Sc2c, a 2D Semiconducting Electride. *J. Am. Chem. Soc.* **2022**, *144*, 10862–10869.

(18) Glass, C. W.; Oganov, A. R.; Hansen, N. USPEX—Evolutionary Crystal Structure Prediction. *Comput. Phys. Commun.* **2006**, *175*, 713–720.

(19) Savin, A.; Nesper, R.; Wengert, S.; Fässler, T. F. ELF: The Electron Localization Function. *Angew. Chem. Int. Ed* **1997**, *36*, 1808–1832.

(20) Zhang, X.; Xiao, Z.; Lei, H.; Toda, Y.; Matsuishi, S.; Kamiya, T.; Ueda, S.; Hosono, H. Two-Dimensional Transition-Metal Electride Y_2 C. *Chem. Mater.* **2014**, *26*, 6638–6643.

(21) Gregory, D. H.; Bowman, A.; Baker, C. F.; Weston, D. P. Dicalcium Nitride, Ca2N—a 2D “Excess Electron” Compound; Synthetic Routes and Crystal Chemistry. *J. Mater. Chem* **2000**, *10*, 1635–1641.

(22) Brese, N. E.; O’Keeffe, M. Synthesis, Crystal Structure, and Physical Properties of Sr2N. *J. Solid State Chem.* **1990**, *87*, 134–140.

(23) Mudryk, Y.; Paudyal, D.; Pecharsky, V. K.; Gschneidner, K. A. Magnetic Properties of Gd_2 C: Experiment and First Principles Calculations. *J. Appl. Phys.* **2011**, *109*, 07A924.

(24) Kang, S. H.; Bang, J.; Chung, K.; Nandadasa, C. N.; Han, G.; Lee, S.; Lee, K. H.; Lee, K.; Ma, Y.; Oh, S. H.; Kim, S.-G.; Kim, Y.-M.; Kim, S. W. Water- and Acid-Stable Self-Passivated Dihafnium Sulfide Electride and Its Persistent Electrocatalytic Reaction. *Sci. Adv.* **2020**, *6*, eaba7416.

(25) Weaver, S. M.; Sundberg, J. D.; Slamowitz, C. C.; Radomsky, R. C.; Lanetti, M. G.; McRae, L. M.; Warren, S. C. Counting Electrons in Electrides. *J. Am. Chem. Soc.* **2023**, *145*, 26472–26476.

(26) Rietveld, H. M. The Rietveld Method. *Phys. Scr.* **2014**, *89*, 098002.

(27) Perdew, J. P.; Ruzsinszky, A.; Csonka, G. I.; Vydrov, O. A.; Scuseria, G. E.; Constantin, L. A.; Zhou, X.; Burke, K. Restoring the Density-Gradient Expansion for Exchange in Solids and Surfaces. *Phys. Rev. Lett.* **2008**, *100*, 136406.

(28) Perdew, J. P.; Burke, K.; Ernzerhof, M. Generalized Gradient Approximation Made Simple. *Phys. Rev. Lett.* **1996**, *77*, 3865–3868.

(29) Krukau, A. V.; Vydrov, O. A.; Izmaylov, A. F.; Scuseria, G. E. Influence of the Exchange Screening Parameter on the Performance of Screened Hybrid Functionals. *J. Chem. Phys.* **2006**, *125*, 224106.

(30) Lucero, M. J.; Henderson, T. M.; Scuseria, G. E. Improved Semiconductor Lattice Parameters and Band Gaps from a Middle-Range Screened Hybrid Exchange Functional. *J. Phys. Condens. Matter* **2012**, *24*, 145504.

(31) Mikami, M.; Nakamura, S. Electronic Structure of Rare-Earth Sesquioxides and Oxysulfides. *J Alloys Compd* **2006**, *408–412*, 687–692.

(32) Ong, S. P.; Richards, W. D.; Jain, A.; Hautier, G.; Kocher, M.; Cholia, S.; Gunter, D.; Chevrier, V. L.; Persson, K. A.; Ceder, G. Python Materials Genomics (Pymatgen): A Robust, Open-Source Python Library for Materials Analysis. *Comp. Mater. Sci.* **2013**, *68*, 314–319.

(33) Einstein, A. Über Die von Der Molekularkinetischen Theorie Der Wärme Geforderte Bewegung von in Ruhenden Flüssigkeiten Suspendierten Teilchen. *Ann. Phys.* **1905**, *322*, 549–560.

(34) Nakamura, K.; Ohno, H.; Okamura, K.; Michihiro, Y.; Moriga, T.; Nakabayashi, I.; Kanashiro, T. 7Li NMR Study on Li+ Ionic Diffusion and Phase Transition in Li CoO2. *Solid State Ionics* **2006**, *177*, 821–826.

(35) Persson, K.; Sethuraman, V. A.; Hardwick, L. J.; Hinuma, Y.; Meng, Y. S.; van der Ven, A.; Srinivasan, V.; Kostecki, R.; Ceder, G. Lithium Diffusion in Graphitic Carbon. *J. Phys. Chem. Lett.* **2010**, *1*, 1176–1180.

(36) Alshangiti, O.; Galatolo, G.; Rees, G. J.; Guo, H.; Quirk, J. A.; Dawson, J. A.; Pasta, M. Solvent-in-Salt Electrolytes for Fluoride Ion Batteries. *ACS Energy Lett.* **2023**, *8*, 2668–2673.

CHAPTER 6: ABF_6 MATERIALS AS FIB ELECTROLYTES

6.1 Introduction

Currently, one of the largest emerging areas of battery research is the search for solid-state electrolytes. In ion-shuttle batteries, electrolytes must have (i) high ionic conductivity for ions to diffuse between electrodes and (ii) low electrical conductivity to avoid "shorting" the battery. These electrolytes are typically made of liquids[1], which are particularly conducive to both high ionic and low electrical conductivities. However, the liquid nature of these electrolytes also gives rise to many drawbacks. In particular, if an imperfect battery has thermal runaway, the increase in temperature can cause the electrolyte to become volatile and flammable. In contrast, solid-state batteries use a solid ionic conductor as the electrolyte and offer higher operating voltages, thermal stability, and safety.[2–5]

Much of the current battery research is focused on Li-ion batteries (LIBs) or alternate cation-shuttle batteries (Na, Mg, Zn, etc.)[6–8]. F-ion batteries (FIBs), which shuttle negatively charged F^- rather than positively charged cations, have gained recent attention due to their high theoretical capacity[9–11]. However, FIBs have not yet been fully realized due to the lack of known materials with sufficient F^- ion conductivity.

Recently, our lab has published the most rigorous high-throughput study of ionic conductors to date.[12] All known fluoride-containing crystals—approximately 10,000[13]—were considered, and predicted fluoride diffusion barriers were calculated. Then, additional filters were used to identify structures that could act as F-ion conductors in a variety of applications. Two particular materials, $ZnTiF_6$ and $MgTiF_6$, were identified as possible electrolyte materials for FIBs due to their large band gaps and low predicted fluoride diffusion barriers.

6.2 ABF_6 Compounds and Structures

Following the discovery of $ZnTiF_6$ and $MgTiF_6$ as F-ion conductors, I re-evaluated the ~10,000 fluoride structures to find other structures with the same symmetry and stoichiometry to analyze periodic trends across materials. I first simply filtered to find structures with the ABF_6 stoichiometry where A and B are metals. The majority of structures have space group 148, matching the structures of $ZnTiF_6$ and $MgTiF_6$ (Figure 6-1a). However, a subset of materials also have the space group 225 (Figure 6-1b). ABF_6 structures of both space groups contain corner-sharing octahedra with metal centers surrounded by 6 fluorides. The octahedral tilt angles of each symmetry differ, with materials of the 225 space group having all M_1-F-M_2 angles of exactly 180°. Structures with space group 148, however, have tilted octahedra, with M_1-F-M_2 angles of 144.73°.

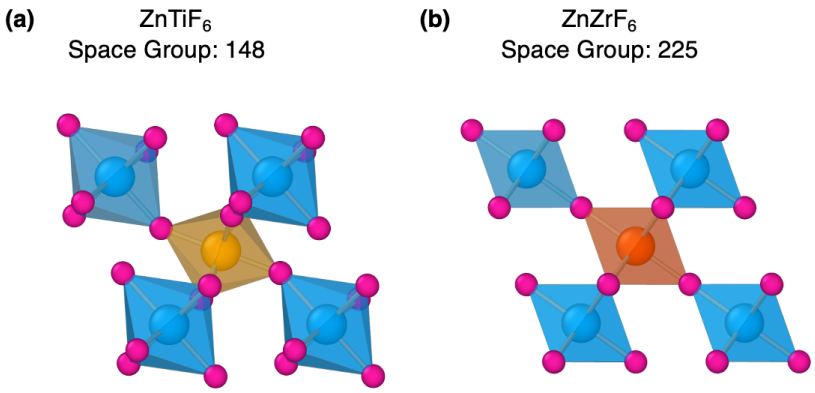


Figure 6-1. ABF_6 structures and space groups. (a) $ZnTiF_6$, an example structure with the 148 space group symmetry. The corner-sharing octahedra surrounding the metal atoms are tilted at 144.73°. Zn is blue, Ti is yellow and F is pink. **(b)** $ZnZrF_6$, an example structure with the 225 space group symmetry. The corner-sharing octahedra surrounding the metal atoms are exactly 180° from each other. Zn is blue, Zr is orange, and F is pink.

Sundberg *et al.*'s high-throughput study[12] included initial low-quality calculations of diffusion barriers via the IDPP method[14] with a single midpoint, which were scaled according to a subset of ~300 high-quality NEB[15] calculations. These calculations, often with errors <300 meV, are quite useful for filtering large sets of data and identifying promising candidates. From

this study[12], we determined the average diffusion barrier to be 0.84 eV ± 0.35 eV for the 73 ABF_6 materials with the 148 space group, and 1.67 eV ± 0.46 eV for the 21 materials with the 225 space group. We therefore elected to perform a more in-depth study of the materials with the 148 space group to analyze trends across structures with identical symmetry to find suitable candidates for FIB solid-state electrolytes.

I pulled all materials from the Materials Project[13,16] database that belong to space group 148, contained F, and had an anonymous formula of ABF_6. This search returned 115 candidate structures (Table C-1), all with the ABF_6 stoichiometry, where A and B are both metals. Seventy-three of these structures were previously analyzed by Sundberg *et al.*[12], while 42 are new to this study. Herein, we report calculations of the band gaps of each material calculated with the HSE06 functional to achieve accurate electronic structures, as well as F-ion diffusion studies via NEB for a subset of materials. We then chose $ZnSnF_6$ as the most ideal candidate material, performed more in-depth studies of diffusion via molecular dynamics, and synthesized it via mechanochemical ball milling.

6.3 Electronic Structure

Solid-state electrolytes in ion-shuttle batteries must be electrical insulators to prevent the battery from short-circuiting. Any structure available through the Materials Project database also includes a tabulated band gap calculated via the PBE[17] functional. However, it is well known, and even noted by the Materials Project, that electronic structures calculated via PBE vastly underestimate a material's band gap. We therefore calculated the band gap of each material via the HSE06[18] functional, which more accurately calculates electron delocalization due to the inclusion of the Hartree-Fock (HF) method. To perform these calculations, we used both the Simmate[16,19] workflows for "band structure calculation" and "density of states" and compared their estimations of the band gap. We also perform

analogous calculations on the same set of structures with the PBE functional for direct comparison. All values are listed in Table C-1.

We first sought to confirm that a full band structure calculation and a density of states (DOS) calculation give the same band gap for a material. These calculations were performed with the same mesh size k-point grid, but the band structure method also includes high-symmetry points in real space (as seen on the x-axis of a band structure plot). Figure 6-2a compares the PBE values of the band gap calculated via both methods, and Figure 6-2b shows these values for the HSE06 functional.

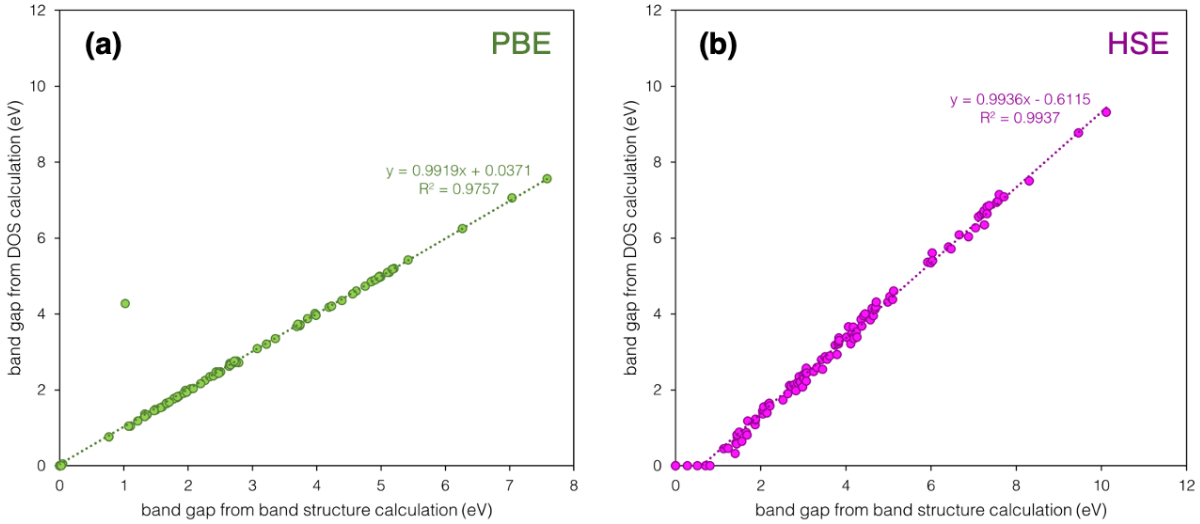


Figure 6-2. Band gaps calculated via band structure calculation vs. density of states calculation. Each calculation was performed via its respective workflows in Simmate with the same k-point mesh size. **(a)** band gaps calculated via the PBE functional. **(b)** band gaps calculated via the HSE functional.

Band gaps calculated via the PBE functional do not depend on the type of calculation, as there is a very close one-to-one correlation between the two. For those calculated via HSE, calculations via the two methods disagree only for materials with very low band gaps (<1 eV), where the density of states method often calculates a band gap of 0. This is demonstrated by the collection of data points along the x-axis of Figure 6-2b. The HSE-calculated band structure and DOS diagrams for one such material, $MgBiF_6$, are shown in Figure 6-3. There

is significant band splitting for spin-up and spin-down electrons evident in both calculations. The Fermi level for both calculations lies between a spin-up and spin-down electron from a Mg-Bi hybrid orbital. Upon analysis of the value at each K-point of the DOS calculation, incorrect broadening caused the calculated value to be 0. Therefore, for further analysis, we will use band gaps calculated via the band structure workflow.

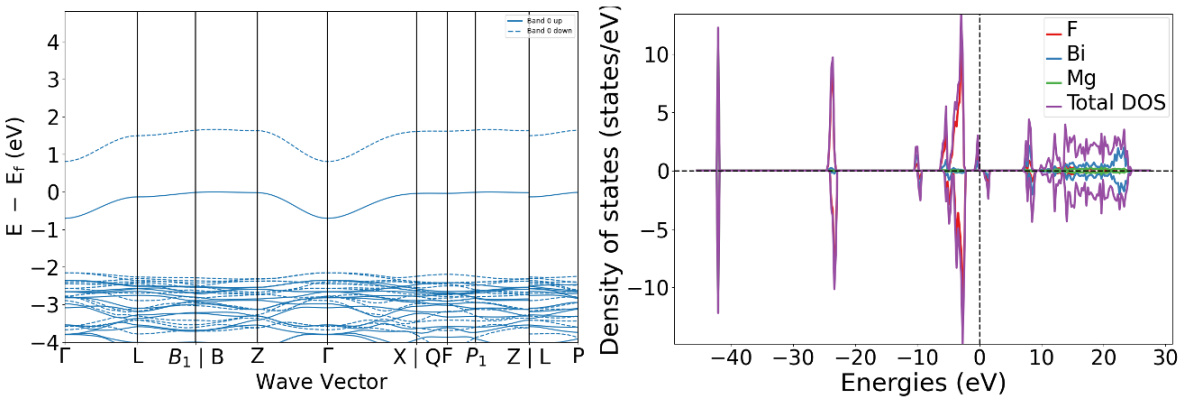


Figure 6-3. Band structure (left) and density of states (right) of $MgBiF_6$ calculated via HSE. Each calculation was performed via its respective workflows in Simmate with the same k-point mesh size. Spin up and spin down splitting in the DOS plot is denoted by the top and bottom plots.

We then compared the band gaps calculated by the band structure workflow with both the PBE and HSE06 functionals. The PBE method identified 37 of the materials as metals (band gap = 0), while the HSE method identified only 3. Figure 6-4 shows the relationship between the band gaps calculated via the HSE and PBE methods. From these calculations, we performed a linear regression on the data to be able to predict band gaps with only a low-quality PBE calculation, without the need to perform a cost-intensive HSE calculation. The regression, shown in Figure 6-4, fit these data to a linear model of:

$$\text{PBE} = 0.7784(\text{HSE}) - 0.7999. \quad (6.1)$$

The standard error of this regression is 0.861 eV. Because the HSE functional has been shown to calculate more accurate electronic structures, we used this as our dependent variable in these studies. However, for future calculations, this model can also be used to

calculate more accurate band gaps from only a low-quality PBE calculation without the need to perform a cost-intensive HSE calculation.

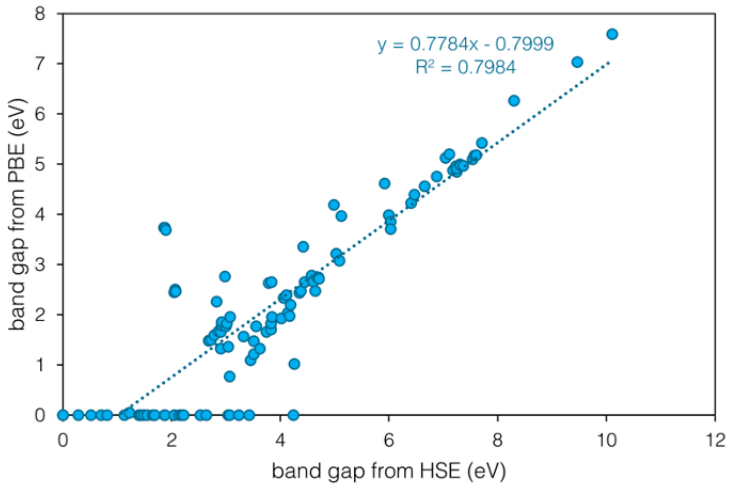


Figure 6-4. Band gaps calculated via HSE and PBE. Each calculation was performed via its respective workflows in Simmate with the same k-point mesh size.

We sought to understand the periodic trends of band gaps within the ABF_6 structures. We thus performed a "case study" by examining a subset of structures where A = Mg^{2+}. By keeping the A metal constant, we are able to make comparisons with only one variable: the identity of the B^{4+} metal. The structures used for this study are listed in Table 6-1, as well as their band gaps calculated via PBE and HSE. There are no discernable periodic trends in this set of structures when comparing band gap energy to atomic number or ionic radii of B^{4+} species. We therefore looked more in depth at the DOS plots of each of these structures (Figure C-1).

Table 6-1. Structures for in-depth band structure investigation. All band gaps are in eV.

Structure	HSE band gap	PBE band gap
$MgWF_6$	1.87	3.74
$MgMoF_6$	2.04	2.45
$MgRhF_6$	2.14	0.00
$MgCrF_6$	2.86	1.66
$MgNiF_6$	3.24	0.00
$MgCoF_6$	3.32	1.57
$MgPdF_6$	3.83	1.70
$MgMnF_6$	4.58	2.78
$MgPbF_6$	5.09	3.07
$MgTiF_6$	6.66	4.56
$MgSnF_6$	7.31	4.98

We wanted to investigate the contributions of each element present in the structure to the bands close to the Fermi level. We thus chose three example structures, two with transition metals, $MgTiF_6$ and $MgMoF_6$, and one p-block metal, $MgSnF_6$. Their DOS by elemental breakdown are shown in Figure 6-5. These calculations were performed by the "band structure" workflow (i.e., have been calculated with a spatial vector) but are plotted as DOS in order to more easily compare the bulk electronic structures. In each of these structures, the 2s and 2p orbitals of Mg are ~20 eV above the Fermi level, as Mg is in the 2^+ oxidation state and thus is isoelectronic to the noble gas Ne. The 2p orbitals of F can be seen just below the Fermi level, as F is in the 1^- state. The orbital energies of the B^{4+} metals vary with the identity of the metal. Ti^{4+} is isoelectronic to Ar and thus requires a considerable amount of energy to promote an electron to the unfilled 3d orbital. Similarly, Sn^{4+} has a completely filled 4d orbital and requires a considerable amount of energy to begin filling the 5s or 5p orbitals. As a result, both of these structures have very large band gaps. Mn^{4+}, on the other hand, has a half-filled d orbital, and that band therefore crosses the Fermi level, making the band gap 0 eV.

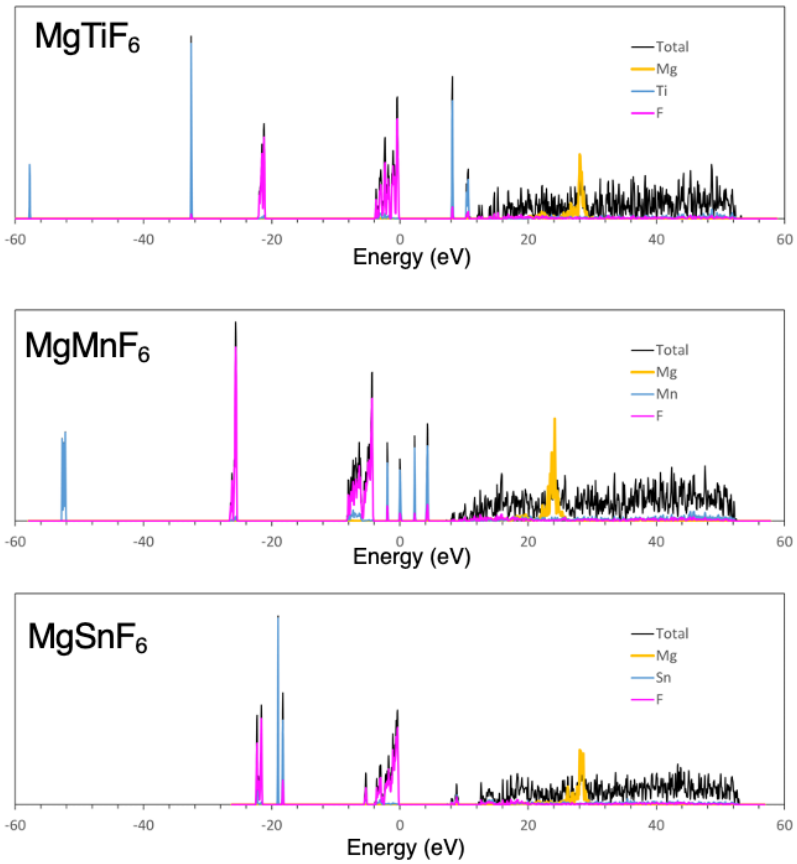


Figure 6-5. Densities of states of $MgTiF_6$, $MgMnF_6$, and $MgSnF_6$. Yellow represents orbitals belonging to Mg, pink represents F, and blue represents the respective B^{4+} metal. Calculations were performed on the full band structure but plotted as a DOS.

Often, solid-state electrolytes need a band gap above 3.5 eV to operate in a battery[5,12]. However, an even larger bandgap and lower electrical conductivity will allow for a more efficient battery. Our study of electronic structure shows that structures with p-block metals such as Sn often have large band gaps and thus would be good insulators for solid-state electrolytes.

6.4 Fluoride Diffusion

After correctly calculating the band gaps of all ABF_6 materials belonging to space group 148, we chose a subset of materials to perform in-depth analyses of fluoride diffusion. As Sn and Pb are p block metals, ABF_6 materials where B^{4+} = Sn^{4+} or Pb^{4+} often have large

band gaps, as demonstrated with $MgSnF_6$ above. Although Sundberg *et al.*[12] performed initial high-throughput initial calculations of F^- diffusion barriers via the IDPP method, the more rigorous nudged elastic band (NEB) method is considered one of the most accurate measures of the activation energy associated with a hopping event because it finds the saddle point of the minimum energy pathway between two sites. Because this method is computationally expensive, we chose a set of six materials, $ZnSnF_6$, $ZnPbF_6$, $CdSnF_6$, $CdPbF_6$, $HgSnF_6$, and $HgPbF_6$, to study periodic trends, as all A^{2+} metals belong to period 12 and B^{4+} belong to period 14. These materials also have low predicted diffusion barriers according to initial IDPP measurements.

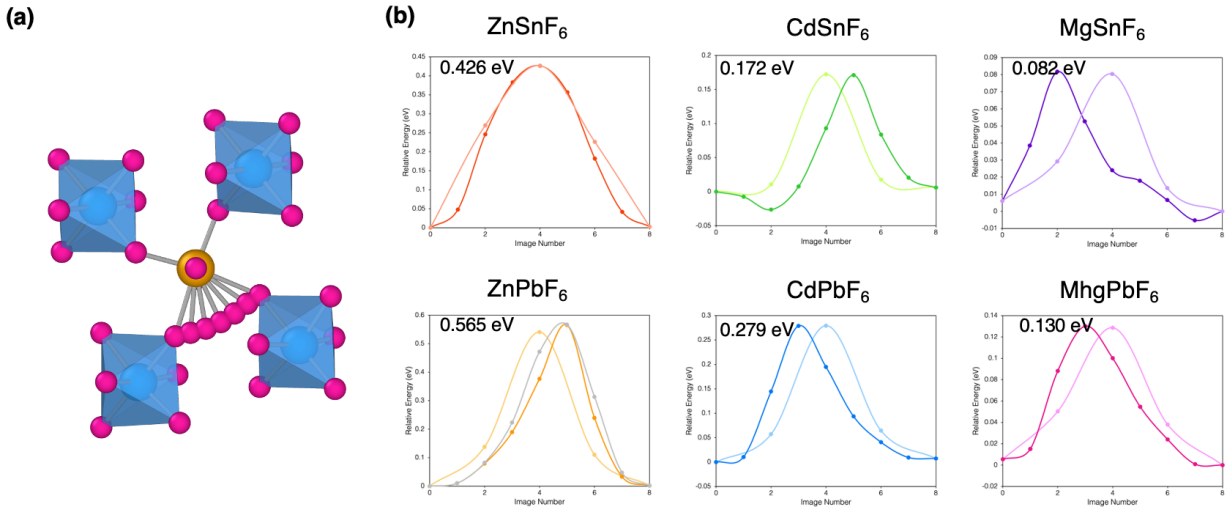


Figure 6-6. NEB pathways in ABF_6 materials. (a) A diagram showing the pathway taken by a single F atom in the NEB method. Each atom between points A and B represents an "image" where an energy calculation is performed. The number of images is set by the user. **(b)** The energies of NEB pathways for a subset of 6 materials, calculated with both 5 (light) and 7 (dark) images. Both calculations gave the same barrier within ±5%.

Because each F site in these materials is symmetry equivalent, only one path is needed to form a percolation pathway throughout the material, as shown in Figure 6-6a. Each diffusion pathway was calculated with climbing image NEB[20] so that the highest-energy point is driven up to the energy maximum, therefore ensuring that the true transition state is

captured. Figure 6-6b shows the NEB diagrams for each pathway, which were calculated via two separate NEB calculations, one with 5 images and one with 7 images. This was done to confirm that NEB calculations with fewer images still capture the transition state. Because each calculation was within error of each other, we deem both 5 images and 7 images to be accurate.

As we move down period 11 of the periodic table from Zn to Cd to Hg, diffusion barriers decrease. We hypothesize that this is due to the larger unit cell size due to the ionic radii of the metals, allowing the F^- pathway to be farther away from neighboring cations. Table 6-2 lists the band gaps and diffusion barriers for each of these materials.

Table 6-2. Diffusion barriers and band gaps for a set of ABF_6 materials. All values are given in eV. The diffusion barriers were calculated via NEB and band gaps with the HSE06 functional.

	Diffusion Barrier	Band Gap
$ZnSnF_6$	0.427	6.0326
$ZnPbF_6$	0.541	3.8455
$CdSnF_6$	0.172	6.0269
$CdPbF_6$	0.279	4.0591
$HgSnF_6$	0.082	4.3534
$HgPbF_6$	0.129	2.902

To be a viable solid-state electrolyte, a crystalline solid should have a band gap greater than 3.5 eV and a diffusion barrier less than 0.7 eV[12]. All of these materials, with the exception of $HgPbF_6$, which has a band gap of 2.902 eV, meet these criteria. We therefore selected our candidate material by a subsequent set of criteria that a commercial solid-state electrolyte must face: safety/toxicity and cost of raw materials. $ZnSnF_6$ was thus chosen as our target synthetic candidate.

6.5 Solid-State Synthesis of $ZnSnF_6$

A synthesis of $ZnSnF_6$ by direct fluorination in the presence of pure HF was published in 1950 by Hoppe *et al.*[21] This method formed a $ZnSnF_6$ hydrate that was subsequently dehydrated. We sought to synthesize the material in a safer, more scalable way that did not require additional dehydration. We therefore used mechanochemical ball-milling, which has not been used to synthesize an ABF_6 compound but has been used for various other ternary oxides and fluorides.[22–28] By performing this in an Ar atmosphere, we also negated the need for further dehydration.

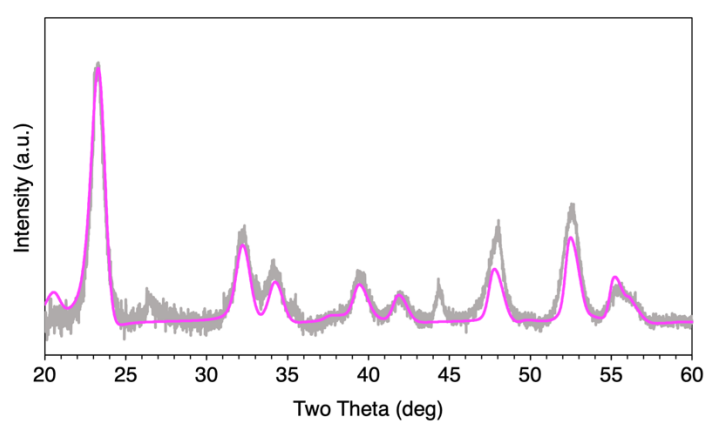


Figure 6-7. X-ray diffraction of $ZnSnF_6$ from mechanochemical ball-milling. Grey represents the experimental data, and pink represents the fit to the calculated structure via Rietveld refinement. All the peaks not fit with the refinement are attributed to ZnF_2.

The broad XRD peaks in Figure 6-7 are representative of small crystallite sizes in a polycrystalline material, which is to be expected from a mechanochemically ball milled sample. The crystallite size can be increased by sintering after ball milling. Rietveld refinement[29] indicates that a small amount of the starting material ZnF_2 is still present. Because the two starting materials, ZnF_2 and SnF_4, were combined in stoichiometric amounts, we hypothesize that the excess SnF_4 either reacted with the stainless steel ball mill jar or is still present in the material as an amorphous compound. However, this is the first successful synthesis of $ZnSNF_6$ via mechanochemical ball milling.

6.6 Conclusions

We have studied viable solid-state electrolytes for FIBs by investigating all ABF_6 crystals. We then performed high-quality calculations of band structure of the ABF_6 materials with space group 148, as these are the most promising structures according to preliminary calculations of band gap and fluoride diffusion barrier in the literature[12]. The band gaps obtained from these calculations allowed us to (1) perform linear regression between low-quality PBE calculations and high-quality HSE calculations to predict correct band gaps in the future and (2) understand periodic trends with a case study of ABF_6 materials where A is Mg^{2+} and (3) filter materials for the best solid-state electrolyte candidates. We then performed NEB calculations on a subset of materials where $A^{2+} = Zn^{2+}$, Cd^{2+}, or Hg^{2+} and $B^{4+} = Sn^{4+}$ or Pb^{4+}. From this, we chose the $ZnSnF_6$ material as our most promising candidate for synthesis and successfully synthesized a polycrystalline sample via mechanochemical ball milling.

REFERENCES

(1) Li, M.; Wang, C.; Chen, Z.; Xu, K.; Lu, J. New Concepts in Electrolytes. *Chem. Rev.* **2020**, *120*, 6783–6819.

(2) Chen, R.; Li, Q.; Yu, X.; Chen, L.; Li, H. Approaching Practically Accessible Solid-State Batteries: Stability Issues Related to Solid Electrolytes and Interfaces. *Chem. Rev.* **2020**, *120*, 6820–6877.

(3) Mohammad, I.; Witter, R.; Fichtner, M.; Anji Reddy, M. Room-Temperature, Rechargeable Solid-State Fluoride-Ion Batteries. *ACS Appl. Energy Mater.* **2018**, *1*, 4766–4775.

(4) Hammad Fawey, M.; Chakravadhanula, V. S. K.; Reddy, M. A.; Rongeat, C.; Scherer, T.; Hahn, H.; Fichtner, M.; Kübel, C. In Situ TEM Studies of Micron-Sized All-Solid-State Fluoride Ion Batteries: Preparation, Prospects, and Challenges. *Microsc. Res. Tech.* **2016**, *79*, 615–624.

(5) Famprikis, T.; Canepa, P.; Dawson, J. A.; Islam, M. S.; Masquelier, C. Fundamentals of Inorganic Solid-State Electrolytes for Batteries. *Nat. Mater.* **2019**, *18*, 1278–1291.

(6) Slater, M. D.; Kim, D.; Lee, E.; Johnson, C. S. Sodium-Ion Batteries. *Adv. Funct. Mater* **2013**, *23*, 947–958.

(7) Wang, F.; Fan, X.; Gao, T.; Sun, W.; Ma, Z.; Yang, C.; Han, F.; Xu, K.; Wang, C. High-Voltage Aqueous Magnesium Ion Batteries. *ACS Cent. Sci.* **2017**, *3*, 1121–1128.

(8) Ming, J.; Guo, J.; Xia, C.; Wang, W.; Alshareef, H. N. Zinc-Ion Batteries: Materials, Mechanisms, and Applications. *Materials Science and Engineering: R: Reports* **2019**, *135*, 58–84.

(9) Anji Reddy, M.; Fichtner, M. Batteries Based on Fluoride Shuttle. *J. Mater. Chem* **2011**, *21*, 17059.

(10) Xiao, A. W.; Galatolo, G.; Pasta, M. The Case for Fluoride-Ion Batteries. *Joule* **2021**.

(11) Nowroozi, M. A.; Mohammad, I.; Molaiyan, P.; Wissel, K.; Munnangi, A. R.; Clemens, O. Fluoride Ion Batteries – Past, Present, and Future. *J. Mater. Chem. A* **2021**.

(12) Sundberg, J. D.; Druffel, D. L.; McRae, L. M.; Lanetti, M. G.; Pawlik, J. T.; Warren, S. C. High-Throughput Discovery of Fluoride-Ion Conductors via a Decoupled, Dynamic, and Iterative (DDI) Framework. *npj Comput. Mater.* **2022**, *8*, 106.

(13) Jain, A.; Ong, S. P.; Hautier, G.; Chen, W.; Richards, W. D.; Dacek, S.; Cholia, S.; Gunter, D.; Skinner, D.; Ceder, G.; Persson, K. A. Commentary: The Materials Project: A Materials Genome Approach to Accelerating Materials Innovation. *APL Mater.* **2013**, *1*, 011002.

(14) Smidstrup, S.; Pedersen, A.; Stokbro, K.; Jónsson, H. Improved Initial Guess for Minimum Energy Path Calculations. *J. Chem. Phys.* **2014**, *140*, 214106.

(15) Jónsson, H.; Mills, G.; Jacobsen, K. W. Nudged Elastic Band Method for Finding Minimum Energy Paths of Transitions. In *Classical and Quantum Dynamics in Condensed Phase Simulations*; Berne, B. J.; Ciccotti, G.; Coker, D. F., Eds.; World Scientific, 1998; pp. 385–404.

(16) Ong, S. P.; Richards, W. D.; Jain, A.; Hautier, G.; Kocher, M.; Cholia, S.; Gunter, D.; Chevrier, V. L.; Persson, K. A.; Ceder, G. Python Materials Genomics (Pymatgen): A Robust, Open-Source Python Library for Materials Analysis. *Comp. Mater. Sci.* **2013**, *68*, 314–319.

(17) Perdew, J. P.; Burke, K.; Ernzerhof, M. Generalized Gradient Approximation Made Simple. *Phys. Rev. Lett.* **1996**, *77*, 3865–3868.

(18) Krukau, A. V.; Vydrov, O. A.; Izmaylov, A. F.; Scuseria, G. E. Influence of the Exchange Screening Parameter on the Performance of Screened Hybrid Functionals. *J. Chem. Phys.* **2006**, *125*, 224106.

(19) Sundberg, J. D.; Benjamin, S. S.; McRae, L. M.; Warren, S. C. Simmate: A Framework for Materials Science. *JOSS* **2022**, *7*, 4364.

(20) Henkelman, G.; Uberuaga, B. P.; Jónsson, H. A Climbing Image Nudged Elastic Band Method for Finding Saddle Points and Minimum Energy Paths. *J. Chem. Phys.* **2000**, *113*, 9901–9904.

(21) Hoppe, R.; Wilhelm, V.; Mueller, B. Zur Kenntnis Der Verbindungen m Sn F6 Mit m = Mn, Fe, Zn, Hg, Pb Bzw. Co, Ni, Cu, Cd. *Zeitschrift fuer Anorganische und Allgemeine Chemie* **1950**, *392:1–9*, 1972.

(22) Read, J. A.; Behl, W. K. Mechanochemical Synthesis of Carbon Fluorides. *Electrochem. Solid-State Lett.* **2009**, *12*, A16.

(23) Achary, K. R.; Rao, Y. B.; Kamadurai, R. K.; Patro, L. N. Mechanochemical Synthesis and Fluoride Ion Conductivity Studies in $Srsnf_4$ Polymorphs. *J. Phys. Chem. C* **2023**.

(24) Lee, J.; Zhang, Q.; Saito, F. Mechanochemical Synthesis of Ternary Fluorides with Perovskite Structures. *Chem. Lett.* **2001**, *30*, 700–701.

(25) Heise, M.; Scholz, G.; Düvel, A.; Heitjans, P.; Kemnitz, E. Mechanochemical Synthesis, Structure, and Properties of Solid Solutions of Alkaline Earth Metal Fluorides: Ma1−xMbxF2 (M: Ca, Sr, Ba). *Solid State Sciences* **2016**, *60*, 65–74.

(26) Preishuber-Pflügl, F.; Wilkening, M. Mechanochemically Synthesized Fluorides: Local Structures and Ion Transport. *Dalton Trans.* **2016**, *45*, 8675–8687.

(27) Ao, W.; Li, J.; Yang, H.; Zeng, X.; Ma, X. Mechanochemical Synthesis of Zinc Oxide Nanocrystalline. *Powder Technol.* **2006**, *168*, 148–151.

(28) Yang, H.; Hu, Y.; Zhang, X.; Qiu, G. Mechanochemical Synthesis of Cobalt Oxide Nanoparticles. *Mater. Lett.* **2004**, *58*, 387–389.

(29) Rietveld, H. M. The Rietveld Method. *Phys. Scr.* **2014**, *89*, 098002.

APPENDIX A: SUPPORTING INFORMATION FOR CHAPTER 3

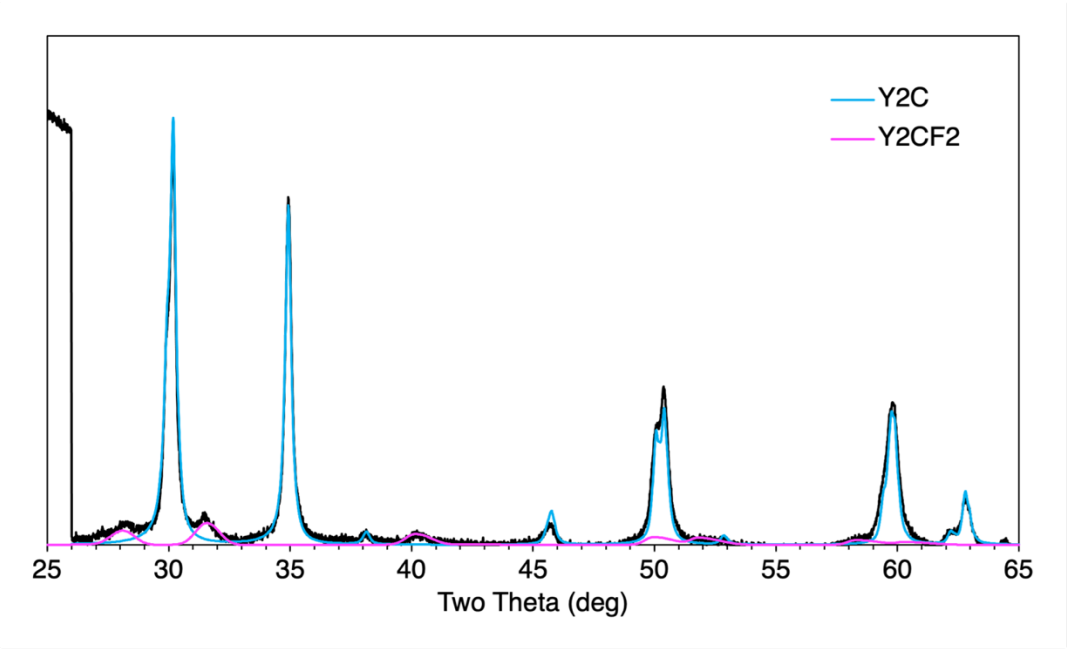


Figure A-1. XRD of partially fluorinated Y_2C . This sample was fluorinated with 15% stoichiometry of XeF_2 to confirm that F^- was not remaining in the ABC-stacked Y_2C structure. Rietveld refinement confirmed 13.4% conversion.

APPENDIX B: SUPPORTING INFORMATION FOR CHAPTER 5

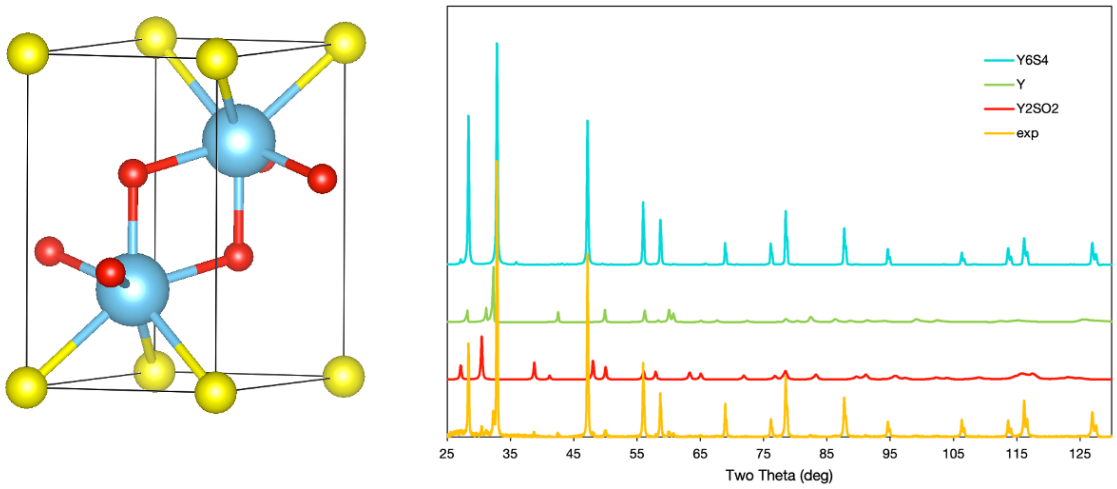


Figure B-1. Y_2SO_2 structure and XRD pattern of oxidized Y_6S_4. Unit cell structure of Y_2SO_2 shows layers of O^{2-} ions (red) between layers of Y (blue) and S (yellow). Y_2SO_2 peaks are most noticeable in the XRD pattern of as-synthesized Y_6S_x at low angles between 20-40º2θ

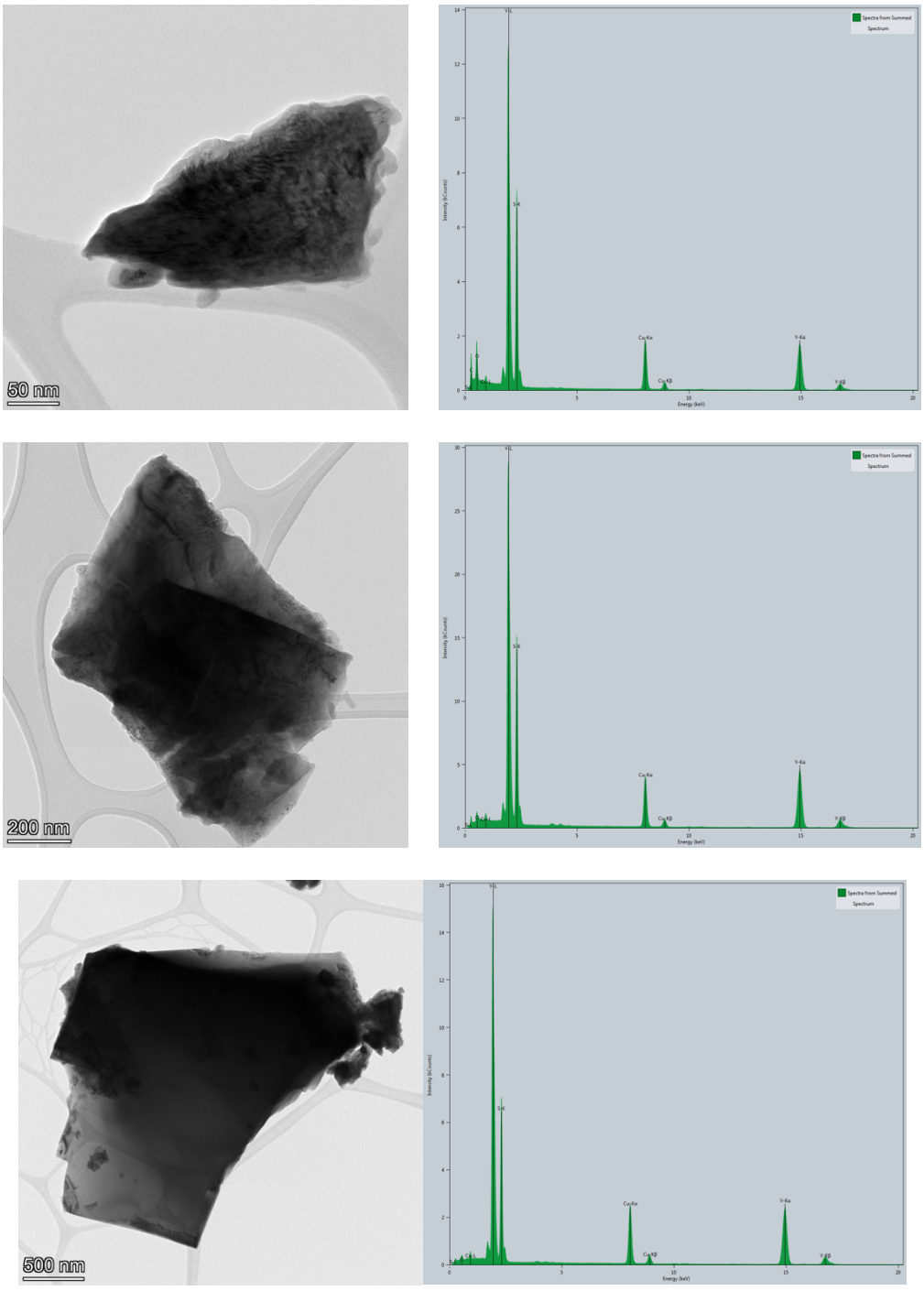


Figure B-2a. Bright-Field TEM images and EDS spectra of Y_6S_x particles.

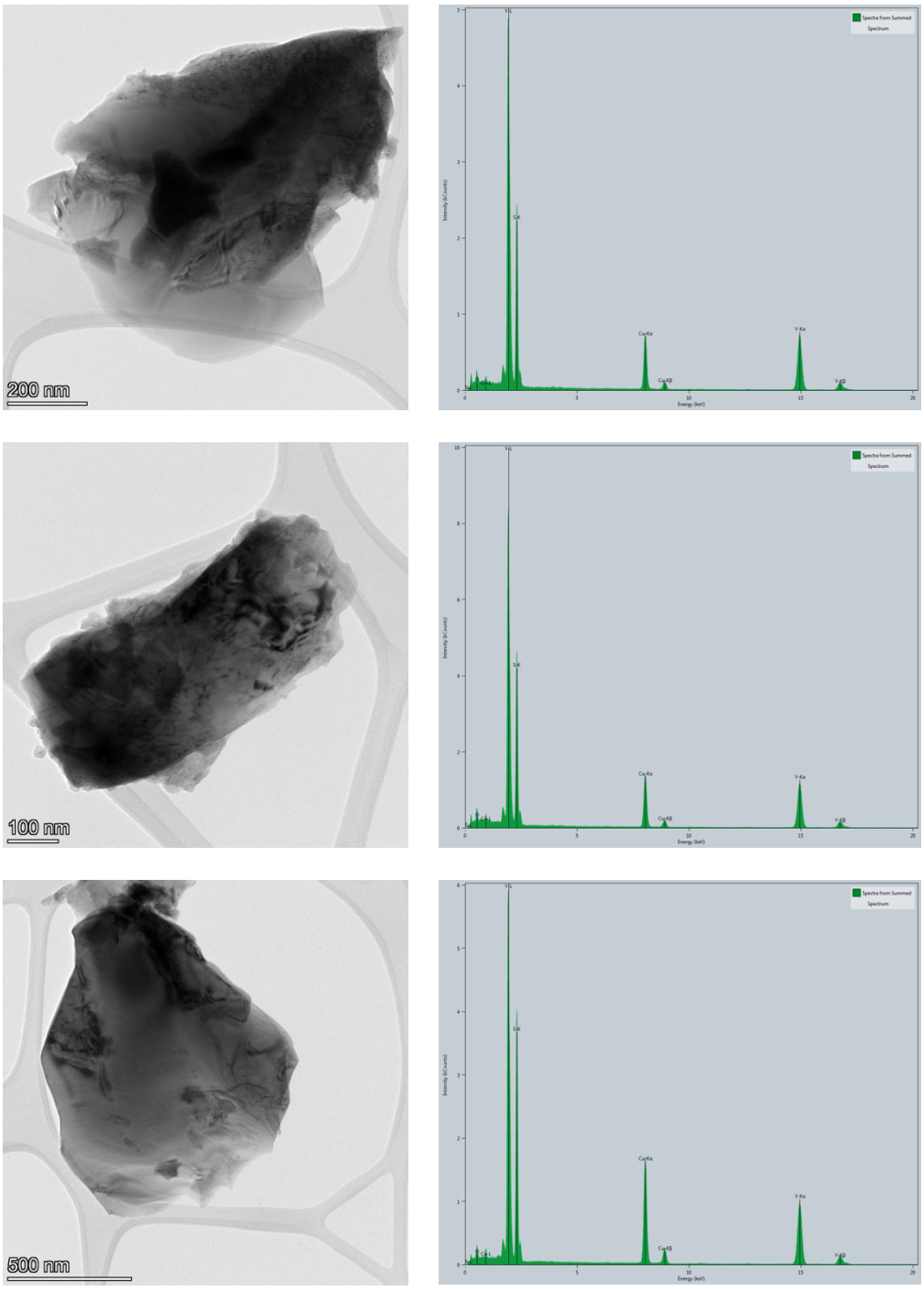


Figure B-2b. Bright-Field TEM images and EDS spectra of Y_6S_x particles.

APPENDIX C: SUPPORTING INFORMATION FOR CHAPTER 6

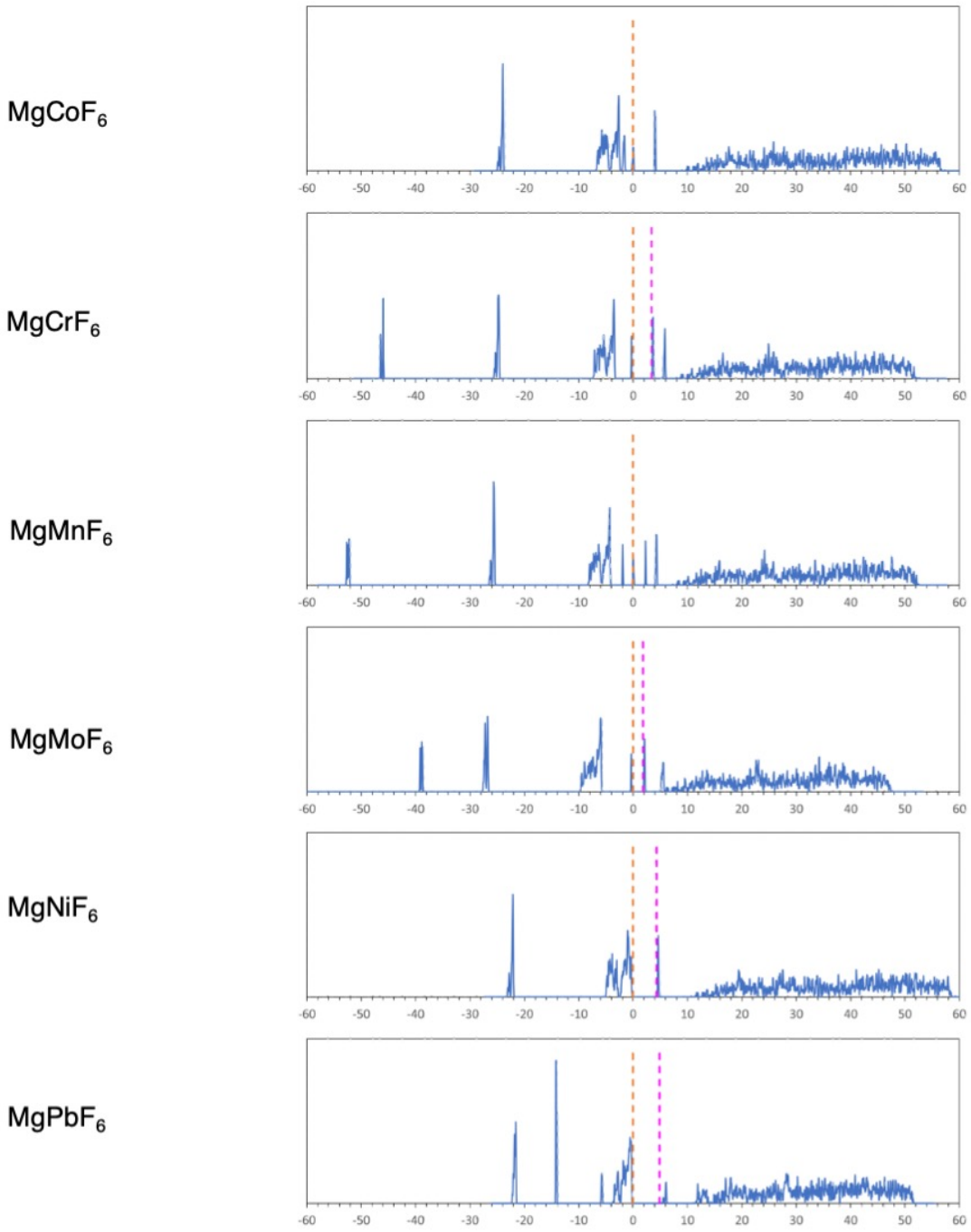
Table C-1. Band gaps and IDPP diffusion barriers of all ABF_6 structures. All structure identified from initial filtering of the Materials Project database.

Structure	IDPP Diffusion Barrier (eV)	Band Gaps (eV)			
		HSE		PBE	
		Band Structure Workflow	DOS Workflow	Band Structure Workflow	DOS Workflow
BaIrF6	0.69	2.18	1.63	0.00	0.00
BaSnF6	0.79	7.23	6.67	4.96	4.95
CaBiF6	--	1.23	0.46	0.05	0.05
CaCoF6	1.48	3.55	2.80	1.77	1.76
CaCrF6	0.91	3.01	2.30	1.82	1.80
CaFeF6	--	1.41	0.61	0.00	0.00
CaMnF6	0.82	5.03	4.46	3.22	3.20
CaMoF6	0.59	2.06	1.55	2.50	2.48
CaNiF6	0.84	4.19	3.35	2.20	2.17
CaPdF6	0.90	4.17	3.66	1.98	1.94
CaPtF6	--	4.64	3.95	2.48	2.44
CaRhF6	0.68	2.22	1.58	0.00	0.00
CaSbF6	--	1.13	0.45	0.00	0.00
CaSnF6	--	7.71	7.09	5.42	5.42
CaTiF6	--	6.88	6.03	4.76	4.74
CaVF6	--	3.43	2.79	0.00	0.00
CaWF6	0.75	1.86	1.11	3.74	3.69
CrCdF6	0.72	3.00	2.40	1.78	1.76
CdPbF6	0.54	4.06	3.67	2.34	2.35
CdPdF6	0.89	3.75	3.17	1.66	1.65
CdPtF6	--	4.14	3.48	2.04	2.02
CdRhF6	0.81	2.20	1.64	0.00	0.00
CdSnF6	0.85	6.03	5.61	3.85	3.88
TiCdF6	0.69	6.47	5.72	4.39	4.36
CoPtF6	--	3.07	2.45	1.96	1.94
CoSnF6	0.72	3.83	3.37	2.65	2.70
ZrCoF6	--	--	--	0.00	0.00
CrMoF6	0.71	2.98	2.07	2.76	2.75
CrNiF6	0.43	--	--	0.00	0.00
CsAsF6	1.47	7.57	6.98	5.17	5.18
CsBiF6	0.97	4.70	4.18	2.75	2.73
CsNbF6	1.02	7.11	6.56	5.20	5.20
CsReF6	--	1.88	1.23	0.00	0.00
CsSbF6	1.36	7.31	6.82	5.00	4.98

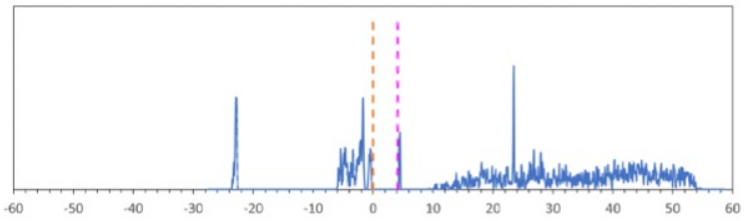
CsUF6	--	4.26	3.39	1.02	4.27
CuMoF6	--	0.00	0.00	0.00	0.00
CuSnF6	--	4.24	3.53	0.00	0.00
FeSnF6	--	1.43	0.58	0.00	0.00
ZrCuF6	--	--	--	0.00	0.00
NbFeF6	--	1.66	0.88	0.00	0.00
ZrFeF6	--	--	--	0.00	0.00
CrHgF6	2.11	2.78	2.13	1.60	1.55
HgPbF6	0.49	2.90	2.35	1.33	1.37
HgRhF6	0.84	2.05	1.37	0.00	0.00
SnHgF6	0.77	4.35	3.86	2.44	2.47
InAsF6	--	4.42	3.96	3.36	3.36
KAsF6	1.59	7.24	6.71	4.85	4.85
KCrF6	1.02	2.68	2.11	1.49	1.48
KOsF6	1.43	3.62	2.90	1.33	1.29
KPF6	1.65	9.47	8.77	7.03	7.06
KRhF6	1.03	1.87	1.09	0.00	0.00
LiAsF6	1.28	7.54	6.94	5.10	5.09
LiAuF6	--	3.83	3.26	1.83	1.83
LiBiF6	0.59	4.37	3.69	2.47	2.47
LiIrF6	0.96	1.68	0.81	0.00	0.00
LiMnF6	--	1.55	0.64	0.00	0.00
LiNbF6	0.82	7.04	6.27	5.13	5.09
LiOsF6	--	3.51	2.87	1.21	1.18
LiPF6	1.68	10.11	9.32	7.58	7.57
LiPtF6	--	1.44	0.82	0.00	0.00
LiRhF6	--	1.69	1.18	0.00	0.00
LiRuF6	1.06	3.45	2.54	1.10	1.04
LiSbF6	1.21	7.25	6.34	4.91	4.90
LiTaF6	--	8.30	7.51	6.26	6.25
MgBiF6	--	0.81	0.00	0.00	0.00
MgCoF6	0.87	3.32	2.59	1.57	1.53
MgCrF6	0.68	2.86	2.20	1.66	1.64
MgFeF6	--	1.40	0.32	0.00	0.00
MgMnF6	0.57	4.58	3.85	2.78	2.72
MgMoF6	0.34	2.04	1.44	2.45	2.42
MgNiF6	0.68	3.24	2.48	0.00	0.00
MgPbF6	0.71	5.09	4.39	3.07	3.09
MgPdF6	0.60	3.83	3.21	1.70	1.68
MgRhF6	0.55	2.14	1.40	0.00	0.00
MgSbF6	--	0.70	0.00	0.00	0.00
MgSnF6	0.73	7.31	6.64	4.98	5.00
MgTiF6	0.32	6.66	6.09	4.56	4.53

MgVF6	--	3.07	2.23	0.00	0.00
MgWF6	0.45	1.87	1.21	3.74	3.72
MnPtF6	--	2.92	2.21	1.86	1.83
MnSnF6	0.77	3.79	2.93	2.63	2.62
NaAsF6	--	7.60	7.15	5.18	5.18
NaBiF6	0.89	4.68	4.13	2.73	2.72
NaCrF6	--	2.64	1.90	0.00	0.00
NiPbF6	0.77	2.83	1.98	2.26	2.25
NiRhF6	0.57	--	--	0.03	0.00
NiSnF6	0.74	4.98	4.31	4.19	4.17
ZrPdF6	--	--	--	1.07	1.04
NiPtF6	--	--	--	2.08	2.04
PdPtF6	--	3.07	2.57	0.77	0.76
RbAsF6	1.39	7.37	6.85	4.97	4.97
RbBiF6	0.88	4.61	4.15	2.66	2.66
RbCrF6	1.01	2.72	2.09	1.50	1.47
RbSbF6	1.27	7.18	6.62	4.87	4.87
TlAsF6	1.32	5.92	5.36	4.62	4.60
TlGaF6	--	4.72	4.31	2.71	2.76
TlInF6	0.72	4.45	4.00	2.65	2.67
ScTlF6	--	5.99	5.34	3.99	3.96
NbVF6	--	1.49	0.89	0.00	0.00
ZnBiF6	--	0.00	0.00	0.00	0.00
ZnCoF6	0.75	3.04	2.45	1.36	1.35
ZnCrF6	0.48	2.91	--	1.66	1.64
ZnFeF6	0.41	0.00	0.00	0.00	0.00
MnZnF6	0.55	4.11	3.21	2.39	2.37
ZnMoF6	0.43	2.07	--	2.47	2.44
ZnNiF6	0.56	2.52	1.74	0.00	0.00
ZnPbF6	0.53	3.85	3.30	1.96	1.99
ZnPdF6	0.60	3.51	2.87	1.47	1.45
ZnPtF6	--	4.02	3.39	1.93	1.91
ZnRhF6	0.56	--	--	0.00	0.00
ZnSbF6	--	--	--	0.00	0.00
ZnSnF6	0.65	6.03	5.41	3.70	3.73
TiZnF6	0.05	6.41	5.76	4.23	4.21
VZnF6	--	3.04	2.44	0.00	0.00
ZnWF6	0.59	1.90	--	3.69	3.67

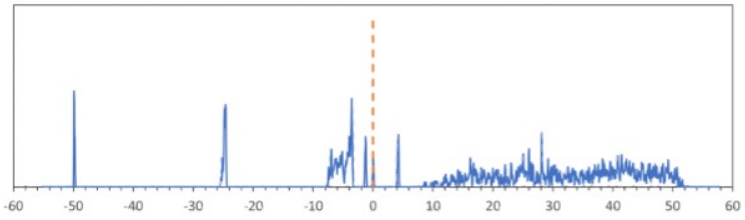
Figure C-1. Densities of states for Mg-containing structures. Calculations were performed on the full band structure but plotted as a DOS. Orange Dotted line represents the valence band and/or Fermi level; pink dotted line represents the conduction band.



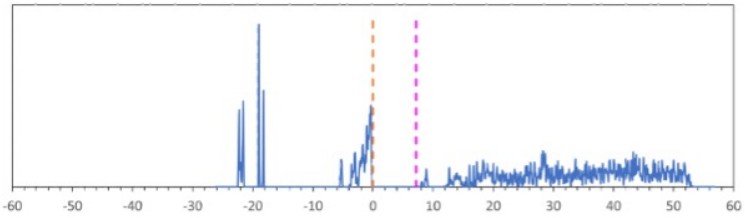
$MgPdF_6$



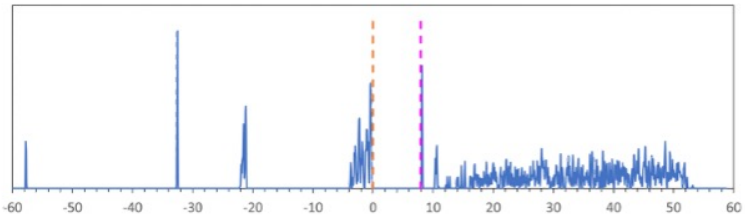
$MgRhF_6$



$MgSnF_6$



$MgTiF_6$



$MgWF_6$

